



SOFIA observations of far-IR fine-structure lines in galaxies to measure metallicity

LUIGI SPINOGLIO ¹, JUAN ANTONIO FERNÁNDEZ-ONTIVEROS ^{1,2}, MATTHEW A. MALKAN,³ SUYASH KUMAR,³ MIGUEL PEREIRA-SANTAELLA,⁴ BORJA PÉREZ-DÍAZ,⁵ ENRIQUE PÉREZ-MONTERO,⁵ ALFRED KRABBE,⁶ WILLIAM VACCA,⁷ SEBASTIAN COLDITZ,⁶ AND CHRISTIAN FISCHER⁶

¹*Istituto di Astrofisica e Planetologia Spaziale - INAF, Via Fosso del cavaliere 100, I-00133, Roma, Italy*

²*Centro de Estudios de Física del Cosmos de Aragón, Unidad Asociada al CSIC, Plaza San Juan 1, E-44001 Teruel, Spain*

³*Department of Physics and Astronomy, UCLA, Los Angeles, CA 90095-1547, USA*

⁴*Centro de Astrobiología (CSIC-INTA), Ctra. de Ajalvir, Km 4, 28850, Torrejón de Ardoz, Madrid, Spain*

⁵*Instituto de Astrofísica de Andalucía (IAA-CSIC), Glorieta de la Astronomía s/n, E-18008 Granada, Spain*

⁶*Deutsches SOFIA Institut, University of Stuttgart, Pfaffenwaldring 29, D-70569 Stuttgart, Germany*

⁷*SOFIA/USRA, NASA Ames Research Center, MS N232-12, Moffett Field, CA 94035-1000*

ABSTRACT

We present new and archival SOFIA FIFI-LS far-IR spectroscopic observations of 25 local galaxies of either the [OIII]52 μ m and/or the [NIII]57 μ m lines. Including other 31 galaxies from *Herschel*-PACS, we discuss a local sample of 47 galaxies, including HII region, luminous IR, low-metallicity dwarf and Seyfert galaxies. Analyzing the mid- to far-IR fine-structure lines of this sample, we assess the metallicity and compare with the optical spectroscopy estimates. Using the IR, we find a similar O/H–N/O relation to that known in the optical. As opposite, we find systematically lower N/O IR abundances when compared to the optical determinations, especially at high values of N/O ($\log(\text{N/O}) > -0.8$). We explore various hypotheses to account for this difference: (i) difference in ionization structure traced by optical (O⁺, N⁺ regions) versus IR lines (O²⁺, N²⁺ regions); (ii) contamination of diffuse ionized gas affecting the optical lines used to compute the N/O abundance; (iii) dust obscuration affecting the optical-based determinations. However, we have not found any correlation of the $\Delta(\text{N/O}) = (\text{N/O})_{\text{OPT}} - (\text{N/O})_{\text{IR}}$ with either ionization, or electron density, or optical extinction. We speculatively suggest that accretion of metal-poor gas from the circumgalactic medium could provide an explanation for this difference, because the rapid decrease of total abundances during infall is followed by a N/O ratio decrease due to primary production of young - possibly embedded - massive stars, are preferentially traced by the IR diagnostics, while optical diagnostics would better trace the secondary production, when both N/O and O/H abundance ratios will increase.

Keywords: Galaxy abundances, Active galaxies, Starburst galaxies, Dwarf galaxies, Far infrared astronomy, Spectroscopy

1. INTRODUCTION

The content of heavy elements in galaxies is a key physical diagnostic of galaxy evolution, because metals are a by-product of the star formation activity. Additionally, the metal abundances are modulated by inflow and outflow events, which involves both starburst and active galactic nuclei feeding and feedback processes. It has long been known that massive galaxies have higher metallicities, compared to galaxies with lower stellar mass (Lequeux et al. 1979; Tremonti et al.

2004). More recently the cosmic evolution of this correlation has been measured out to high redshifts (Henry et al. 2013; Ly et al. 2016; see Maiolino & Mannucci 2019 and references therein for a review). Besides the global metallicity, as measured by the O/H ratio, the relative abundances between heavy elements are also a key tool to understand the chemical evolution of galaxies (e.g. Pérez-Montero et al. 2013). One of the main problems that still need to be explored is for instance the behavior of the N/O ratio, which is dominated by primary oxygen and nitrogen production in young stellar populations. When these evolve during the lifetime of the galaxy, the nitrogen abundance is increased by the secondary production due to the yield of intermediate mass stars (Dopita & Evans 1986; Pilyugin et al. 2003; Vila-Costas & Ed-

munds 1993; Vincenzo et al. 2016). Furthermore, the N/O ratio depends on the star formation efficiency (e.g. Mollá et al. 2009), the accretion of pristine external gas (Amorín et al. 2010; Perez et al. 2011; Torrey et al. 2012), the efficiency of galactic winds in removing metals from the ISM (e.g. Hogarth et al. 2020), and on the shape of the IMF function (e.g. Tsujimoto & Bekki 2011). Therefore, while O/H provides information on the total amount of heavy elements produced, the N/O ratio tells us how these elements have been formed.

The earliest galaxies are likely to have very strong high-ionization emission lines. At their high redshifts ($z > 4$), their key diagnostic fine structure forbidden lines can be detected at sub-millimeter wavelengths by ALMA (De Breuck et al. 2019). To understand the abundances in the ionized ISM in these high-redshift galaxies, we need more and better observations of the same far-IR fine-structure lines in local galaxies and especially in nearby dwarf galaxies, characterized by low metal abundances.

Nearly all studies of the gas metallicity in galaxies have used rest-frame optical and UV diagnostics (e.g., Nagao et al. 2006; Kewley & Ellison 2008, and references therein). However, optical/UV spectroscopic methods to derive the gas metallicity have several limitations: (i) optical/UV diagnostics cannot probe the metallicity of the regions affected by significant dust extinction, or of dust-obscured galaxies; (ii) the emissivity of optical and UV permitted or forbidden lines depends strongly on the gas temperature, since the atomic levels involved in the transitions are highly excited above the ground level; (iii) nebular diagnostics using the optical [NII] lines can introduce biases, e.g. in the O/H abundances and the ionization parameter, for sources with high or low N/O abundances (Pérez-Montero & Contini 2009); (iv) when applied to nebular lines in active galactic nuclei (AGN), the temperature method – widely used in star-forming regions – underestimates the metallicities by typically ~ 0.8 dex when compared to estimates from strong-line methods (Dors et al. 2015). Additionally, a large fraction of oxygen in AGN is expected to be highly ionized ($O^{>2+}$) and therefore not traced by the optical transitions (Pérez-Montero et al. 2019). All these limitations are overcome by using the IR fine structure lines, as was shown using observations of planetary nebulae (Pottasch & Beintema 1999; Bernard-Salas et al. 2001; Liu et al. 2001) by the Short Wavelength Spectrometer (SWS; de Graauw et al. 1996) and the Long Wavelength Spectrometer (LWS; Clegg et al. 1996) onboard the Infrared Space Observatory (ISO; Kessler et al. 1996).

The use of IR fine structure line ratios for gas metallicity diagnostics and in particular for measuring abundance ratios different from the solar values has been pioneered by Spinoglio & Malkan (1992), who considered in their study HII region abundances and highly dust depleted abundances using a standard photoionization code. More recently, metal-

licity diagnostics based on the far-IR fine structure lines of [OIII]51.8 μ m, [OIII]88.3 μ m, and [NIII]57.2 μ m have been proposed as metallicity tracers by Nagao et al. (2011) and applied to *Herschel*-PACS observations of Ultra-Luminous IR Galaxies (ULIRG) by Pereira-Santaella et al. (2017) and (Herrera-Camus et al. 2018). The nebular ionization structure of oxygen and nitrogen species is expected to be nearly identical, due to the very similar ionization potential values of these elements (13.6 and 14.5 eV for O^+ and N^+ , respectively, 35.1 and 29.6 eV for O^{2+} and N^{2+}). This implies that the intensity ratios of O^{2+} and N^{2+} transitions can be used as a proxy for the global N/O abundance ratio. Nevertheless, this approach requires a previous knowledge of the O/H–N/O relation to derive metallicities, which may present large deviations from the relation observed in the local Universe, especially under extreme star formation conditions (e.g. Amorín et al. 2010).

Alternative IR-based tracers on the mid-IR lines of neon and sulfur were introduced by Fernández-Ontiveros et al. (2016, 2017) as potential tools to study the chemical evolution of galaxies at the *Cosmic Noon* through space-born IR spectroscopy. However, a large improvement in the determination of IR abundances was achieved by exploiting the full suite of mid- to far-IR lines. This was recently implemented by Fernández-Ontiveros et al. (2021) to determine chemical abundances for star-forming galaxies by applying Bayesian techniques to a grid of photoionization models covering a wide range in O/H, N/O, and U. Specifically, the N/O abundance can be fixed from the far-IR transitions of O^{2+} and N^{2+} , while the ionization-sensitive ratios of neon and sulfur lines can be used to determine the metallicity using known empirical correlations between the ionization parameter (U) and O/H (Pérez-Montero 2014) as priors.

In this work we present the largest available sample of galaxies for which new far-IR spectroscopic observations of [OIII]52 μ m and [NIII]57 μ m lines have been collected with SOFIA, complemented by the work of *Herschel*-PACS. This unique spectroscopic catalog allows us to develop and test new IR diagnostic for the global and relative abundances of heavy elements.

The paper is organized as follows. Section 2 presents the observations carried out with the Stratospheric Observatory for Infrared Astronomy (SOFIA; Temi et al. 2014), their data analysis procedure and the ancillary data that we have assembled to complement and analyze the results. Section 3 used IR line ratio diagrams to classify the galaxies of our sample according to the ionization and density of their line emission regions, using standard photoionization models. Section 4 outlines the two methods used to derive the abundances using optical lines and IR fine structure lines. Section 5 give the results of this work using various IR line ratio diagrams

to measure the metallicity and a discussion is presented in section 6. Finally, section 7 gives the summary of this work.

2. OBSERVATIONS

We present new observations with the SOFIA Far Infrared Field-Imaging Line Spectrometer (FIFI-LS [Fischer et al. 2018](#)) for 25 galaxies. FIFI-LS is a mid-IR medium resolution ($R \sim 500$ -2000) integral field spectrograph. It consists of two independently and simultaneously operated spectrographs and uses a dichroic to split incoming light into two channels: a blue side (50-125 μm) and a red side (100-205 μm). Each spectrograph contains an image slicer and a disperser that enables the simultaneous acquisition of spectra from 25 spatial positions. The detectors in both spectrographs consist of 400 (5 spatial x 5 spatial x 16 spectral) Gallium-doped Germanium pixels. The instantaneous spectral coverage of the 16 pixels ranges from 1000-3000 km s^{-1} . The blue side spectrograph has an instantaneous field of view of 30 x 30 arcsec with 6 arcsec spatial pixels (spaxels) while the red side has a field of view of 60 x 60 arcsec with 12 arcsec spaxels. The field of view of the blue side is completely contained within that of the red side. A description of the properties of FIFI-LS can be found in [Fischer et al. \(2018\)](#) and [Colditz et al. \(2020\)](#), and the SOFIA website¹.

Among the SOFIA FIFI-LS observations presented here, the only published data are those relative to Arp 299, Haro 3, IIZw40, M83, MCG+12-02-001, NGC 4194 and NGC 4214 and have been reported in [Peng et al. \(2021\)](#), however we performed a new analysis also of these data, in order to have an homogeneous data set. In most cases we have found results consistent (within the errors) with the values published by these authors, as can be seen in Tables 2 and 4. The only exceptions are for MCG+12-02-001, for which we adopted the [OIII]52 μm and [NIII]57 μm line fluxes published in [Peng et al. \(2021\)](#), because their results show a higher signal to noise ratio and for IIZw40 for which we find a significantly lower (by a factor ~ 2) [OIII]52 μm line flux, because of the more compact emission region that we have chosen ($\sim 15''$ in diameter) in this very compact galaxy compared to the more extended area sampled by [Peng et al. \(2021\)](#) ($\gtrsim 20''$ in diameter). In this latter case we report our flux measurement for the [OIII]52 μm line and we give an upper limit for the [NIII]57 μm line.

For NGC 2146 we adopted the line flux from [Brauer et al. \(2008\)](#), who used the ISO-LWS spectrometer.

The journal of the SOFIA FIFI-LS observations that we have reduced is presented in Table 1, where the detailed information on the SOFIA programs, including the AOR identification, the Mission-ID, the PI of the program, the ob-

served spectral line and the total integration time. In total we have analyzed the spectra of 25 galaxies. For 8 of these galaxies we have SOFIA detections of both the [OIII]52 μm and [NIII]57 μm lines, for another 8 galaxies we have combined the new [OIII]52 μm line detection from SOFIA with the [NIII]57 μm line observation from *Herschel*-PACS (see Table 2), while for the remaining 9 galaxies we present detections of the [OIII]52 μm line only, which are not complemented by any observation of the [NIII]57 μm line (Table 4). The data have been reduced with the FIFI-LS pipeline ([Vacca et al. 2020](#)) and the reduced datacubes have been retrieved from the SOFIA archive at IRSA².

2.1. Data Analysis

We present below our procedure for extracting emission line fluxes and their uncertainties for the SOFIA FIFI-LS data. We could not use the standard paxel by paxel fitting procedure, used normally for Integral Field Unit (IFU) data, because the high background contribution from the atmosphere drastically reduces the signal-to-noise ratio of our data sets.

We use here the example of NGC5253, a galaxy observed within our program (PI M.A. Malkan; AOR ID 07_0239_4). All other galaxies spectra have been reduced using the same method. The datacubes used for these reductions have all been obtained from the SOFIA data archive, unless otherwise indicated.

To illustrate the position of the FIFI-LS observations, we obtained a 2MASS H-band All-Sky Release Survey Atlas Image of each galaxy over approximately the same spatial scale as that covered by FIFI-LS on SOFIA. In the special cases of NGC2366 and UGC5189, we present WISE W1 band images of these galaxies instead of the 2MASS images due to the lack of significant emission in the latter; refer Figure 37(a) and 38(a). This is shown in Figure 1(a). The exact areas covered by FIFI are shown by the solid yellow and dotted salmon boxes (representing the regions covered for the [OIII]52 μm and [NIII]57 μm detections respectively).

The first step to determine the line fluxes of each source is to define a useful aperture. We do have a spatial resolution of about FWHM ~ 6 arcsec and compact but still not point like extension of the sources. We use the following procedure to find an ellipsoid shaped aperture for each data set to capture the whole flux while minimizing the noise contribution of pixels without flux from the source.

We locate the emitting region of the galaxy in the far-IR using SOFIA linemaps. The reduced datacube is a stack of 2-D flux channel maps at various wavelengths. We integrate these maps across ~ 10 wavelength channels surrounding the central redshifted wavelength of the emission line of interest. This gives us a preliminary linemap for the galaxy that helps

¹ <https://www.sofia.usra.edu/science/proposing-and-observing/observers-handbook-cycle-7/3-fifi-ls>

² <https://irsa.ipac.caltech.edu/Missions/sofia.html>

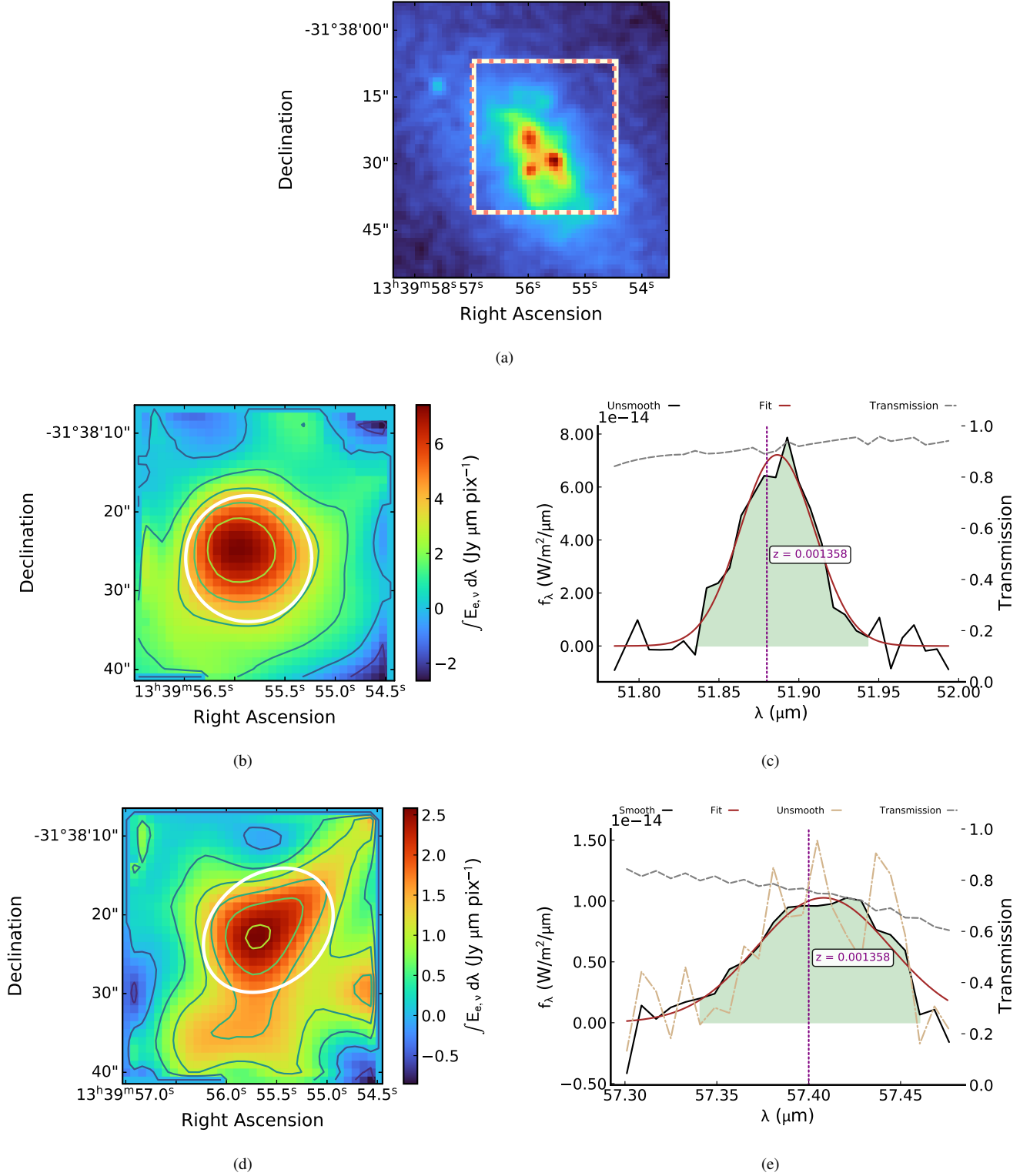


Figure 1. The 2MASS H-band image (Figure 1(a)), 2-D Linemaps and 1-D Spectra for [OIII]52 μm (Figures 1(b) and 1(c), respectively) and [NIII]57 μm (Figures 1(d) and 1(e), respectively) in NGC 5253. The [NIII]57 μm profiles here have not been corrected for atmospheric transmission.

us locate its emitting region. After choosing a center (which often aligns closely with the optical center of the galaxy),

we identify an elliptical aperture around the center that captures the majority of the emitting region. We add up the flux

densities from all spaxels within this elliptical aperture, and repeat this procedure separately for all wavelengths to obtain the wavelength profile of the spectral density of the emission line.

Before making the emission line flux calculation, we trim our spectrum by masking out noisy wavelength channels on the red/blue side of the central wavelength. If the spectrum is still noisy, we apply a Wiener filter to it (this is the case of the [NIII]57 μ m line, but not the [OIII]52 μ m line in NGC5253, see the solid black “Smooth” line in Figure 1).

Thereafter, we identify typically 5 to 10 continuum points on either side of the central peak in the trimmed spectrum. We use the median of these values as continuum signal and subtract it from all channels. We then add all the channels that were considered to be part of detection in the trimmed spectrum to create the continuum subtracted linemap (Figures 1(b) and 1(d)). After obtaining this linemap, we may find that it sometimes differs from the preliminary continuum map we made for the galaxy. In such cases, we choose a new center and elliptical aperture that better matches the continuum-subtracted linemap, and repeat the above procedure. It is possible that in doing so, the choice of continuum points changes. But the difference is usually minor, and after a few iterations, we converge to a choice of center, elliptical aperture, and continuum points that together give the best possible continuum-subtracted linemap, with the chosen elliptical aperture best identifying the emitting region of the galaxy. Figures 1(b) and 1(d) were obtained through this iterative procedure.

We point out two caveats at this stage. First, while we generally use the flux channel from a datacube that has been corrected for atmospheric transmission (this is the case of the [OIII]52 μ m line in NGC5253), occasionally the atmospheric transmission in the wavelength range of interest can be low (notice the grey-dashed line in Figure 1(e) with an atmospheric transmission as low as ~ 0.60). In these cases, we use the flux channel that has *not* been corrected for atmospheric transmission (this is the case of the [NIII]57 μ m line in NGC5253). We do so because the SOFIA archive’s automated correction procedure does not handle low transmissions. Second, while circular apertures may suit compact objects which are nearly point-like (e.g., the [OIII]52 μ m line in NGC5253), in other cases there is extended emission in certain directions, requiring an elliptical aperture to enclose most of the line emitting region and maximize the signal-to-noise ratio. Standard software, like QFitsView³, support only using circular apertures, so we wrote our own Python routine that can use elliptical apertures. The robustness of our routine has been verified by calculating fluxes indepen-

dently for identical circular apertures created by QFitsView and our routine (using the procedure that will be described hereafter), and checking that they are equal.

We now return to the trimmed spectrum that was obtained with an optimal choice of emission center, elliptical aperture, and continuum points to create the best continuum-subtracted linemap for the galaxy. We then subtract off the continuum from the trimmed spectrum and fit a Gaussian to the resulting emission line spectrum (solid brown lines in Figures 1(c) and 1(e)). This fitted Gaussian is overplotted with the solid black line in Figures 1(c) and 1(e). For Figure 1(e), where we applied the Wiener filter, we also include the unfiltered trimmed spectrum in the tan dot-dashed line). Finally, we overplot the transmission line (grey, dashed).

We then measure the line flux, F , by integrating the area under the continuum-subtracted trimmed spectrum (green shaded area in Figures 1(c) and 1(e)). We exclude from this integration the spectral range used to estimate the continuum level. We then compute the formal statistical error δF in the flux as:

$$\delta F = \Delta\lambda \sqrt{\sum_P (f(P) - y_P)^2} \quad (1)$$

Here, P is a continuum point, y_P is its spectral density, and $f(P)$ is its spectral density as predicted by the fitted continuum line. $\Delta\lambda$ is the wavelength pixel width (which is 0.007 μ m for SOFIA). Calculating δF amounts to adding the errors between the actual spectrum and the continuum line in quadrature. Note at this stage that if the flux channel used for the galaxy was *not* corrected for atmospheric transmission, we replace our calculated flux F with $F / \langle T \rangle$, where $\langle T \rangle$ is the average transmission in the wavelength range we integrate across to calculate F .

The formal statistical error does not take into account the uncertainty in setting the continuum level. To compute a more realistic error bar for our flux measurement, we make a slightly different choice of the continuum points in our trimmed spectrum (or alternatively make a somewhat different selection for the noise to discard from the untrimmed spectrum). This subjective estimate gives us a different, but still “nearly correct” continuum level. We repeat the aforementioned process to compute the flux with the formal statistical error again.

This leaves us with two flux readings, $F_1 \pm \delta F_1$ and $F_2 \pm \delta F_2$, from the two iterations. We are now ready to estimate the actual flux measurement as $F \pm \Delta F$, where:

$$F = \frac{F_1 + F_2}{2} \quad (2)$$

and:

$$\Delta F = \max(F_1, F_2) - \min(F_1, F_2) + \delta F_1 + \delta F_2 \quad (3)$$

³ <https://www.mpe.mpg.de/~ott/QFitsView>

Essentially, we are deriving our flux as the average of both estimates, and the error as the difference of the upper bound and lower bound as dictated by the formal statistical error. This completes our data reduction process.

2.2. Ancillary data

We have used the literature data to complement the observations obtained with SOFIA FIFI-LS. In particular we have taken the catalog of *Herschel* (Pilbratt et al. 2010) PACS (Poglitsch et al. 2010) and SPIRE (Griffin et al. 2010) observations of AGN and Starburst galaxies of Fernández-Ontiveros et al. (2016) and the observations of the dwarf galaxies of Cormier et al. (2015). We also included the ISO-LWS observations reported from Brauer et al. (2008) of NGC 2146 and NGC 4194. Our sample of local galaxies contains 47 galaxies divided in 21 HII region/(U)LIRG galaxies, 19 Seyfert galaxies, including one LINER and 7 dwarf galaxies. The sample is presented in Table 5, with all the relevant information, including coordinates, redshift, optical metallicities and N/O ratio, as computed from optical emission line observations (Pérez-Montero 2014), as well as the abundances and the N/O ratio computed from the IR lines (Fernández-Ontiveros et al. 2021). The full dataset of far-IR spectroscopy of the sample of 48 galaxies is given in Table 2.

We have also compiled the observations of the mid-IR fine-structure lines, mainly collected from the *Spitzer* (Werner et al. 2004) Infrared Spectrograph (IRS; Houck et al. 2004), as shown in Table 3. We note that this table contains 51 galaxies, because we have also included 3 objects for which we do not have full far-IR lines coverage: IC342, NGC2976 and NGC4536.

Table 4 presents the SOFIA FIFI-LS observations of the [OIII]52 μ m line of an additional list of 11 galaxies, for which we do not have detections of the [NIII]57 μ m line, and therefore we are not able to discuss them further.

3. SAMPLE CHARACTERIZATION

We present in Fig. 2 the so-called “IR BPT” diagram proposed for the first time by Fernández-Ontiveros et al. (2016). In contrast with the optical BPT, the diagram in Fig. 2 can be regarded as a “softness diagram”, because the axes ([OIV]25.9 μ m/[OIII]88 μ m and [NeIII]15.6 μ m/[NeII]12.8 μ m) are independent of the chemical abundances, and thus represent a more selective measure of the strength and shape of the radiation field in the ~ 20 –80 eV range (see also Vilchez & Pagel 1988; Pérez-Montero & Vilchez 2009; Meléndez et al. 2011). Here the separation of the different types of galaxies is largely independent of photoionization models to define the boundaries, mostly due to the high ionization potential of O³⁺ (54.9 eV). This is beyond the double ionization edge of helium (54.4 eV), where the continuum emission of any stellar population drops

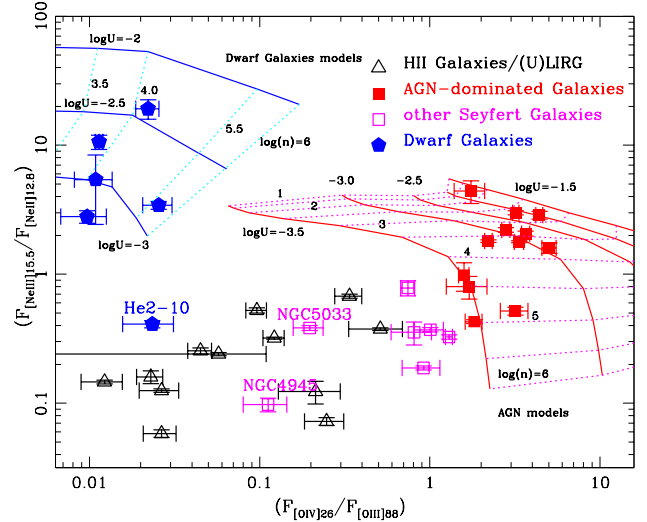


Figure 2. [NeIII]15.6 μ m/[NeII]12.8 μ m line ratio versus the [OIV]25.9 μ m/[OIII]88 μ m line ratio, the so-called *IR BPT* diagram (Fernández-Ontiveros et al. 2016), showing the separation between the galaxy types: on the right AGN, on the bottom left Starbursts/HII region galaxies and ULIRGs and on the upper left part the dwarf galaxies, characterized by low metallicity. The two Seyfert galaxies NGC4945 and NGC5033 have line ratios more typical of HII region galaxies, and also the dwarf galaxy He2-10 is similar to them. A grid of AGN photoionization models (models A in Section 4) spans the parameters value of: $1.0 < \log(n) < 6.0$ and $-3.5 < \log(U) < -1.5$. Similarly a grid of low-metallicity starburst galaxies models (models A in Section 4 with a metallicity of $Z = 0.004$ ($1/5 Z_{\odot}$)), the ranges of $3.5 < \log(n) < 6.0$ and $-3.0 < \log(U) < -2.0$.

sharply while the AGN power-law continuum remains unaffected. Consequently, AGN are in the right part of the diagram, characterized by a higher value of the ionization of the gas responsible for the emission, the HII region galaxies and (U)LIRG are on the lower left part of the diagram, while the dwarf galaxies at the upper left region, having a metallicity significantly lower than solar. An additional advantage of IR diagnostics is that they are insensitive to dust extinction and temperature effects, in contrast with optical tracers.

The IR BPT represents a very powerful tool to separate galaxies not only by the shape of their primary ionizing spectrum, i.e. star formation or AGN dominated, using the [OIV]25.9 μ m/[OIII]88 μ m line ratio, but also for the different metallicities, through the [NeIII]15.6 μ m/[NeII]12.8 μ m line ratio. We use this diagram to further classify the Seyfert galaxies into two separate classes: those within the grid of AGN photoionization models (models A in Section 4) are classified hereafter as “AGN-dominated” galaxies, while those outside these models are called “other Seyfert galaxies”. These latter galaxies include: NGC 4945, NGC 5033, CenA (NGC 5128), NGC 6240, NGC 7130 (IC 5135), NGC 7469 and NGC 7582. We note that for these

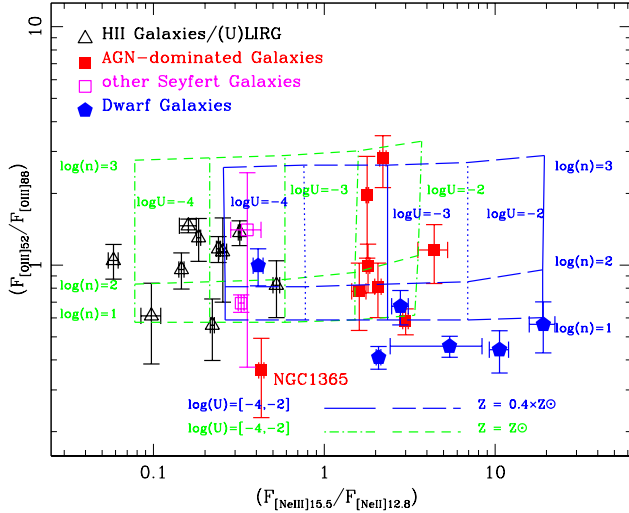


Figure 3. Ionization density diagram made with the $[\text{OIII}]52\mu\text{m}/88\mu\text{m}$ ratio versus the $[\text{NeIII}]15.5\mu\text{m}/[\text{NeII}]12.8\mu\text{m}$ ratio. The grid of models (models B in Section 4) represent Starburst models with density $\log(n)=[1,3]$ and ionization potential of $\log(U)=[-2,-4]$. Two types of abundances have been assumed: solar (grid with density as short-dashed line and ionization parameter as dot-dashed line) and subsolar with $Z=0.4\times Z_{\odot}$ (grid with density as long-dashed line and ionization parameter as solid line). The effect of sub-solar abundances shifts the models to the right, and intercepts a low metallicity dwarf galaxy.

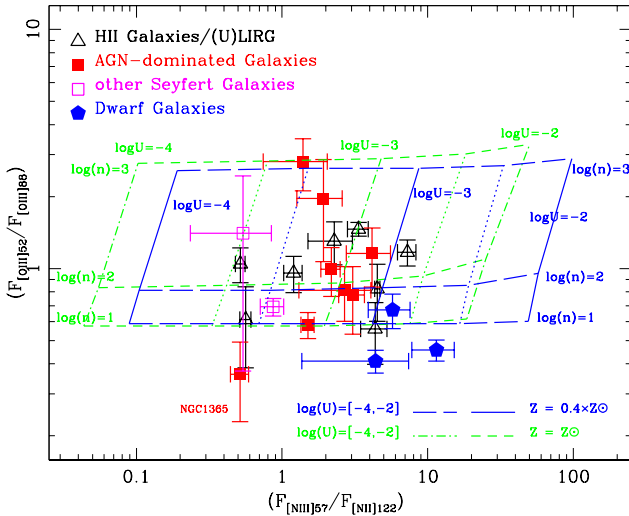


Figure 4. Ionization density diagram made with the $[\text{OIII}]52\mu\text{m}/88\mu\text{m}$ ratio versus the $[\text{NIII}]57\mu\text{m}/[\text{NII}]122\mu\text{m}$ ratio. The models are the same as in Fig. 3, again with the two types of abundances: solar and sub-solar ($Z=0.4\times Z_{\odot}$).

galaxies the IR lines excitation can originate from, or at least be contaminated by, HII regions in the host galaxy (Xia et al. 2018).

In Fig. 3 we show an ionization-density diagram made using the line ratios of $[\text{OIII}]52\mu\text{m}/88\mu\text{m}$ and $[\text{NeIII}]15.5\mu\text{m}/[\text{NeII}]12.8\mu\text{m}$. Two grids of starburst photoionization models (models B in Section 4) are shown, one with solar metal abundances and the other with sub-solar abundances. The diagram shows that the typical density is $\sim 1.0 < \log(n_e/\text{cm}^{-3}) < 3.0$, while the ionization parameter is $\sim -4 < \log(U) < -2$ for HII region galaxies/ULIRG. The effect of decreasing the metal abundances is to shift the model grid to the right side of the diagram, because the line ratio tracing the ionization parameter is sensitive to the metal abundances. The $[\text{NeIII}]15.5\mu\text{m}/[\text{NeII}]12.8\mu\text{m}$ ratio increases by an average factor of $\gtrsim 5$, from solar to $0.4 \times Z_{\odot}$ abundances. We notice in Fig. 3 that the three galaxies in this diagram classified as “other Seyfert” galaxies are well within the area populated by the HII region/ULIRG galaxies, confirming that most of their ionized emission does not originate in the AGN Narrow Line Region (NLR), as indicated by the low value of the ionization potential ($\log U \sim -3.5$).

Figure 4 shows another ionization-density diagram, made purely with far-IR lines, the $[\text{OIII}]52\mu\text{m}/88\mu\text{m}$ ratio versus the $[\text{NIII}]57\mu\text{m}/[\text{NII}]122\mu\text{m}$ ratio. Similarly to the previous diagram, this diagram also indicates that the gas density is $\sim 1.0 < \log(n_e/\text{cm}^{-3}) < 3.0$, and the ionization parameter is $\sim -4 < \log(U) < -2$. The effect of decreasing the metal abundances is to increase the ratio of $[\text{NIII}]57\mu\text{m}/[\text{NII}]122\mu\text{m}$ by an average factor of $\gtrsim 2.5$, from solar to $0.4 \times Z_{\odot}$ abundances.

4. PHOTOIONIZATION MODELS AND ABUNDANCE DETERMINATIONS

In this work we have used various photoionization models using the CLOUDY code (Ferland et al. 2017), also with the aim to demonstrate their overall consistency with each other, which does not depend on the particular choices of the parameters details. One set of models (hereafter models A) has been taken from Fernández-Ontiveros et al. (2016) which includes both AGN models and starburst galaxies models. For the AGN, a grid of constant density models (with $\log(n_H) (\text{cm}^{-3}) = 1$ to 6) in a plane-parallel geometry has been built using an AGN ionizing continuum of a power law from the optical to the X-rays with a slope of $\alpha = -1.4$ ($S_{\nu} \propto \nu^{\alpha}$), and ionization parameters (U) with values of $\log U = -1.5, -2.0, -2.5, -3.0, -3.5$. For these models, the maximum column density of $N_H = 10^{23} \text{ cm}^{-2}$ was used as the stopping criterion of the spatial integration, representative of the column density found in NLR clouds (Moore & Cohen 1994).

For the star forming galaxies models, the ionizing spectrum was simulated using the STARBURST99 code (Leitherer et al. 1999) for two cases: (1) a young burst of star formation with an age of 1 Myr and a metallicity of $Z = 0.004(1/5Z_{\odot})$, in order to produce the hard UV ion-

izing spectrum in a low-metallicity environment, such the one typical of dwarf galaxies, and (2) a continuous burst of star formation with an age of 20 Myr and solar metallicity, to model normal star forming galaxies. We use models with plane-parallel geometry, constant pressure, initial densities in the $\log(n_H)$ (cm^{-3}) = 1 to 6 range, and ionization parameters in the $\log U$ = -2.0 to -4.5 range. We assumed two intervals for the Kroupa initial mass function (IMF; with exponents 1.3, 2.3 and mass boundaries of 0.1, 0.5, and 100 M_\odot), the 1994 Geneva tracks with standard mass-loss rates, and the Pauldrach/Hillier atmospheres, which take into account the effects of non-LTE and radiation driven winds.

Another set of models (hereafter models B) has been taken from [Pereira-Santaella et al. \(2017\)](#) and includes both starburst galaxies and AGN models. In starburst models, they assumed a constant pressure slab model illuminated by the spectrum of a continuous burst of SF. This illuminating spectrum was calculated using STARBURST99 ([Leitherer et al. 1999](#)) assuming continuous SF with a [Kroupa \(2001\)](#) initial mass function with an upper stellar mass boundary of 100 M_\odot . This is an average spectrum representing the integrated emission of a galaxy with stellar populations of different ages. They produced the spectra for five different stellar metallicities ($Z_\star = 0.05 Z_\odot, 0.2 Z_\odot, 0.4 Z_\odot, Z_\odot$ and $2 Z_\odot$) available for the Geneva evolutionary tracks ([Meynet et al. 1994](#)). AGN photoionization models follows the prescription of starburst models, but with ionizing spectrum with a broken power-law with an index $\alpha = -1.4$ ($S_\nu \propto \nu^\alpha$) between 10 μm and 50 keV, $\alpha = 2.5$ for $\lambda > 10 \mu\text{m}$ and $\alpha = -2.0$ for $E > 50$ keV. The range of the ionization parameters, $\log U = -3.0$ to -1.6 , is that of typical AGN. The remaining input parameters of the model (gas-phase abundances, stopping criteria, gas density range, dust grains, etc.) are the same that we used for the starburst models.

Two independent abundance determinations were obtained for both the O/H and N/O ratios using the optical and the infrared nebular lines. The estimates were derived with the HII-CHI-MISTRY (hereafter HCM; [Pérez-Montero 2014](#)) and the HII-CHI-MISTRY-IR codes⁴ (HCM-IR; [Fernández-Ontiveros et al. 2021](#)). Both are based on the same grid of photoionization models (hereafter models C), computed using CLOUDY ([Ferland et al. 2017](#)) adopting simple stellar population models from POPSTAR as incident radiation field ([Mollá et al. 2009](#)). The models sample a wide range in oxygen abundance ($6.9 < 12 + \log(\text{O}/\text{H}) < 9.1$), nitrogen abundance ($-2.0 < \log(\text{N}/\text{O}) < 0.0$), and ionization parameter ($-4.0 < \log U < -1.5$), assuming a filling factor of 0.1 and a constant electron density of $n_e = 100 \text{ cm}^{-3}$. To compute the optical-based abundances for AGN we used

photoionization models assuming a power-law ionizing continuum ($F_\nu \propto \nu^{\alpha_{\text{OX}}}$; $\alpha_{\text{OX}} = -1.2$) and $n_e = 500 \text{ cm}^{-3}$ (see [Pérez-Montero et al. 2019](#)). We refer to [Fernández-Ontiveros et al. \(2021\)](#) for a comparison of the predicted emission line ratios with the observed ones for a sample of star forming galaxies, showing that the range of variations of the main emission-line ratios of this sample are within the ranges covered by the models.

HCM and HCM-IR perform a Bayesian-like calculation of the $12 + \log(\text{O}/\text{H})$ and the N/O abundances, and the ionization parameter, by comparing the optical (reddening corrected) and infrared nebular lines, respectively, with the predicted values in the grids of photoionization models. The abundance determination does not rely on a single best-fit model, but it is instead based on the Bayesian calculation where all the models contribute to the computation of the abundances. The estimated abundance and its associated uncertainty is then computed from the weighted grid of models, as discussed in [Fernández-Ontiveros et al. \(2021\)](#). The photoionization models provide abundance estimates consistent with the direct method –based on the detection of auroral nebular lines in the optical range– within a scatter of 0.1 dex and 0.2 dex, respectively ([Pérez-Montero 2014](#); [Fernández-Ontiveros et al. 2021](#)).

For the case of AGN, the abundance determinations could not be obtained using HCM-IR due to the lack of hydrogen recombination line measurements in the mid-IR. Humphreys- α is the brightest recombination line in the range covered by *Spitzer*/IRS in the high-spectral resolution mode (9.9–37.1 μm), however it is a weak line ($\sim 1/100$ th of $\text{H}\beta$) and thus it is not reported in most of the works discussed in Section 2.2, where these spectra were analyzed. Therefore, IR-based $12 + \log(\text{O}/\text{H})$ determinations are not available for the AGN in our sample. In this regard, IR-based abundance determinations for AGN will be addressed in a forthcoming work ([Pérez-Díaz et al. in prep.](#)). Nevertheless, a robust estimate of the N/O abundance ratio can be obtained from the $[\text{OIII}]\lambda 52, 88 \mu\text{m}$ and $[\text{NIII}]\lambda 57 \mu\text{m}$ lines, due to the similar ionization structure of these two elements. For this purpose we define the N3O3 parameter, based on the relative intensities of the nitrogen and oxygen lines in the far-IR:

$$\text{N3O3} = \log \left(\frac{I([\text{NIII}]\lambda 57 \mu\text{m})}{I([\text{OIII}]\lambda 52 \mu\text{m}) + I([\text{OIII}]\lambda 88 \mu\text{m})} \right) \quad (4)$$

This parameter was used by [Peng et al. \(2021\)](#) and [Fernández-Ontiveros et al. \(2021\)](#) for the derivation of the N/O relative abundances in star-forming galaxies, and can be also be applied to the case of Narrow Line Region (NLR) in AGN, due to the very low dependence on the excitation conditions of the ionized gas. This is due to the similar ionization structure of the oxygen and nitrogen elements in the nebula. To this aim, we analyzed the predicted values of N3O3 for

⁴ Available at: <https://www.iaa.csic.es/~epm/HII-CHI-mistry.html>

the grid of AGN photoionization models described in Pérez-Montero et al. (2019). As input ionizing source we adopted a double-peak power law with index $\alpha_{UV} = -1.5$, also considering different values for $\alpha_{OX} = -0.8$ and -1.2 , with an electron density of $n_e = 500 \text{ cm}^{-3}$, sampling the same range in metallicity, ionization parameter and N/O mentioned earlier. The N3O3 parameter presents a very tight relation with the N/O abundances in star forming regions (Peng et al. 2021; Fernández-Ontiveros et al. 2021). This is also true under harder radiation fields in AGN, as shown by the linear sequence of AGN models at a fixed $12 + \log(\text{O}/\text{H}) = 8.8$ and $\alpha_{OX} = -1.2$ in Appendix B. Thus, a robust linear relation between these parameters can be extracted. The linear fit to the whole set of models for this value of α_{OX} has a correlation coefficient of 0.91 and results in the following expression:

$$\log(\text{N}/\text{O}) = (0.97 \pm 0.01) \times \text{N3O3} - (0.01 \pm 0.01) \quad (5)$$

Additionally, the analysis for the model grid with $\alpha_{OX} = -0.8$ lead to similar results within the typical observational errors.

5. RESULTS

We discuss the results of the abundance determination through both the optical and IR spectral lines. We use in the following a few diagrams showing various IR line ratios as a function of the metallicity. We also compare both the (O/H) and (N/O) abundance determinations using the two methods.

5.1. Far-IR line ratios as a function of gas-phase metallicity

Following the work of Nagao et al. (2011) and Pereira-Santaella et al. (2017) we present for the HII region/ULIRG galaxies and the dwarf galaxies of our sample, in Fig. 5, the ratio of $(2.2 \times [\text{OIII}]88\mu\text{m} + [\text{OIII}]52\mu\text{m})/[\text{NIII}]57\mu\text{m}$ as a function of the gas-phase metallicity as measured in the optical and expressed in terms of $12 + \log(\text{O}/\text{H})$. The starburst galaxies photoionization models are taken from Pereira-Santaella et al. (2017) (models B in Section 4) and include values of ionization parameter $\log(U) = -2, -3$ and -4 and electron densities with $\log(n_e/\text{cm}^{-3}) = [1, 3]$. These models follow the same relation between N/O and O/H derived by Pilyugin et al. (2014), adopted in Pereira-Santaella et al. (2017) and reported in Eq. (2) of this latter study.

We also show in the same figure (solid line (in green)) a photoionization model (from models C in Section 4) with $\log(U) = -3$, $\log(n_e/\text{cm}^{-3}) = 2$ and a $\log(\text{N}/\text{O}) = -1.54$ for metallicities of $[12 + \log(\text{O}/\text{H})] < 8.09$ and $\log(\text{N}/\text{O}) = 4.21 + 1.47 \times \log(\text{O}/\text{H})$ for metallicities of $[12 + \log(\text{O}/\text{H})] > 8.09$, which corresponds to the Pilyugin et al. (2014) relation between N and O, as well as (green broken lines) the effect of increasing and decreasing, in the lower and upper curve respectively, the $\log(\text{N}/\text{O})$ by 0.35 dex. It appears clear from

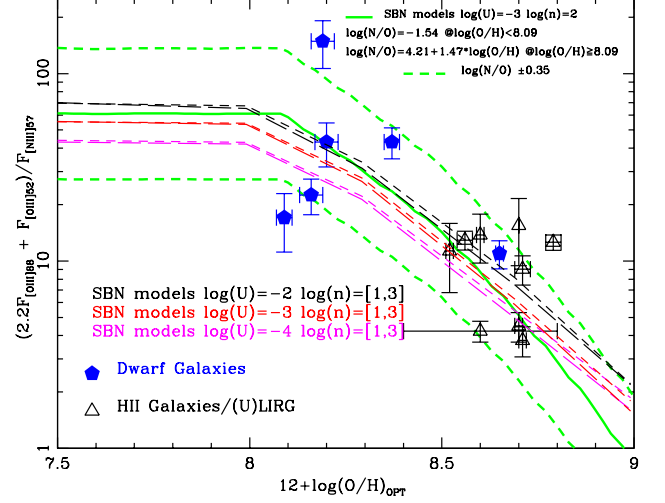


Figure 5. Ratio of $(2.2 \times [\text{OIII}]88\mu\text{m} + [\text{OIII}]52\mu\text{m})/[\text{NIII}]57\mu\text{m}$ as a function of the gas-phase metallicity for the HII region/ULIRG galaxies and the dwarf galaxies of our sample. The photoionization models (models B in Section 4) are taken from Pereira-Santaella et al. (2017) and include values of ionization parameter $\log(U) = -2, -3$ and -4 from the top to the bottom and densities with $\log(n_e/\text{cm}^{-3}) = [1, 3]$. The solid line (in green) represents a photoionization model (models C in Section 4) with $\log(U) = -3$, $\log(n_e/\text{cm}^{-3}) = 2$ and a $\log(\text{N}/\text{O}) = -1.54$ for metallicities of $[12 + \log(\text{O}/\text{H})] < 8.09$ and $\log(\text{N}/\text{O}) = 4.21 + 1.47 \times \log(\text{O}/\text{H})$ for metallicities of $[12 + \log(\text{O}/\text{H})] > 8.09$. The two broken lines (in green) show the effect of increasing and decreasing, respectively, the $\log(\text{N}/\text{O})$ by 0.35 dex.

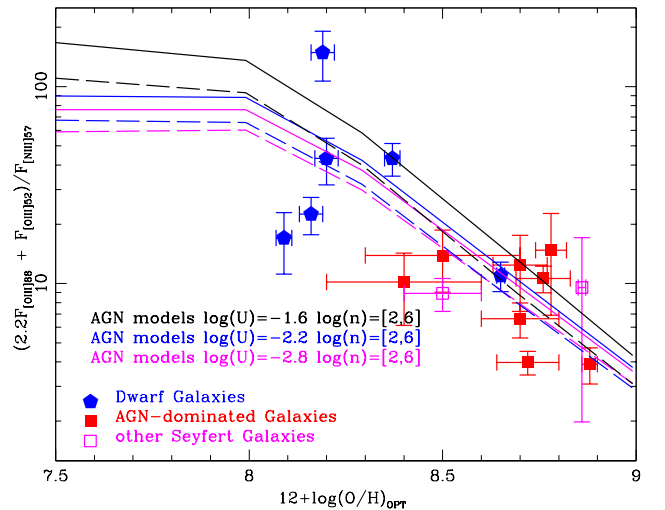


Figure 6. Same as Fig. 5, but with the AGN observations and the relative photoionization models (models B in Section 4) from Pereira-Santaella et al. (2017). The dwarf galaxies observations have been included for comparison.

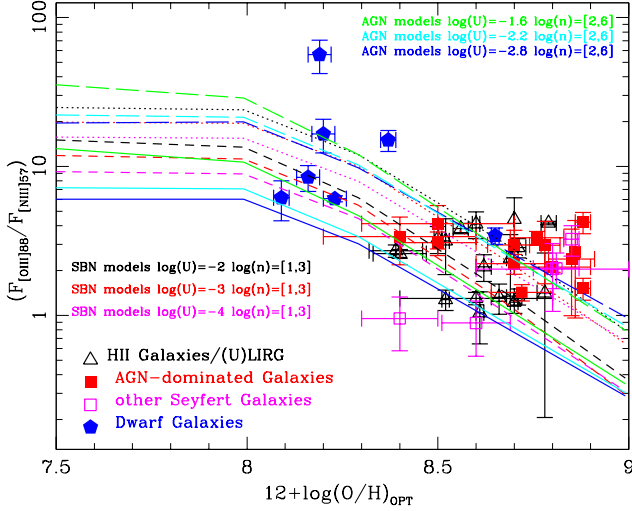


Figure 7. Ratio of $[OIII]88\mu m/[NIII]57\mu m$ as a function of the gas-phase metallicity. The photoionization models (models B in Section 4) are taken from Pereira-Santaella et al. (2017) and include values of ionization potential $\log(U)=-2, -3$ and -4 from the top to the bottom and densities with $\log(n_e/\text{cm}^{-3})=[1,3]$ for the starburst models and ionization potential $\log(U)=-1.6, -2.2$ and -2.8 from the top to the bottom and densities with $\log(n_e/\text{cm}^{-3})=[2,6]$ for the AGN models.

this plot that, to fit most galaxies, an N/O ratio of a factor ~ 2 higher or lower than the solar value is needed. As anticipated in Section 4, the different photoionization models shown in Fig. 5 do agree well, and a slight discrepancy only appears for high metallicities $[12+\log(O/H)] \gtrsim 8.7$. This shows that only minor differences are present in the N/O abundances using the constant pressure models in Pereira-Santaella et al. (2017) and the constant density models used in HCM and HCM-IR.

The same line ratio is presented for the AGN, including also the dwarf galaxies for comparison, in Fig. 6. Here the photoionization model grid (models B in Section 4) includes models with ionization parameter $\sim -2.8 < \log(U) < -1.6$ and densities of $\sim 2.0 < \log(n_e) < 6.0 \text{ cm}^{-3}$. Also in this case the large scatter of the points around the given models could be due to a different value of the N/O ratio.

In Fig. 7, we show the ratio $[OIII]88.3\mu m/[NIII]57.2\mu m$ versus the metallicity for all the galaxies of the sample, including HII region/ULIRG galaxies, dwarf galaxies and AGN. Here both starburst and AGN models (models B in Section 4) are included and the intrinsic spread of the models is larger than in the case of the previous composite line ratio. Also these photoionization models follow the same relation between N/O and O/H derived by (Pilyugin et al. 2014) adopted in Pereira-Santaella et al. (2017).

Fig. 8 shows the $[OIII]88\mu m/[NII]122\mu m$ ratio as a function of the gas-phase metallicity for all galaxies of our sample, compared to the Starburst photoionization models (mod-

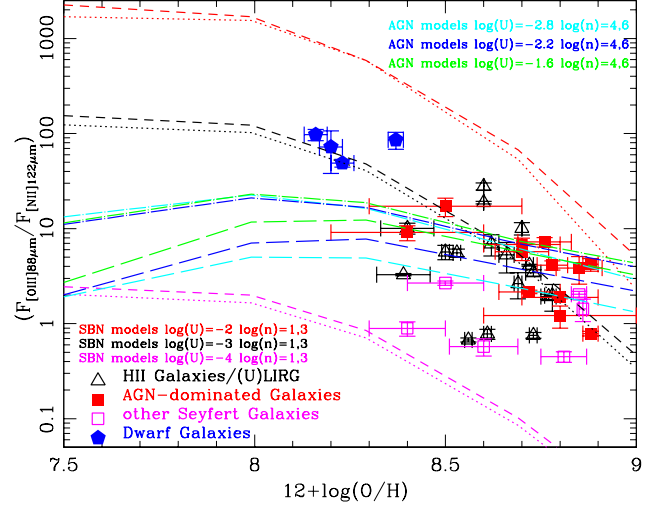


Figure 8. Ratio of $[OIII]88\mu m/[NII]122\mu m$ as a function of the gas-phase metallicity. The photoionization models (models B in Section 4) are taken from Pereira-Santaella et al. (2017) and include values of ionization potential $\log(U)=-2, -3$ and -4 from the top to the bottom and densities with $\log(n_e/\text{cm}^{-3})=[1,3]$ for the starburst models and ionization potential $\log(U)=-1.6, -2.2$ and -2.8 from the top to the bottom and densities with $\log(n_e/\text{cm}^{-3})=[4,6]$ for the AGN models.

els B in Section 4). Also these photoionization models follow the same relation between N/O and O/H derived by Pilyugin et al. (2014) adopted in Pereira-Santaella et al. (2017). One can see from this figure a large spread in the models produced by different ionization parameter. In other words, the determination of the metallicity from a given line ratio is only reliable if we can measure the ionization parameter through other line ratios.

In Fig. 9 we show the $[OIII]88\mu m/[NII]122\mu m$ line ratio as a function of the $[NIII]57\mu m/[NII]122\mu m$ line ratio for both solar and sub-solar abundances (models B in Section 4). As before, the sub-solar value has been set to $Z = 0.4 \times Z_\odot$. We can see from this diagram that only a few objects (4/5 dwarf galaxies) need sub-solar abundances. We also notice that we can read out from the vertical axis a precise estimate of the ionization parameter: assuming, e.g., solar abundances, we can associate a value of $\log(U) = -4$ at a $[OIII]88\mu m/[NII]122\mu m = 0.1$, a value of $\log(U) = -3$ for a ratio ~ 5 and a value of $\log(U) = -2$ at a ratio $\gtrsim 50$. It follows that observations of the three far-IR lines of $[NIII]57\mu m$, $[OIII]88\mu m$ and $[NII]122\mu m$ can break the degeneracy due to the ionization parameter. In other words, placing an observed galaxy in this diagram will give an estimate of the ionization parameter and therefore make possible an estimate of the metallicity, through the use of the diagram in Fig. 8.

5.2. Mid-IR line ratios as a function of gas-phase metallicity

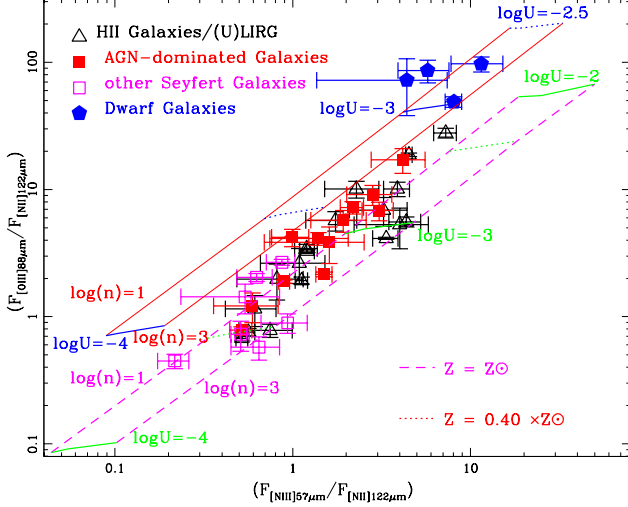


Figure 9. Ratio of $[OIII]88\mu m/[NII]122\mu m$ as a function of the $[NIII]57\mu m/[NII]122\mu m$ line ratio. The photoionization models (models B in Section 4) are taken from [Pereira-Santaella et al. \(2017\)](#) and include values of ionization potential $\log(U)=-2, -3, -3.5$ and -4 from the top to the bottom and densities with $\log(n)=[1,3]$ for the starburst models. For comparison, also the AGN data points have been included. the lower grid assumes solar abundances, while the upper grid indicates models with a sub-solar metallicity of $Z = 0.4 \times Z_{\odot}$.

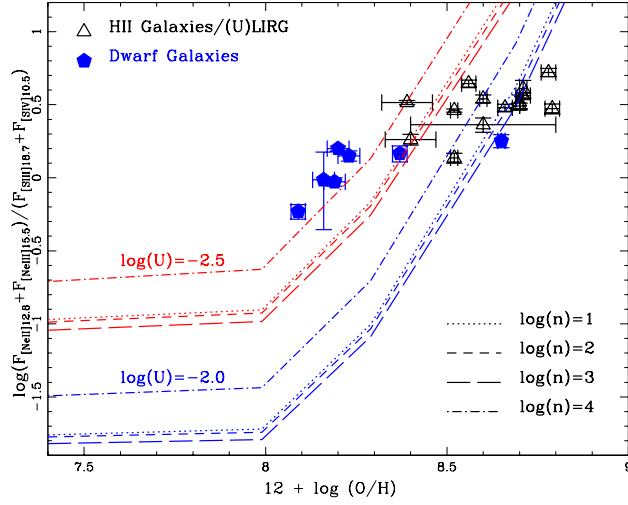


Figure 10. Logarithm of the observed ratio of the sum of $([NeII]12.8\mu m + [NeIII]15.6\mu m)$ to the sum of $([SIII]18.7\mu m + [SIV]10.5\mu m)$ versus the optical metallicity ([Fernández-Ontiveros et al. 2016](#)) for the starburst and dwarf galaxies of our sample. Two sets of CLOUDY photoionization models (models A in Section 4) with $\log(U)=-2.5$ (upper models) and $\log(U)=-2.0$ (lower models) are compared to the data, assuming sulphur depletion at $[12 + \log(O/H)] > 8$, for electron densities in the range of $\log(n)=[1,4]$.

Following the work presented in [Fernández-Ontiveros et al. \(2016, 2017\)](#), we have also considered the ratio of $([NeII]12.8\mu m + [NeIII]15.6\mu m)$ to $([SIII]18.7\mu m + [SIV]10.5\mu m)$ which, as a first approximation, is equal to the total neon to total sulfur ratio if one excludes active galaxies, which can ionize also the $[NeV]$ IR fine structure lines. In Fig. 10 this ratio is shown as a function of the metallicity as computed from the optical emission lines. Starburst galaxies photoionization models (models A in Section 4) with a ionization parameter of $-2.5 < \log(U) < -2.0$ and densities $1 < \log(n_e/\text{cm}^{-3}) < 4$ have been included. These models assume sulphur depletion for $[12 + \log(O/H)] > 8$. It appears evident from this figure that there is a correlation between the neon to sulfur ratio, measured by the $Ne_{23}S_{34}$ index, and the gas-phase metallicity. In conclusion, we confirm the results of [Fernández-Ontiveros et al. \(2016, 2017\)](#) that these line fluxes can be used to measure the metallicity. This is important also because the upcoming mission of the *James Webb Space Telescope* (JWST, [Gardner et al. \(2006\)](#)) will be able to detect these IR fine-structure lines in the local universe and at low redshift ($z \leq 0.8$).

5.3. Metallicities from optical lines versus IR lines

In Fig. 11 the metallicity derived from IR lines, using the method from [Fernández-Ontiveros et al. \(2021\)](#) is compared to the metallicity computed from the optical lines using [Pérez-Montero \(2014\)](#). It is shown in the figure a fit to the data, which agrees within the errors with the one-to-one correlation. It follows that, from the data of our sample of galaxies, there is no significant difference between the determination of the metallicity through optical lines and that one through IR lines.

5.4. N/O ratio from optical lines versus IR lines

In Fig. 12 the $(N/O)_{IR}$ ratio derived from IR lines, using the method of [Fernández-Ontiveros et al. \(2021\)](#) is compared to the $(N/O)_{OPT}$ ratio computed from the optical lines using the work of [Pérez-Montero \(2014\)](#). It appears from this comparison that the N/O ratio computed from the IR lines is on average lower than that one derived from optical lines, especially at high values of N/O ($N/O > -1$). The solar value measured with optical lines $(N/O)_{OPT}(\odot) \sim 0.24$ corresponds, according to the fit, to an IR determined value of $(N/O)_{IR}(\odot) \sim 0.12$, i.e. a factor two lower. A least squares fit to the data results in a slope much flatter than the value of $\alpha = 1$. Considering all star forming galaxies, i.e. the HII galaxies and ULIRGs together with the dwarf galaxies, the fit gives a slope of $\alpha = 0.68 \pm 0.12$, while using all the galaxies of our sample the slope is $\alpha = 0.52 \pm 0.10$.

5.5. N/O abundance ratio

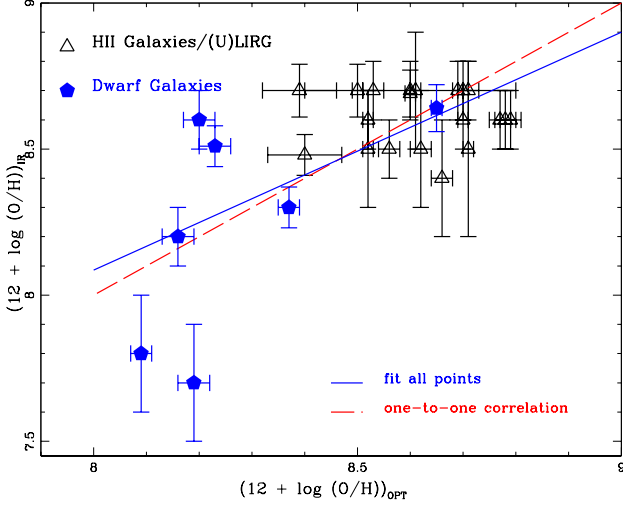


Figure 11. Metallicity derived from IR lines, using the method from Fernández-Ontiveros et al. (2021), is compared to the metallicity computed from the optical lines using Pérez-Montero (2014). The dashed line shows the one-to-one correlation, while the solid line gives the fit: $y = (0.89 \pm 0.15) \cdot x - (0.83 \pm 1.32)$ ($\chi^2 = 0.53$, $R = 0.77$).

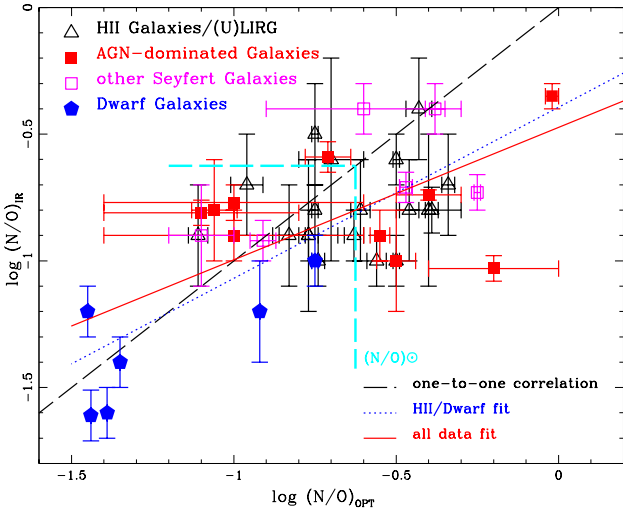


Figure 12. N/O ratio derived from IR, using the method from IR lines of Fernández-Ontiveros et al. (2021) is compared to the N/O ratio computed from the optical lines using Pérez-Montero (2014). The dashed line shows the one-to-one correlation, while the dotted line gives the fit for HII/ULIRG and dwarf galaxies: $y = (0.68 \pm 0.12) \cdot x - (0.39 \pm 0.10)$ ($\chi^2 = 0.93$, $R = 0.76$). A fit to all the data gives (shown as a solid line): $y = (0.52 \pm 0.10) \cdot x - (0.47 \pm 0.08)$ ($\chi^2 = 1.84$, $R = 0.64$). The solar value of $(N/O)_{\odot}=0.24$ is also indicated.

In Fig. 13 the N/O ratio, computed from the IR emission lines using the method developed by Fernández-Ontiveros et al. (2021) and reported in Table 5, is plotted as a func-

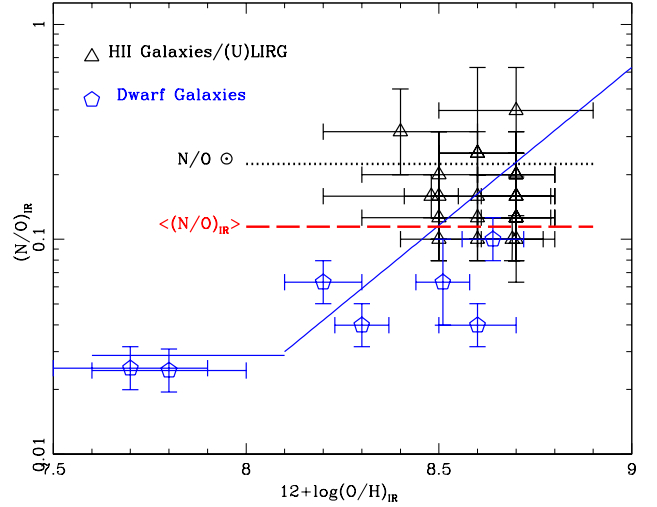


Figure 13. N/O ratio computed from IR emission lines versus the metallicity similarly computed. The solar value of $N/O = 0.24$ has been indicated as well as the average value of the $\log(N/O)_{IR} = -0.94 \pm 0.30$. The Pilyugin et al. (2014) relation between N and O is shown as a solid line, for comparison, which assumes $\log(N/O) = -1.54$ for: $[12 + \log(O/H)] < 8.1$. and $\log(N/O) = 4.21 + 1.47 \times [\log(O/H)]$ for: $[12 + \log(O/H)] > 8.1$.

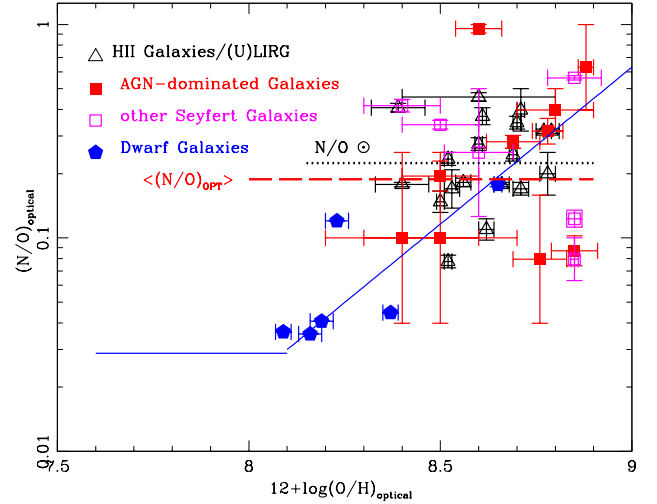


Figure 14. N/O ratio computed from optical emission lines versus the metallicity similarly computed. The solar value of $N/O = 0.24$ has been indicated as the average value of the $\log(N/O)_{OPT} = -0.73 \pm 0.34$. The Pilyugin et al. (2014) relation between N and O is shown as a solid line, for comparison, as given in the caption of Fig. 13.

tion of the metallicity, computed also from the IR emission lines.

In Fig. 14 the N/O ratio, computed from the optical emission lines using the method developed by Pérez-Montero (2014) and reported in Table 5, is plotted as a function of the metallicity, computed also from the optical emission lines.

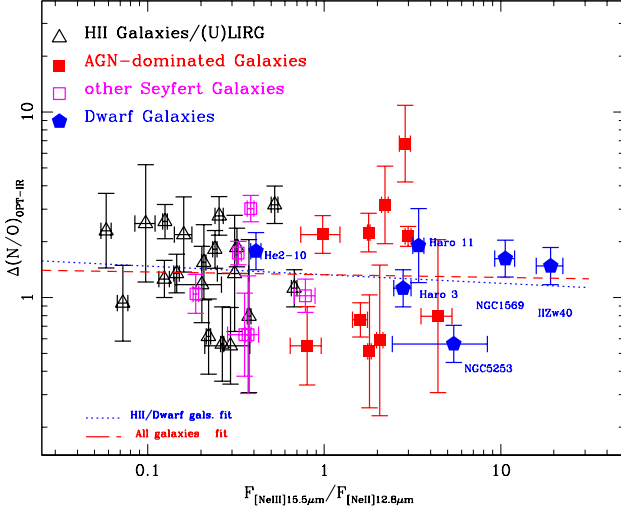


Figure 15. Logarithmic difference between the N/O ratio computed from IR emission lines and the N/O from optical lines versus the $[\text{NeIII}]15.5\mu\text{m}/[\text{NeII}]12.8\mu\text{m}$ line ratio, which measures the gas ionization. The dotted line gives the fit for HII/ULIRG and dwarf galaxies: $y = (-0.05 \pm 0.07) \cdot x + (0.12 \pm 0.05)$ ($\chi^2 = 1.19$, $R = -0.14$). A fit to all the data gives (shown as a dashed line): $y = (-0.01 \pm 0.07) \cdot x + (0.12 \pm 0.05)$ ($\chi^2 = 2.92$, $R = -0.03$).

If we compare the average value of the $\log(\text{N/O})_{\text{IR}} = -0.73 \pm 0.34$ (Fig.13) with the average value of the $\log(\text{N/O})_{\text{OPT}} = -0.94 \pm 0.30$ (Fig.14), we see a large difference of ~ 0.2 dex.

In the following sections we study the possible dependence of the $\Delta(\text{N/O})$ with ionization, density and extinction.

5.5.1. $\Delta(\text{N/O})$ versus ionization

Fig.15 shows the logarithmic difference between the N/O ratio computed from IR emission lines (N/O_{IR}) and the N/O from optical lines (N/O_{OPT}) (hereafter $\Delta(\text{N/O}) = (\text{N/O}_{\text{OPT}} - (\text{N/O})_{\text{IR}})$ versus the $[\text{NeIII}]15.5\mu\text{m}/[\text{NeII}]12.8\mu\text{m}$ line ratio. In this diagram a slight decreasing trend could be present due to the higher $\Delta(\text{N/O})$ values in HII galaxies and (U)LIRGs, albeit the correlation is not statistically significant. Dwarf galaxies are in average consistent with an equal value for the (N/O) and Seyfert galaxies have a high dispersion. A similar diagram is shown in Fig. 16, using the $[\text{NIII}]57\mu\text{m}/[\text{NII}]122\mu\text{m}$ line ratio, however the scatter is larger here due to the lower ionization potential of these lines, which results in a larger confusion along the horizontal axis.

We also present in Fig.17 the $\Delta(\text{N/O})$ plotted as a function of the $[\text{OIV}]26\mu\text{m}/[\text{OIII}]88\mu\text{m}$ line ratio, which covers the largest range in ionization and almost three orders of magnitude in line ratio value from low metallicity dwarf galaxies to AGN. Also in this case the search for a correlation fails because of the large spread of the data, however a slight trend

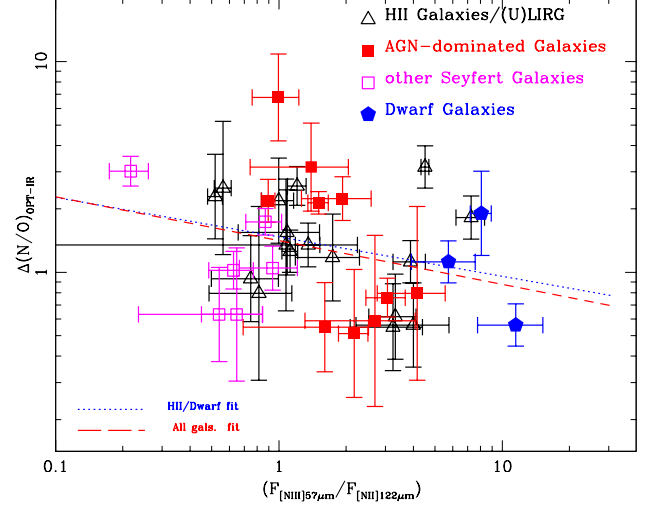


Figure 16. Logarithmic difference between the N/O ratio computed from IR emission lines and the N/O from optical lines versus the $[\text{NIII}]57\mu\text{m}/[\text{NII}]122\mu\text{m}$ line ratio, which measures the gas ionization. The dotted line gives the fit for HII/ULIRG and dwarf galaxies: $y = (-0.18 \pm 0.13) \cdot x + (0.16 \pm 0.06)$ ($\chi^2 = 0.97$, $R = -0.31$). A fit to all the data gives (shown as a dashed line): $y = (-0.21 \pm 0.12) \cdot x + (0.15 \pm 0.05)$ ($\chi^2 = 2.54$, $R = -0.29$).

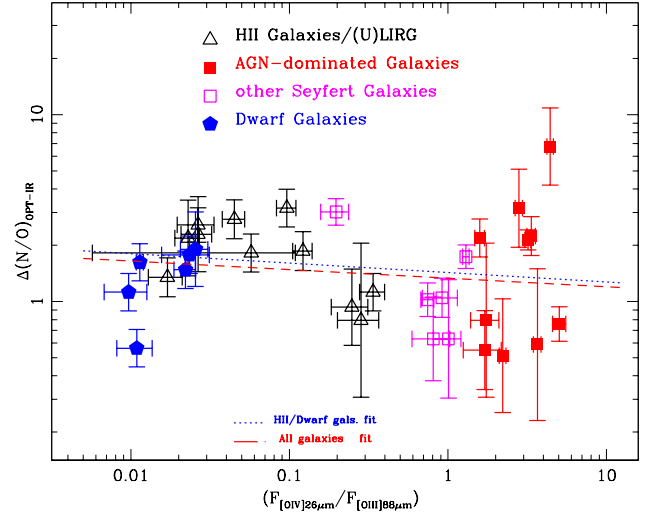


Figure 17. Logarithmic difference between the N/O ratio computed from IR emission lines and the N/O from optical lines versus the $[\text{OIV}]26\mu\text{m}/[\text{OIII}]88\mu\text{m}$ line ratio, which measures the gas ionization. The dotted line gives the fit for HII/ULIRG and dwarf galaxies: $y = (-0.04 \pm 0.10) \cdot x + (0.14 \pm 0.15)$ ($\chi^2 = 0.64$, $R = -0.10$). A fit to all the data gives (shown as a dashed line): $y = (-0.05 \pm 0.05) \cdot x + (0.12 \pm 0.06)$ ($\chi^2 = 2.36$, $R = -0.15$).

of increasing $\Delta(\text{N/O})$ at low gas ionization remains for HII galaxies and (U)LIRGs.

5.5.2. $\Delta(\text{N/O})$ versus density

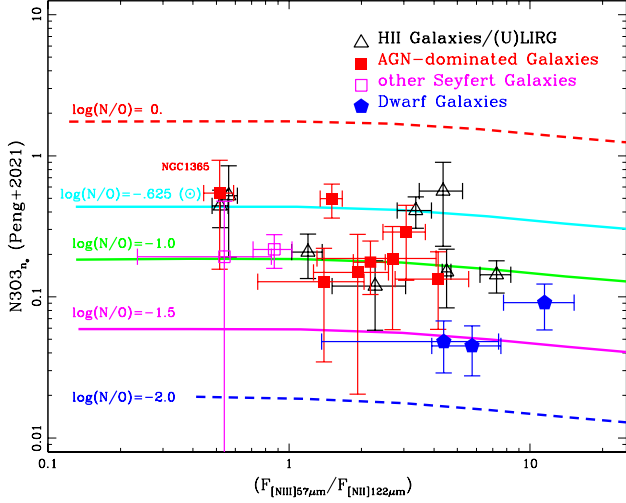


Figure 21. Density-corrected $N3O3n_e$ (Peng et al. 2021) of the sample galaxies as a function of the $[NIII]57\mu m/[NII]122\mu m$ line ratio. The galaxies are divided in the three classes, HII region galaxies/(U)LIRGs, Seyfert galaxies and Dwarf Galaxies. The horizontal lines give the positions of constant N/O ratio as computed from photoionization models.

lines of $[NIII]57\mu m$ and $[OIII]52\mu m$ of 8 galaxies, complemented by *Herschel*-PACS and *Spitzer*-IRS observations of $[OIII]52\mu m$ and $[NeII]12.8\mu m$ and $[NeIII]15.5\mu m$, respectively. They show that the $[NIII]57\mu m/[OIII]52\mu m$ line ratio, denoted $N3O3$, is a physically robust probe of N/O, is insensitive to gas temperature and only weakly dependent on electron density. They also use the observations of the two lines of the $[OIII]52\mu m$ and $88\mu m$ to correct this ratio for the effects of density. We have therefore used this work to derive the density corrected $N3O3n_e$ ratio for our sample of galaxies, and confirm with an independent method our results. The value of $N3O3n_e$ has been derived using the equations (2) and (4) of Peng et al. (2021). We present in Figure 20 the $N3O3n_e$ ratio as a function of the $[NeIII]15.5\mu m/[NeII]12.8\mu m$ line ratio for each galaxy for which we have the observations of the fine-structure lines of $[OIII]52$ and $88\mu m$, $[NIII]57\mu m$, $[NeII]12.8\mu m$ and $[NeIII]15.5\mu m$. In Fig. 21 we show the same $N3O3n_e$ ratio as a function of the $[NIII]57\mu m/[NII]122\mu m$ line ratio. Together with the data points of our sample of galaxies, we also show in these figures the lines of constant N/O ratio ($\log(N/O)=[-2, 0]$) in analogy to the Fig. 3 of Peng et al. (2021). The lines at fixed (N/O) ratio have been taken from CLOUDY photoionization models for stellar populations described in section 4, adopting a solar O/H abundance, an ionization parameter in the range of $\log(U)=[-4.0, -1.5]$ and electron density fixed at the value of $\log(n_e)=2.0$ (cm^{-3}).

6. DISCUSSION

One of the main results in this study is the difference found between optical and IR determinations of the N/O abundance in galaxies. Although the scatter in Fig. 12 is relatively large, a systematic difference is observed for those galaxies with N/O abundances above $\gtrsim -0.6$ dex determined from the optical lines. These galaxies, including both star-forming galaxies and AGN, show IR-based N/O abundances which are about a factor 2-3 lower when compared with the optical estimates, in agreement with the results obtained by Peng et al. (2021) for a sample of 8 galaxies. This difference is in contrast with the overall agreement found between the optical and IR O/H abundances determinations in Fig. 11. Optical and IR methods are consistent within ~ 0.2 dex scatter when O/H abundances are derived (Fernández-Ontiveros et al. 2021), but differ in the N/O values obtained.

Among the different possibilities to explain this discrepancy we investigated three main scenarios that could affect the optical line tracers: differences in the ionization structure, contamination by Diffuse Ionized Gas (DIG; e.g. Vale Asari et al. 2019), and dust extinction. None of these hypothesis seem to explain the observed discrepancy. A difference in the ionization structure could result in lower N/O ratios for the IR tracers, because these lines probe higher ionization gas (O^{2+} and N^{2+}) located closer to massive stars, where the primary production of nitrogen could be prevalent, resulting in lower N/O when compared to the optical lines that trace lower ionization gas (O^+ and N^+) with a higher nitrogen enrichment from a secondary origin. However Figs. 15 and 16 show a flat distribution when the ratio between N/O optical and IR estimates is compared with the strength of the radiation field traced by the $[NeIII]15.6\mu m/[NeII]12.8\mu m$ and $[NIII]57\mu m/[NII]122\mu m$ ratios, respectively. That is, the star-forming galaxies with a strong radiation field (i.e. low-metallicity dwarf galaxies) are scattered around optical-to-IR N/O ratios of ~ 1 in Fig. 15, while solar-like starburst galaxies with the weakest radiation fields are tentatively shifted to ratios around ~ 2 .

An alternative explanation is the contamination by DIG affecting the optical lines in these galaxies. The presence of hot and low-density gas in the ISM was proposed by Peng et al. (2021) as a possible cause of the optical-to-IR discrepancy. In this scenario, the DIG contamination would be stronger for the lower excitation species of O^+ and N^+ . As a matter of fact, the DIG emission can account for $\sim 30\%$ of the optical line fluxes of the $[OII]\lambda\lambda 3727, 3729$ and the $[NII]\lambda\lambda 6548, 6584$ doublets. As opposite, the DIG contamination on the higher ionization transitions in the IR would be negligible. Additionally, this difference would be enhanced for large galaxies with an old stellar population that could have enriched the DIG with secondary nitrogen. We test this hypothesis by comparing the N/O optical-to-IR ratio with the gas density derived from the $[SII]\lambda\lambda 6716, 6731$ doublet in

Fig. 18. The sulfur doublet probes the gas density in the same ISM domain where $[\text{NII}]\lambda\lambda 6548, 6584$ lines are produced, and therefore it should be sensitive to the presence of DIG due to the low densities associated with this component. However, no correlation is found in Fig. 18, meaning that the discrepancies in the $\Delta(\text{N/O})$ are not associated with a low-density gas component. Additionally, excluding the sulfur lines in the abundance computation with HCM does not result in significant differences in the N/O ratios obtained, as would be expected for DIG contamination affecting the sulfur line fluxes (e.g. Pilyugin et al. 2018). Thus, we conclude that DIG contamination does not significantly affect the optical line fluxes.

The third scenario is the possible effect of dust obscuration on the optical-based determinations. Although optical line fluxes were corrected by extinction estimated from the observed Balmer decrement values, uncorrected obscuration affecting the $[\text{OII}]\lambda\lambda 3727, 3729$ doublet would particularly affect the optical N/O abundances, since the nitrogen lines are less affected by dust attenuation. This possibility is investigated in Fig. 19, where the $\Delta(\text{N/O})$ is compared with the optical extinction A_V values derived from the Balmer decrement. No significant trend is observed, suggesting that uncorrected residual extinction cannot explain the differences seen in the N/O abundances.

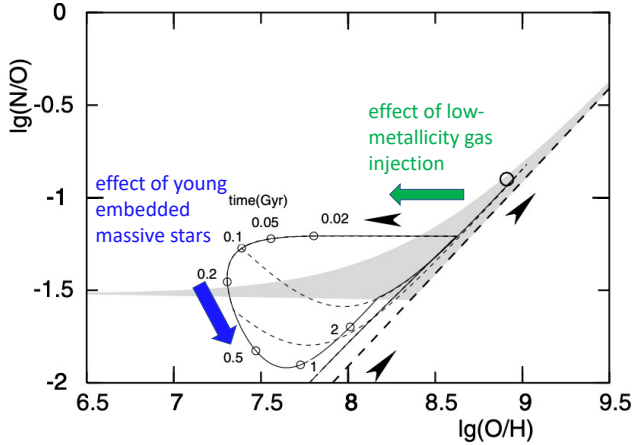


Figure 22. The time evolution of the extreme model from Köppen & Hensler (2005) with an infall rate of 100 galaxy masses per Gyr, starting at an age of 5 Gyr. The upper arrow indicated the effect of low-metallicity gas injection, while the lower arrow the effect of young embedded massive stars. The decrease in the N/O ratio (downward arrow) is due to the primary production of young massive stars, preferentially producing oxygen compared to nitrogen. Adapted from fig. 3 of Köppen & Hensler (2005).

An alternative explanation, more speculative, would imply that optical transitions are completely missing the embedded star forming regions for the galaxies in our sample. Consequently, the optical lines would trace preferentially the gas

in more external regions, which would be more exposed to enrichment with secondary nitrogen and biased against dust embedded massive stars. As opposite, the gas traced by the IR transitions would be associated to lower N/O ratios due to the contribution from massive stars. In this scenario, the differences between optical and IR N/O abundances in galaxies would be a consequence of the chemical evolution process that may follow episodes of low-metallicity gas accretion from the circumgalactic medium or the external disk of the galaxy. This process has been modeled by Köppen & Hensler (2005), showing that the rapid decrease in oxygen abundance after the gas infall is followed by a sharp decrease in the N/O ratio due to the yields of the newly formed massive stars. The O/H and N/O increase at a later time due to the ongoing star formation and the secondary production of nitrogen from intermediate-mass stars, closing the loop in the N/O–O/H diagram (see Fig. 22). As a matter of fact, evidence of gas accretion affecting the N/O ratios in the disks of nearby star forming galaxies has been recently discovered (Luo et al. 2021). Local variations in the star formation efficiency could also play a role to explain the different N/O ratios observed (Mollá et al. 2006; Florido et al. 2015; Kumari et al. 2018). If confirmed, this result would imply that the N/O ratios measured with IR lines are more genuine than those in the optical, since they reflect the chemical abundances in the ISM gas phase including also the obscured regions not detected by optical tracers.

Although the cause of the optical-to-IR discrepancy is still unknown, we favor the abundances derived from the IR lines because these are virtually independent of dust and temperature effects. The optical lines emissivities present a strong dependency with the gas temperature (e.g. fig. 1 in Fernández-Ontiveros et al. 2021) and could be affected by, e.g., inhomogeneities in the gas nebula (Peimbert 1967), while the IR lines can provide more robust abundance estimates (e.g. Vermeij & van der Hulst 2002; Dors et al. 2013). On the other hand, our IR N/O determinations based on photoionization models are in agreement with the values obtained using the density-corrected $\text{N3O3}n_e$ parameter introduced by Peng et al. (2021), as shown in Figs. 20 and 21. The optical-to-IR abundance discrepancy analyzed in this work warns on the use of optical tracers to study the N/O abundances in galaxies at high redshift, e.g. using future *James Webb Space Telescope* observations of their restframe optical spectrum. These should be compared with measurements derived from the far-IR transitions redshifted in the submm range and observed with ALMA or future facilities in this spectral range, when available.

7. SUMMARY

We summarize here the main results of this paper.

1. We have reduced and analyzed new and archival spectra of the [OIII]52 μ m and [NIII]57 μ m lines in 29 galaxies collected by the SOFIA FIFI-LS spectrometer.
2. Using literature data from *Herschel*-PACS and ISO-LWS, we have assembled a sample of 47 galaxies, including 21 HII region/(U)LIRG galaxies, 19 Seyfert galaxies, including one LINER and 7 dwarf galaxies, for which we have full coverage of the [NIII]57 μ m line and at least one of the two [OIII] lines (at 52 μ m or 88 μ m).
3. We have complemented the [NIII] and [OIII] far-IR lines observations of this sample with the mid- and far-IR lines useful for the characterization of the sample and the analysis carried out in this work aimed at the determination of the metallicity using IR spectra. In particular we used the *Spitzer*-IRS and the *Herschel*-PACS spectra where available for the galaxies of the sample.
4. We have exploited the use of various line ratios, namely the $(2.2 \times [\text{OIII}]88\mu\text{m} + [\text{OIII}]52\mu\text{m})/[\text{NIII}]57\mu\text{m}$ ratio, the $[\text{OIII}]88\mu\text{m}/[\text{NIII}]57\mu\text{m}$ ratio, the $[\text{OIII}]88\mu\text{m}/[\text{NII}]122\mu\text{m}$ ratio, and the $([\text{NeII}]12.8\mu\text{m} + [\text{NeIII}]15.6\mu\text{m})$ to $([\text{SIII}]18.7\mu\text{m} + [\text{SIV}]10.5\mu\text{m})$ composite ratio, to map with the use of photoionization models their dependence with the metallicity, expressed as $[12 + \log(\text{O}/\text{H})]$. In other words, we assessed the use of these line ratios to measure the metallicity in galaxies.
5. We find that the determination of the (O/H) ratio with optical emission lines is consistent, within the errors, with its determination through IR fine-structure lines.
6. We find, as opposite, that the determination of the (N/O) abundance through optical lines is significantly different from its determination from the IR lines, especially for high values of (N/O) ($\text{N/O} \gtrsim -0.8$).
7. We explored if a difference in the ionization structure mapped by the IR lines, which trace higher ionization gas (O^{2+} and N^{2+}) with respect to the one mapped in the optical (O^+ and N^+), could result in lower N/O ratios for the IR lines. However we do not find a significant correlation between the $\Delta(\text{N/O}) = (\text{N/O})_{\text{OPT}} - (\text{N/O})_{\text{IR}}$ and the ionization indices.

8. We explored the possibility that the presence of diffuse ionized gas (DIG) in the ISM of galaxies could be responsible for this difference, by searching correlations between the $\Delta(\text{N/O})$ and the electron density as measured from different tracers (the [SII] $\lambda\lambda 6716, 6731$ lines, the [SIII]18 μ m and 33 μ m lines and the [OIII]52 μ m and 88 μ m lines), but we do not find any statistically significant correlation.
9. We also searched the correlation between the $\Delta(\text{N/O})$ and the optical extinction A_V , to search for a systematic underestimation of the correction for optical extinction of the optical lines used to determine the (N/O) ratio, but we did not find any correlation.
10. We speculatively suggest that accretion of metal-poor gas from the circumgalactic medium could provide an explanation for the observed $\Delta(\text{N/O})$, because the rapid decrease of the oxygen abundance during infall is followed by a decrease of the N/O ratio due to the primary production of young - possibly embedded - massive stars, which are preferentially traced by the IR diagnostics, while optical diagnostics would better trace the secondary production, when both N/O and O/H abundance ratios will increase.

Facilities: SOFIA(FIFI-LS), Spitzer(IRS), Herschel(PACS)

This work is based on observations made with the NASA/DLR Stratospheric Observatory for Infrared Astronomy (SOFIA). SOFIA is jointly operated by the Universities Space Research Association, Inc. (USRA), under NASA contract NNA17BF53C, and the Deutsches SOFIA Institut (DSI) under DLR contract 50 OK 0901 to the University of Stuttgart. We thank the anonymous referee, who helped to improve this paper. JAFO and LS acknowledge financial support by the Agenzia Spaziale Italiana (ASI) under the research contract 2018-31-HH0. MPS acknowledges support from the Comunidad de Madrid through the Atracción de Talento Investigador Grant 2018-T1/TIC-11035 and PID2019-105423GA-I00 (MCIU/AEI/FEDER,UE). We acknowledge financial support from the NASA/SOFIA grant USRA 07-0239.

REFERENCES

Alonso-Herrero, A., García-Marín, M., Rodríguez Zaurín, J., et al. 2010, A&A, 522, A7, doi: [10.1051/0004-6361/201014746](https://doi.org/10.1051/0004-6361/201014746)

Amorín, R. O., Pérez-Montero, E., & Vílchez, J. M. 2010, ApJL, 715, L128, doi: [10.1088/2041-8205/715/2/L128](https://doi.org/10.1088/2041-8205/715/2/L128)

- Armus, L., Charmandaris, V., Bernard-Salas, J., et al. 2007, *ApJ*, 656, 148, doi: [10.1086/510107](https://doi.org/10.1086/510107)
- Bernard-Salas, J., Pottasch, S. R., Beintema, D. A., & Wesselius, P. R. 2001, *A&A*, 367, 949, doi: [10.1051/0004-6361:20000435](https://doi.org/10.1051/0004-6361:20000435)
- Brauher, J. R., Dale, D. A., & Helou, G. 2008, *ApJS*, 178, 280, doi: [10.1086/590249](https://doi.org/10.1086/590249)
- Calzetti, D., Harris, J., Gallagher, John S., I., et al. 2004, *AJ*, 127, 1405, doi: [10.1086/382095](https://doi.org/10.1086/382095)
- Clegg, P. E., Ade, P. A. R., Armand, C., et al. 1996, *A&A*, 315, L38
- Colditz, S., Looney, L. W., Bigiel, F., et al. 2020, in Society of Photo-Optical Instrumentation Engineers (SPIE) Conference Series, Vol. 11453, Society of Photo-Optical Instrumentation Engineers (SPIE) Conference Series, 1145334, doi: [10.1117/12.2560120](https://doi.org/10.1117/12.2560120)
- Cormier, D., Madden, S. C., Lebouteiller, V., et al. 2015, *A&A*, 578, A53, doi: [10.1051/0004-6361/201425207](https://doi.org/10.1051/0004-6361/201425207)
- Cormier, D., Abel, N. P., Hony, S., et al. 2019, *A&A*, 626, A23, doi: [10.1051/0004-6361/201834457](https://doi.org/10.1051/0004-6361/201834457)
- Dale, D. A., Smith, J. D. T., Armus, L., et al. 2006, *ApJ*, 646, 161, doi: [10.1086/504835](https://doi.org/10.1086/504835)
- De Breuck, C., Weiß, A., Béthermin, M., et al. 2019, *A&A*, 631, A167, doi: [10.1051/0004-6361/201936169](https://doi.org/10.1051/0004-6361/201936169)
- de Graauw, T., Haser, L. N., Beintema, D. A., et al. 1996, *A&A*, 315, L49
- Díaz-Santos, T., Armus, L., Charmandaris, V., et al. 2017, *ApJ*, 846, 32, doi: [10.3847/1538-4357/aa81d7](https://doi.org/10.3847/1538-4357/aa81d7)
- Dopita, M. A., & Evans, I. N. 1986, *ApJ*, 307, 431, doi: [10.1086/164432](https://doi.org/10.1086/164432)
- Dors, O. L., Cardaci, M. V., Hägele, G. F., et al. 2015, *MNRAS*, 453, 4102, doi: [10.1093/mnras/stv1916](https://doi.org/10.1093/mnras/stv1916)
- Dors, O. L., Hägele, G. F., Cardaci, M. V., et al. 2013, *MNRAS*, 432, 2512, doi: [10.1093/mnras/stt610](https://doi.org/10.1093/mnras/stt610)
- Ferland, G. J., Chatzikos, M., Guzmán, F., et al. 2017, *RMxAA*, 53, 385. <https://arxiv.org/abs/1705.10877>
- Fernández-Ontiveros, J. A., Pérez-Montero, E., Vílchez, J. M., Amorín, R., & Spinoglio, L. 2021, arXiv e-prints, arXiv:2103.09253. <https://arxiv.org/abs/2103.09253>
- Fernández-Ontiveros, J. A., Spinoglio, L., Pereira-Santaella, M., et al. 2016, *ApJS*, 226, 19, doi: [10.3847/0067-0049/226/2/19](https://doi.org/10.3847/0067-0049/226/2/19)
- Fernández-Ontiveros, J. A., Armus, L., Baes, M., et al. 2017, *PASA*, 34, e053, doi: [10.1017/pasa.2017.43](https://doi.org/10.1017/pasa.2017.43)
- Fischer, C., Beckmann, S., Bryant, A., et al. 2018, *Journal of Astronomical Instrumentation*, 7, 1840003, doi: [10.1142/S2251171718400032](https://doi.org/10.1142/S2251171718400032)
- Florido, E., Zurita, A., Pérez, I., et al. 2015, *A&A*, 584, A88, doi: [10.1051/0004-6361/201526191](https://doi.org/10.1051/0004-6361/201526191)
- Gardner, J. P., Mather, J. C., Clampin, M., et al. 2006, *SSRv*, 123, 485, doi: [10.1007/s11214-006-8315-7](https://doi.org/10.1007/s11214-006-8315-7)
- Griffin, M. J., Abergel, A., Abreu, A., et al. 2010, *A&A*, 518, L3, doi: [10.1051/0004-6361/201014519](https://doi.org/10.1051/0004-6361/201014519)
- Henry, A., Scarlata, C., Domínguez, A., et al. 2013, *ApJL*, 776, L27, doi: [10.1088/2041-8205/776/2/L27](https://doi.org/10.1088/2041-8205/776/2/L27)
- Herrera-Camus, R., Sturm, E., Graciá-Carpio, J., et al. 2018, *ApJ*, 861, 94, doi: [10.3847/1538-4357/aac0f6](https://doi.org/10.3847/1538-4357/aac0f6)
- Hogarth, L., Amorín, R., Vílchez, J. M., et al. 2020, *MNRAS*, 494, 3541, doi: [10.1093/mnras/staa851](https://doi.org/10.1093/mnras/staa851)
- Houck, J. R., Roellig, T. L., van Cleve, J., et al. 2004, *ApJS*, 154, 18, doi: [10.1086/423134](https://doi.org/10.1086/423134)
- Imanishi, M., Maiolino, R., & Nakagawa, T. 2010, *ApJ*, 709, 801, doi: [10.1088/0004-637X/709/2/801](https://doi.org/10.1088/0004-637X/709/2/801)
- Inami, H., Armus, L., Charmandaris, V., et al. 2013, *ApJ*, 777, 156, doi: [10.1088/0004-637X/777/2/156](https://doi.org/10.1088/0004-637X/777/2/156)
- Izotov, Y. I., & Thuan, T. X. 1998, *ApJ*, 500, 188, doi: [10.1086/305698](https://doi.org/10.1086/305698)
- Izotov, Y. I., Thuan, T. X., & Lipovetsky, V. A. 1994, *ApJ*, 435, 647, doi: [10.1086/174843](https://doi.org/10.1086/174843)
- Kessler, M. F., Steinz, J. A., Anderegg, M. E., et al. 1996, *A&A*, 500, 493
- Kewley, L. J., & Ellison, S. L. 2008, *ApJ*, 681, 1183, doi: [10.1086/587500](https://doi.org/10.1086/587500)
- Kobulnicky, H. A., & Skillman, E. D. 1996, *ApJ*, 471, 211, doi: [10.1086/177964](https://doi.org/10.1086/177964)
- Köppen, J., & Hensler, G. 2005, *A&A*, 434, 531, doi: [10.1051/0004-6361:20042266](https://doi.org/10.1051/0004-6361:20042266)
- Kroupa, P. 2001, *MNRAS*, 322, 231, doi: [10.1046/j.1365-8711.2001.04022.x](https://doi.org/10.1046/j.1365-8711.2001.04022.x)
- Kumari, N., James, B. L., Irwin, M. J., Amorín, R., & Pérez-Montero, E. 2018, *MNRAS*, 476, 3793, doi: [10.1093/mnras/sty402](https://doi.org/10.1093/mnras/sty402)
- Leitherer, C., Schaerer, D., Goldader, J. D., et al. 1999, *ApJS*, 123, 3, doi: [10.1086/313233](https://doi.org/10.1086/313233)
- Lequeux, J., Peimbert, M., Rayo, J. F., Serrano, A., & Torres-Peimbert, S. 1979, *A&A*, 500, 145
- Liu, X. W., Barlow, M. J., Cohen, M., et al. 2001, *MNRAS*, 323, 343, doi: [10.1046/j.1365-8711.2001.04180.x](https://doi.org/10.1046/j.1365-8711.2001.04180.x)
- Luo, Y., Heckman, T., Hwang, H.-C., et al. 2021, *ApJ*, 908, 183, doi: [10.3847/1538-4357/abd1df](https://doi.org/10.3847/1538-4357/abd1df)
- Ly, C., Malkan, M. A., Rigby, J. R., & Nagao, T. 2016, *ApJ*, 828, 67, doi: [10.3847/0004-637X/828/2/67](https://doi.org/10.3847/0004-637X/828/2/67)
- Madden, S. C., Rémy-Ruyer, A., Galametz, M., et al. 2013, *PASP*, 125, 600, doi: [10.1086/671138](https://doi.org/10.1086/671138)
- Maiolino, R., & Mannucci, F. 2019, *A&A Rv*, 27, 3, doi: [10.1007/s00159-018-0112-2](https://doi.org/10.1007/s00159-018-0112-2)
- Meléndez, M., Kraemer, S. B., Weaver, K. A., & Mushotzky, R. F. 2011, *ApJ*, 738, 6, doi: [10.1088/0004-637X/738/1/6](https://doi.org/10.1088/0004-637X/738/1/6)
- Meynet, G., Maeder, A., Schaller, G., Schaerer, D., & Charbonnel, C. 1994, *A&AS*, 103, 97
- Mollá, M., García-Vargas, M. L., & Bressan, A. 2009, *MNRAS*, 398, 451, doi: [10.1111/j.1365-2966.2009.15160.x](https://doi.org/10.1111/j.1365-2966.2009.15160.x)

- Mollá, M., Vílchez, J. M., Gavilán, M., & Díaz, A. I. 2006, *MNRAS*, 372, 1069, doi: [10.1111/j.1365-2966.2006.10892.x](https://doi.org/10.1111/j.1365-2966.2006.10892.x)
- Moore, D., & Cohen, R. D. 1994, *ApJ*, 433, 602, doi: [10.1086/174670](https://doi.org/10.1086/174670)
- Nagao, T., Maiolino, R., & Marconi, A. 2006, *A&A*, 459, 85, doi: [10.1051/0004-6361:20065216](https://doi.org/10.1051/0004-6361:20065216)
- Nagao, T., Maiolino, R., Marconi, A., & Matsuhara, H. 2011, *A&A*, 526, A149, doi: [10.1051/0004-6361/201015471](https://doi.org/10.1051/0004-6361/201015471)
- Pearson, C., Rigopoulou, D., Hurley, P., et al. 2016, *ApJS*, 227, 9, doi: [10.3847/0067-0049/227/1/9](https://doi.org/10.3847/0067-0049/227/1/9)
- Peimbert, M. 1967, *ApJ*, 150, 825, doi: [10.1086/149385](https://doi.org/10.1086/149385)
- Peng, B., Lamarche, C., Stacey, G. J., et al. 2021, *ApJ*, 908, 166, doi: [10.3847/1538-4357/abd4e2](https://doi.org/10.3847/1538-4357/abd4e2)
- Pereira-Santaella, M., Rigopoulou, D., Farrah, D., Lebouteiller, V., & Li, J. 2017, *MNRAS*, 470, 1218, doi: [10.1093/mnras/stx1284](https://doi.org/10.1093/mnras/stx1284)
- Perez, J., Michel-Dansac, L., & Tissera, P. B. 2011, *MNRAS*, 417, 580, doi: [10.1111/j.1365-2966.2011.19300.x](https://doi.org/10.1111/j.1365-2966.2011.19300.x)
- Pérez-Montero, E. 2014, *MNRAS*, 441, 2663, doi: [10.1093/mnras/stu753](https://doi.org/10.1093/mnras/stu753)
- Pérez-Montero, E., & Contini, T. 2009, *MNRAS*, 398, 949, doi: [10.1111/j.1365-2966.2009.15145.x](https://doi.org/10.1111/j.1365-2966.2009.15145.x)
- Pérez-Montero, E., Dors, O. L., Vílchez, J. M., et al. 2019, *MNRAS*, 489, 2652, doi: [10.1093/mnras/stz2278](https://doi.org/10.1093/mnras/stz2278)
- Pérez-Montero, E., & Vílchez, J. M. 2009, *MNRAS*, 400, 1721, doi: [10.1111/j.1365-2966.2009.15590.x](https://doi.org/10.1111/j.1365-2966.2009.15590.x)
- Pérez-Montero, E., Contini, T., Lamareille, F., et al. 2013, *A&A*, 549, A25, doi: [10.1051/0004-6361/201220070](https://doi.org/10.1051/0004-6361/201220070)
- Pilbratt, G. L., Riedinger, J. R., Passvogel, T., et al. 2010, *A&A*, 518, L1, doi: [10.1051/0004-6361/201014759](https://doi.org/10.1051/0004-6361/201014759)
- Pilyugin, L. S., Grebel, E. K., & Kniazev, A. Y. 2014, *AJ*, 147, 131, doi: [10.1088/0004-6256/147/6/131](https://doi.org/10.1088/0004-6256/147/6/131)
- Pilyugin, L. S., Grebel, E. K., Zinchenko, I. A., et al. 2018, *A&A*, 613, A1, doi: [10.1051/0004-6361/201732185](https://doi.org/10.1051/0004-6361/201732185)
- Pilyugin, L. S., & Thuan, T. X. 2007, *ApJ*, 669, 299, doi: [10.1086/521597](https://doi.org/10.1086/521597)
- Pilyugin, L. S., Thuan, T. X., & Vílchez, J. M. 2003, *A&A*, 397, 487, doi: [10.1051/0004-6361:20021458](https://doi.org/10.1051/0004-6361:20021458)
- Poglitsch, A., Waelkens, C., Geis, N., et al. 2010, *A&A*, 518, L2, doi: [10.1051/0004-6361/201014535](https://doi.org/10.1051/0004-6361/201014535)
- Pottasch, S. R., & Beintema, D. A. 1999, *A&A*, 347, 975
- Spinoglio, L., & Malkan, M. A. 1992, *ApJ*, 399, 504, doi: [10.1086/171943](https://doi.org/10.1086/171943)
- Tem, P., Marcum, P. M., Young, E., et al. 2014, *ApJS*, 212, 24, doi: [10.1088/0067-0049/212/2/24](https://doi.org/10.1088/0067-0049/212/2/24)
- Torrey, P., Cox, T. J., Kewley, L., & Hernquist, L. 2012, *ApJ*, 746, 108, doi: [10.1088/0004-637X/746/1/108](https://doi.org/10.1088/0004-637X/746/1/108)
- Tremonti, C. A., Heckman, T. M., Kauffmann, G., et al. 2004, *ApJ*, 613, 898, doi: [10.1086/423264](https://doi.org/10.1086/423264)
- Tsujimoto, T., & Bekki, K. 2011, *A&A*, 530, A78, doi: [10.1051/0004-6361/201016210](https://doi.org/10.1051/0004-6361/201016210)
- Vacca, W., Clarke, M., Perera, D., Fadda, D., & Holt, J. 2020, in *Astronomical Society of the Pacific Conference Series*, Vol. 527, *Astronomical Society of the Pacific Conference Series*, ed. R. Pizzo, E. R. Deul, J. D. Mol, J. de Plaa, & H. Verkouter, 547
- Vale Asari, N., Couto, G. S., Cid Fernandes, R., et al. 2019, *MNRAS*, 489, 4721, doi: [10.1093/mnras/stz2470](https://doi.org/10.1093/mnras/stz2470)
- Veilleux, S., Rupke, D. S. N., Kim, D. C., et al. 2009, *ApJS*, 182, 628, doi: [10.1088/0067-0049/182/2/628](https://doi.org/10.1088/0067-0049/182/2/628)
- Vermeij, R., & van der Hulst, J. M. 2002, *A&A*, 391, 1081, doi: [10.1051/0004-6361:20020864](https://doi.org/10.1051/0004-6361:20020864)
- Vila-Costas, M. B., & Edmunds, M. G. 1993, *MNRAS*, 265, 199, doi: [10.1093/mnras/265.1.199](https://doi.org/10.1093/mnras/265.1.199)
- Vílchez, J. M., & Pagel, B. E. J. 1988, *MNRAS*, 231, 257, doi: [10.1093/mnras/231.2.257](https://doi.org/10.1093/mnras/231.2.257)
- Vincenzo, F., Belfiore, F., Maiolino, R., Matteucci, F., & Ventura, P. 2016, *MNRAS*, 458, 3466, doi: [10.1093/mnras/stw532](https://doi.org/10.1093/mnras/stw532)
- Werner, M. W., Roellig, T. L., Low, F. J., et al. 2004, *ApJS*, 154, 1, doi: [10.1086/422992](https://doi.org/10.1086/422992)
- Xia, J., Malkan, M. A., Ross, N. R., & Ancheta, A. J. 2018, *ApJ*, 869, 138, doi: [10.3847/1538-4357/aaedc2](https://doi.org/10.3847/1538-4357/aaedc2)

Table 1. Journal of the SOFIA FIFI-LS observations

Target	RA	dec	z	Type	AOR-ID	Mission-ID	PI	line	T_{exp} (s)
(1)	(2)	(3)	(4)	(5)	(6)	(7)	(8)	(9)	(10)
MCG+12-02-001	00h 54m 03.6s	+73d 05m 12s	0.015698	ULIRG	07_0209_11	2019-05-01_FLF562	G. Stacey	[OIII] $_{52\mu m}$	1320.96
MCG+12-02-001	" "	" "	" "	" "	07_0209_12	2019-05-01_FLF562	G. Stacey	[NIII] $_{57\mu m}$	1351.68
NGC1365	03h 33m 36.4s	-36d 08m 26s	0.005457	S1.8	05_0111_3	2017-07-28_FLF424	G. Stacey	[OIII] $_{52\mu m}$	1843.20
IC342	03h 46m 48.5s	+68d 05m 47s	0.000103	HII	03_0135_9	2015-03-26_FLF205	K. Croxall	[OIII] $_{52\mu m}$	967.68
NGC1569	04h 30m 49.0s	+64d 50m 53s	-0.000347	Dwarf	87_0005_7	2014-04-22_FLF0162	R. Klein	[OIII] $_{52\mu m}$	14976.50
NGC1569	" "	" "	" "	" "	07_0048_2	2019-05-02_FLF563	J. Spilker	[NIII] $_{57\mu m}$	2805.76
NGC1614	04h 34m 00.0s	-08d 34m 45s	0.015938	HII	07_0209_14	2019-10-30_FLF631	G. Stacey	[OIII] $_{52\mu m}$	522.24
NGC1614	" "	" "	" "	" "	07_0209_15	2019-10-30_FLF631	G. Stacey	[NIII] $_{57\mu m}$	1136.64
NGC1808	05h 07m 42.3s	-37d 30m 46s	0.003319	HII	05_0111_3	2017-07-28_FLF424	G. Stacey	[OIII] $_{52\mu m}$	1751.04
IIZw40	05h 55m 42.7s	+03d 23m 32s	0.002632	Dwarf	06_0225_5	2018-11-06_FLF524	G. Stacey	[OIII] $_{52\mu m}$	768.00
IIZw40	" "	" "	" "	" "	06_0225_10	2018-11-06_FLF524	G. Stacey	[NIII] $_{57\mu m}$	1536.00
NGC2146	06h 18m 37.8s	+78d 21m 25s	0.002979	HII	03_0135_2	2015-03-12_FLF199	K. Croxall	[OIII] $_{52\mu m}$	368.69
NGC2146	" "	" "	" "	" "	03_0135_17	2015-03-12_FLF199	K. Croxall	[NIII] $_{57\mu m}$	307.228
NGC2366	07h 28m 55.5s	+69d 13m 05s	0.000267	Dwarf	07_0239_6	2019-05-14_FLF570	M.A. Malkan	[OIII] $_{52\mu m}$	614.40
NGC2366	" "	" "	" "	" "	07_0239_7	2019-05-14_FLF570	M.A. Malkan	[NIII] $_{57\mu m}$	614.40
He2-10	08h 36m 15.2s	-26d 24m 34s	0.002912	Dwarf	70_0508_6	2017-02-25_FLF378	A. Krabbe	[OIII] $_{52\mu m}$	1658.88
UGC5189	09h 42m 54.7s	+09d 29m 01s	0.01072	HII	07_0182_1	2019-05-09_FLF568	T. Jones	[OIII] $_{52\mu m}$	2211.84
M82	09h 55m 52.2s	+69d 40m 48s	0.000677	HII	70_0408_1	2016-02-25_FLF280	A. Krabbe	[OIII] $_{52\mu m}$	2918.40
M82	" "	" "	" "	" "	70_0608_10	2018-11-08_FLF526	A. Krabbe	[NIII] $_{57\mu m}$	4177.92
Haro3	10h 45m 22.4s	+55d 57m 38s	0.003149	Dwarf	06_0225_6	2018-11-07_FLF525	G. Stacey	[OIII] $_{52\mu m}$	1413.12
Mrk1271	10h 56m 09.1s	+06d 10m 22s	0.00338	HII	07_0182_3	2019-05-04_FLF565	T. Jones	[OIII] $_{52\mu m}$	1720.32
Arp299A	11h 28m 30.4s	+58d 34m 10s	0.0103	HII	05_0111_5	2017-02-28_FLF379	G. Stacey	[OIII] $_{52\mu m}$	2949.12
Arp299B&C	" "	" "	" "	" "	05_0111_5	2017-02-28_FLF379	G. Stacey	[OIII] $_{52\mu m}$	2949.12
Pox4	11h 51m 11.6s	-20d 36m 02s	0.01197	HII	07_0182_2	2019-05-03_FLF564	T. Jones	[OIII] $_{52\mu m}$	1259.52
Mrk193	11h 55m 28.3s	+57d 39m 52s	0.017202	HII	07_0182_4	2019-05-14_FLF570	T. Jones	[OIII] $_{52\mu m}$	3164.16
NGC4194	12h 14m 09.5s	+54d 31m 37s	0.008342	HII	07_0209_16	2019-05-09_FLF568	G. Stacey	[OIII] $_{52\mu m}$	430.08
NGC4194	" "	" "	" "	" "	07_0209_18	2019-05-09_FLF568	G. Stacey	[NIII] $_{57\mu m}$	860.16
NGC4214	12h 15m 39.3s	+36d 19m 37s	0.00097	Dwarf	06_0225_8	2019-02-28_FLF549	G. Stacey	[OIII] $_{52\mu m}$	1320.96
NGC4214	" "	" "	" "	" "	06_0225_9	2019-05-08_FLF567	G. Stacey	[NIII] $_{57\mu m}$	1413.12
NGC4536	12h 34m 27.1s	+02d 11m 17s	0.006031	HII	03_0135_6	2015-03-27_FLF206	K. Croxall	[OIII] $_{52\mu m}$	399.36
NGC4631	12h 42m 07.8s	+32d 32m 35s	0.002021	HII	07_0239_3	2019-05-10_FLF569	M.A. Malkan	[OIII] $_{52\mu m}$	215.04
NGC4631	" "	" "	" "	" "	07_0239_3	2019-05-10_FLF569	M.A. Malkan	[NIII] $_{57\mu m}$	1720.32
NGC4670	12h 45m 17.1s	+27d 07m 31s	0.003566	Dwarf	06_0222_21	2019-03-02_FLF551	T. Wiklind	[OIII] $_{52\mu m}$	491.52
M83	13h 37m 00.9s	-29d 51m 56s	0.001711	HII	07_0209_8	2019-05-04_FLF565	G. Stacey	[OIII] $_{52\mu m}$	2119.68
NGC5253	13h 39m 56.0s	-31d 38m 24s	0.001358	Dwarf	07_0239_4	2019-05-10_FLF569	M.A. Malkan	[OIII] $_{52\mu m}$	307.20
NGC5253	" "	" "	" "	" "	07_0239_5	2019-05-10_FLF569	M.A. Malkan	[NIII] $_{57\mu m}$	829.44

Table 2. Observed far-IR lines fluxes of the local galaxy sample.

Name	$F_{[\text{OIII}]52\mu\text{m}}$ [10^{-17} W/m 2]	$F_{[\text{NIII}]57\mu\text{m}}$ [10^{-17} W/m 2]	$F_{[\text{OIII}]88\mu\text{m}}$ [10^{-17} W/m 2]	$F_{[\text{NII}]122\mu\text{m}}$ [10^{-17} W/m 2]	$F_{[\text{NII}]205\mu\text{m}}$ [10^{-17} W/m 2]	Notes	Refs.
(1)	(2)	(3)	(4)	(5)	(6)	(7)	(8)
Haro11	—	28.30±0.80	172.0±3.0	3.51±0.27	2.34±0.49	*	C15
NGC253	—	599.5±178.3	625.2±53.5	802.7±28.1	175.3±11.2	*	FO16
MCG+12-02-001	305.0±30.9	52.9 ±15.3	234.0±24.0	23.20±1.12	—	‡	P21,B08,AH10
NGC1068	369.4±34.7	443.6±41.9	634.3±19.7	294.5±3.0	186.6±6.8	*	FO16
NGC1365	72.43±23.57	131.6±16.7	200.3±8.1	254.8±3.8	77.97±1.46	† #	FO16
NGC1569	1237.±245.	152.2±37.4	2800.±10.	—	—	‡ #	C15
NGC1614	219.7±71.1	46.8±6.6	193.0±12.1	—	10.62±0.39	‡ #	FO16
NGC1808	125.3±39.9	152.6±10.8	204.4±11.0	271.2±4.3	—	† #	FO16
IIZw40	202.6±46.7	58.2±16.8	359.0±4.0	<2.65	—	‡ #	P21,C15
Mrk3	114.8±46.5	19.6±3.9	58.49±2.94	10.20±1.47	—	*	FO16
NGC2146	1514.±201.	551.±59.	1577.±65.	459.3±17.4	129.6±1.9	*	B08,FO16
He2-10	336.4±54.6	98.5±10.9	338.0±5.0	—	10.42±0.49	† #	C15
IRAS08572+3915	—	2.4±0.37	5.1±0.26	0.74±0.15	—	*	DS17
UGC5101	—	10.13±6.28	14.33±3.36	13.16±1.81	6.04±0.44	*	FO16
M82	2915.±171.6	1620.±244.3	1991.±16.7	482.3±5.4	437.6±8.3	‡ #	FO16
NGC3256	—	169.8±13.8	461.1±6.9	140.6±2.0	45.27±0.97	*	FO16
Haro3	124.4±17.8	12.3±1.7	185.0±4.0	2.14±0.39	—	† #	C15
IRAS10565+2448	—	9.10±0.40	15.6±0.40	8.1±0.3	2.44±0.13	*	PS17,P16
IRAS11095-0238	4.80±1.21	1.13±0.77	—	1.05±0.43	0.49±0.16	*	FO16
Arp299 A=IC694	328.1±37.0	73.0±5.0	280.0±3.2	10.05±0.78	—	† #	C19
Arp299 B+C=NGC3690	246.8±63.7	72.0±1.3	300.0±2.6	15.96±0.38	—	† #	C19
NGC4151	37.56±9.56	21.73±2.00	48.40±2.87	7.09±0.76	6.63±0.68	*	FO16
IRAS12112+0305	—	5.6±0.9	7.4±0.5	1.4±0.4	—	*	PS17, DS17
NGC4194	282.5±14.6	65.0±22.0	206.0±14.0	<19.0	—	† #	B08
NGC4214-reg.1	130.9±11.7	19.30±4.52	319.0±6.2	4.4±2.0	17.6±0.53	‡ #	C19
NGC4631	114.6±30.7	160.1±21.5	204.7±4.3	36.74±2.56	58.97±1.47	‡ #	FO16
NGC4945	<714	177.±16.	253.±60.	347.6±9.7	—	*	FO16
NGC5033	—	12.46±2.10	25.79±2.58	57.44±1.71	—	*	FO16
IRAS13120-5453	—	16.00±3.84	30.08±5.92	33.66±3.00	10.62±0.63	*	FO16, PS17
CenA=NGC5128	<462	53.34±10.28	173.47±6.68	85.15±2.81	51.66±1.47	*	FO16
M83	205.4±18.7	166.5±10.3	216.9±6.97	321.0±4.59	92.59±3.90	† #	FO16
NGC5253	412.0±40.0	106.36±20.6	901.0±4.0	9.25±1.21	—	‡ #	C15
Mrk273	—	13.78±5.75	33.00±5.53	8.58±1.31	3.84±0.28	*	FO16
IC4329A	26.26±2.59	9.31±1.38	30.16±1.31	3.31±0.45	—	*	FO16
Mrk463E	45.95±7.92	9.61±2.11	39.68±4.13	2.31±0.27	0.51±0.20	*	FO16
Circinus	—	268.3±15.3	565.5±9.8	299.4±4.0	—	*	FO16
NGC5506	101.71±20.12	30.79±2.14	102.3±3.3	14.14±1.15	—	*	FO16
NGC6240	46.57±26.39	12.50±5.86	33.10±5.57	23.15±2.22	18.47±0.39	*	FO16
IRAS17208-0014	—	10.72±2.85	25.94±4.61	9.84±1.28	3.25±0.24	*	FO16, PS17
3C405=Cyg A	78.58±15.69	9.49±3.8	28.04±1.3	6.80±0.46	1.68±0.15	*	FO16
IRAS20551-4250	—	4.0±0.7	13.1±0.4	2.3±0.33	0.76±0.11	*	PS17,DS17,P16
NGC7130=IC5135	—	22.00±5.49	19.58±3.01	34.02±1.86	13.94±0.29	*	FO16
NGC7172	—	6.96±2.13	14.27±2.49	11.74±1.04	21.83±0.58	*	FO16
NGC7314	—	3.59±0.44	15.19±0.62	1.90±0.19	—	*	FO16
NGC7469	—	38.80±9.88	37.03±5.12	41.43±1.48	11.45±0.29	*	FO16
IRAS23128-5919	—	17.1±0.9	44.4±0.7	4.4±0.5	1.83±0.10	*	P16,DS17
NGC7582	139.8±8.1	65.58±10.23	201.9±5.3	75.45±2.04	19.59±0.73	*	FO16

Notes: From left to right, the table columns show: (1) object name; (2), (3), (4), (5), (6) line fluxes, in units of 10^{-17} W/m 2 , of the lines: $F_{[\text{OIII}]52\mu\text{m}}$; $F_{[\text{NIII}]57\mu\text{m}}$; $F_{[\text{OIII}]88\mu\text{m}}$; $F_{[\text{NII}]122\mu\text{m}}$; $F_{[\text{NII}]205\mu\text{m}}$; (7): origin of far-IR spectroscopy: All measurements of $F_{[\text{NII}]205\mu\text{m}}$ are from Herschel-SPIRE; *: all data from Herschel-PACS; †: $F_{[\text{OIII}]52\mu\text{m}}$ from SOFIA FIFI-LS; ‡: $F_{[\text{OIII}]52\mu\text{m}}$ and $F_{[\text{NIII}]57\mu\text{m}}$ from SOFIA FIFI-LS; #: SOFIA data reduced in this work; (11) reference for the line fluxes: P21: [Peng et al. \(2021\)](#), C15: [Cormier et al. \(2015\)](#), C19: [Cormier et al. \(2019\)](#), B08: ISO-LWS data from [Brauhar et al. \(2008\)](#); DS17: [Díaz-Santos et al. \(2017\)](#); FO16: Herschel-PACS data from [Fernández-Ontiveros et al. \(2016\)](#) and references therein; P16: [Pearson et al. \(2016\)](#), Pearson priv. comm. ; PS17: [Pereira-Santaella et al. \(2017\)](#).

Table 3. Observed mid-IR fluxes of the local galaxy sample.

Name	Type	$F_{[\text{SiIV}]10.5\mu\text{m}}$ [10^{-17} W/m^2]	$F_{[\text{NeII}]12.8\mu\text{m}}$ [10^{-17} W/m^2]	$F_{[\text{NeIII}]15.5\mu\text{m}}$ [10^{-17} W/m^2]	$F_{[\text{SiIII}]18.7\mu\text{m}}$ [10^{-17} W/m^2]	$F_{[\text{OIV}]25.9\mu\text{m}}$ [10^{-17} W/m^2]	$F_{[\text{SiII}]33.5\mu\text{m}}$ [10^{-17} W/m^2]	$F_{[\text{SiII}]34.8\mu\text{m}}$ [10^{-17} W/m^2]	Refs.
(1)	(2)	(3)	(4)	(5)	(6)	(7)	(8)	(9)	(10)
Haro11	Dwarf	49.4±1.1	32.7±0.9	112.±5.	53.1±2.9	4.390±0.784	81.7±7.0	55.8±4.5	C15
NGC253	HII	<10.50	2832.30±64.20	204.60±9.60	666.40±14.90	154.70±26.90	1538.00±30.10	2412.00±48.00	FO16
MCG+12-02-001	LIRG	3.14±0.81	201.10±2.12	36.99±0.67	73.46±1.55	<6.36	167.60±5.15	181.70±9.64	I13
NGC1068	S1h	536.10±12.80	458.10±13.80	1371.00±10.20	240.60±14.00	2030.00±27.30	374.10±23.20	604.40±17.10	FO16
NGC1365	S1	18.60±0.78	143.00±3.79	61.30±0.51	51.20±0.57	365.00±26.90	720.00±102.00	1303.00±81.00	FO16
IC342	HII	4.76±0.66	615.46±10.52	37.20±0.90	320.03±5.96	<7.70	672.46±7.28	985.73±10.29	FO16
NGC1569	Dwarf	247.±3.	30.5±2.7	324.±13.	131.±5.	31.9±1.5	185.±6.	22.95±1.19	C15
NGC1614	HII	6.89±0.54	249.00±7.00	63.32±1.59	83.03±2.64	8.68±0.85	101.06±2.11	148.60±4.11	FO16
NGC1808	HII	1.47±0.00	177.36±16.36	17.26±0.68	46.20±2.29	<9.54	205.83±20.27	354.26±15.15	FO16
IIZw40	Dwarf	200.±10.	7.35±0.79	141.±9.	52.1±2.2	7.94±1.15	78.2±2.1	36.8±3.5	C15
Mrk3	S1h	59.30±0.62	98.00±1.02	175.00±1.10	53.60±4.49	196.00±2.40	52.40±6.89	84.60±3.28	FO16
NGC2146	LIRG	6.30±0.44	625.00±15.35	91.16±0.95	190.12±4.15	19.33±4.48	848.02±36.93	1209.35±21.70	FO16
He2-10	Dwarf	32.7±1.3	380.0±13.0	156.0±5.0	267.0±19.0	7.915±2.514	317.0±10.0	193.0±4.0	C15
IRAS08572+3915	ULIRG	<0.5	8.36±0.69	2.46±0.50	1.84±0.51	<2.1	<7.7	—	A07,V09
UGC5101	ULIRG	1.32±0.32	37.43±0.45	14.05±0.18	8.46±0.20	7.34±0.83	13.91±1.39	27.47±3.31	I13
NGC2976	HII	—	6.3±0.6	2.2±0.2	5.1±0.3	0.3±0.1	7.5±0.2	6.9±0.4	D06
M82	HII	5.65±0.74	506.22±45.04	80.98±1.99	172.06±5.80	45.67±6.61	1812.90±36.79	2166.00±25.52	FO16
NGC3256	HII	5.25±0.57	514.19±9.34	64.42±0.86	171.83±2.07	12.23±3.02	484.64±13.79	623.37±9.81	?
Haro3	Dwarf	40.8±1.7	35.2±1.3	98.4±7.4	50.3±3.9	1.79±0.5	85.1±2.4	39.9±2.4	C15
IRAS10565+2448	ULIRG	<1.25	61.75±0.81	7.67±0.42	12.35±1.01	<2.40	19.31±1.53	39.88±5.59	I13
IRAS11095-0238	ULIRG	<1.20	6.08±0.61	1.89±0.19	1.22±0.24	<0.90	—	—	FO16
Arp299 B=NGC3690.W ^a	LIRG	5.52±1.11	103.80±2.71	54.42±0.98	47.71±1.79	28.90±3.78	204.00±11.63	228.80±6.27	I10
Arp299 A=NGC3690.E ^b	LIRG	5.06±0.79	237.40±2.65	57.05±0.98	61.61±2.04	16.07±14.29	271.90±22.72	267.00±18.23	I10
NGC4151	S1	84.80±5.51	134.00±5.84	214.50±11.20	71.00±5.05	244.00±9.07	68.50±5.90	135.00±3.77	FO16
IRAS12112+0305	ULIRG	0.47±0.11	14.0±0.14	3.70±0.04	5.40±0.16	<1.1	10.0±0.5	—	I10, V09
NGC4194	LIRG	9.15±0.53	175.70±1.40	56.20±0.60	71.26±0.91	25.10±1.85	157.40±8.53	185.50±3.99	I13
NGC4214-reg.1	Dwarf	56.80±2.10	89.80±2.20	187.00±1.40	117.80±2.00	<9.78	187.10±2.70	—	C15
NGC4536	HII	0.95±0.20	35.46±0.39	6.11±0.06	16.34±0.91	1.72±0.25	100.48±4.53	114.02±1.53	FO16
NGC4631	HII	1.39±0.42	45.92±0.71	10.15±0.13	39.69±2.12	<1.47	85.16±0.76	114.74±1.89	FO16
NGC4945	S	—	698.40±60.40	68.10±2.27	—	28.35±1.39	359.60±20.40	732.80±7.84	FO16
NGC 5033	S2	2.83±0.20	13.26±0.18	5.08±0.15	14.88±0.50	5.08±0.51	17.38±0.85	45.35±1.52	FO16
IRAS13120-5453	ULIRG	0.50±0.10	150.00±15.00	18.46±1.85	19.18±1.92	6.42±1.28	60.64±6.06	107.10±10.70	FO16
CenA=NGC5128	S2	14.01±3.55	189.10±17.50	148.00±6.08	48.50±2.75	129.00±7.05	148.80±10.20	285.40±8.86	FO16
M83-nucleus	HII	3.31±0.23	503.33±19.88	29.30±0.77	227.66±16.51	5.75±1.08	263.50±9.21	391.40±8.55	FO16
NGC5253	Dwarf	541.±211.	121.1±59.6	656.±39.	261.±124.	9.80±2.41	626.±398.	329.±231.	FO16
Mrk273	S2	9.58±0.96	41.90±4.19	33.57±3.36	13.35±1.33	56.36±5.64	42.56±4.26	14.66±2.90	FO16
IC4329A	S1	29.10±1.32	27.60±0.73	57.00±0.97	15.00±1.44	117.00±1.42	16.00±2.19	32.50±3.06	FO16
Mrk463E	S1h	29.86±2.99	9.25±0.92	40.78±4.08	15.85±1.59	69.17±6.92	15.50±1.55	29.79±2.98	FO16
Circinus	S1h	123.20±53.20	393.00±67.50	385.40±29.90	194.50±26.20	897.50±48.90	594.40±89.20	729.90±51.70	FO16
NGC5506	S1h	73.50±1.56	85.10±1.43	153.70±1.10	58.60±7.79	226.20±4.00	91.70±24.40	137.00±6.92	FO16
NGC6240	LIN	2.68±0.27	171.00±17.10	60.60±6.10	17.10±1.71	26.75±2.67	38.11±3.81	265.90±26.60	FO16
IRAS17208-0014	ULIRG	<0.4	38.0±0.38	7.90±0.16	7.30±0.22	<3.2	<13.0	60.0±1.2	V09
3C405	S2	16.20±0.70	21.70±0.70	47.90±0.50	24.20±0.60	78.50±0.70	29.00±1.00	—	FO16
IRAS20551-4250	ULIRG	<1.28	13.49±0.95	2.73±0.61	6.74±0.43	<4.18	9.98±4.49	23.30±8.81	I13
NGC7130=IC5135	S2	5.27±0.84	79.30±0.93	29.40±0.77	19.60±0.33	19.70±0.84	48.20±2.59	93.90±4.90	FO16
NGC7172	S2	5.87±0.61	33.00±1.01	17.10±0.68	11.90±1.00	45.40±0.48	26.90±1.51	59.30±2.42	FO16
NGC7314	S1h	15.90±0.53	8.08±0.39	23.20±0.53	9.97±0.71	67.00±0.41	15.00±1.71	14.20±1.76	FO16
NGC7469	S1	9.00±0.79	191.00±2.70	35.80±0.75	75.40±4.52	34.00±3.80	63.60±9.21	194.00±19.10	FO16
NGC7582	S1h	21.30±1.43	322.00±6.41	105.00±2.05	87.30±1.99	262.00±5.54	244.00±7.85	—	FO16
IRAS23128-5919	ULIRG	4.80±0.28	32.12±0.45	21.72±0.46	24.64±1.70	14.97±2.47	19.35±2.28	34.03±7.47	I13

Notes: From left to right, the table columns show: (1) object name; (2) Galaxy type (dwarf Galaxy, Seyfert, Starburst (HII), and ULIRG); (3), (4), (5), (6), (7), (8), (9) fluxes of the given mid-IR fine structure lines, in units of 10^{-17} W/m^2 , from the following references: (10): FO16: Fernández-Ontiveros et al. (2016) and references therein; I13: Inami et al. (2013); C15: Cormier et al. (2015); D06: Dale et al. (2006); fluxes averaged over $\sim 23'' \times 15''$ and listed in units of $10^{-9} \text{ Wm}^{-2} \text{sr}^{-1}$; A07: Armus et al. (2007); V09: Veilleux et al. (2009); I10: Imanishi et al. (2010).

^a 11h 28m 31.0s 58d 33m 43

^b 11h 28m 33.7s 58d 33m 49

Table 4. Observed properties of other galaxies observed by SOFIA in the [OIII]52 μ m line.

Name	RA	dec	z	Type	12+log(O/H)	$F_{[\text{OIII}]52\mu\text{m}}$ [10^{-17} W/m 2]	$F_{[\text{OIII}]88\mu\text{m}}$ [10^{-17} W/m 2]	Notes	refs.
(1)	(2)	(3)	(4)	(5)	(6)	(7)	(8)	(9)	(10)
IC342	03h 46m 48.5s	+68d 05m 47s	0.000103	HII	8.71 \pm 0.01	98.21 \pm 18.99	171.14 \pm 7.92	† #	
NGC2366	07h 28m 55.6s	+69d 13m 05s	0.000267	Dwarf	7.64 \pm 0.03	155.84 \pm 39.85	226.00 \pm 1.00	† #	M13, C15
UGC5189	09h 42m 54.7s	+09d 29m 01s	0.010720	HII	8.29 \pm 0.07	30.75 \pm 4.45	—	† #	PT07
NGC3077	10h 03m 19.1s	+68d 44m 02s	0.000047	HII	8.60 \pm 0.01	745.65 \pm 112.98	—	† #	C04
Mrk1271	10h 56m 09.1s	+06d 10m 22s	0.003380	HII	7.99 \pm 0.04	< 12 ^a	—	† #	I98
Pox4	11h 51m 11.6s	-20d 36m 02s	0.011970	HII	7.97 \pm 0.06	46.85 \pm 6.44	—	† #	K96
Mrk193	11h 55m 28.3s	+57d 39m 52s	0.017202	HII	7.79 \pm 0.27	< 12 ^b	—	† #	I94
NGC4536	12h 34m 27.1s	+02d 11m 17s	0.006031	HII	8.83 \pm 0.01	136.90 \pm 29.26	166.61 \pm 7.63	† #	
NGC4670	12h 45m 17.1s	+27d 07m 31s	0.003566	Dwarf	8.47 \pm 0.02	38.17 \pm 4.2	—	† #	

Notes: From left to right, the table columns show: (1) object name; (2,3) 2MASS coordinates; (4) NED redshift (z); (5) Galaxy type: dwarf Galaxy, Seyfert, Starburst (HII), Luminous IR Galaxy (LIRG) or Ultra Luminous OR Galaxy (ULIRG); (6) optical metallicity; (7), (8) line fluxes, in units of 10^{-17} W/m 2 , of the lines: $F_{[\text{NIII}]57\mu\text{m}}$ $F_{[\text{OIII}]88\mu\text{m}}$; (9): origin of far-IR spectroscopy: †: $F_{[\text{OIII}]52\mu\text{m}}$ from SOFIA FIFI-LS; #: SOFIA data reduced in this work; the $F_{[\text{OIII}]88\mu\text{m}}$ line fluxes are from Herschel-PACS (Fernández-Ontiveros et al. 2016, and references therein); (10) reference for the metallicity data: M13: Madden et al. (2013); C15: Cormier et al. (2015); PT07: Pilyugin & Thuan (2007); C04: Calzetti et al. (2004); I98: Izotov & Thuan (1998); K96: Kobulnicky & Skillman (1996); I94: Izotov et al. (1994).

^a 3σ upper limit, very noisy line profile

^b 3σ upper limit, line profile not consistent with the expected line width of ~ 300 kms $^{-1}$

Table 5. Observed properties of the local galaxy sample: coordinates, types & metallicities

Name	RA	dec	z	Type	12+log(O/H)	log(N/O)	Refs.	12+log(O/H) _{IR}	log(N/O) _{IR}
(1)	(2)	(3)	(4)	(5)	(6)	(7)	(8)	(9)	(10)
Haro11	00h 36m 52.5s	-33d 33m 17s	0.020598	Dwarf	8.23±0.03	-0.92	M13,C19	8.51±0.07	-1.2±0.2
NGC253	00h 47m 33.1s	-25d 17m 19s	0.000811	HII	8.61±0.01	-0.43±0.04	TW	8.7±0.2	-0.4±0.2
MCG+12-02-001	00h 54m 03.6s	+73d 05m 12s	0.015698	LIRG	8.7	...	AH10	8.7±0.1	-1.0±0.1
NGC1068	02h 42m 40.7s	-00d 00m 48s	0.003793	S1h	8.60±0.06	-0.02±0.02	TW	...	-0.35±0.05
NGC1365	03h 33m 36.4s	-36d 08m 26s	0.005457	S1	8.88±0.02	...	TW	...	-0.3±0.05
NGC1569	04h 30m 49.0s	+64d 50m 53s	-0.000347	Dwarf	8.19±0.03	-1.39	M13,C19	7.7±0.2	-1.6±0.1
NGC1614	04h 34m 00.0s	-08d 34m 45s	0.015938	HII	8.60±0.01	-0.56±0.03	TW	8.69±0.08	-1.0±0.1
NGC1808	05h 07m 42.3s	-37d 30m 46s	0.003319	HII	8.71±0.01	-0.4±0.1	TW	8.5±0.3	-0.8±0.3
IIZw40	05h 55m 42.6s	+03d 23m 32s	0.002632	Dwarf	8.09±0.02	-1.44	M13,C19	7.7±0.2	...
Mrk3	06h 15m 36.4s	+71d 02m 15s	0.013509	S1h	8.69±0.07	-0.55±0.03	TW	...	-0.9±0.1
NGC2146	06h 18m 37.8s	+78d 21m 25s	0.002979	LIRG	8.71±0.02	-0.77±0.03	TW	8.7±0.1	-0.9±0.1
NGC2366	07h 28m 55.6s	+69d 13m 05s	0.000267	Dwarf	7.64±0.03	...	M13
He2-10	08h 36m 15.2s	-26d 24m 34s	0.002912	Dwarf	8.65±0.01	-0.75±0.01	TW	8.64±0.08	-1.0±0.1
IRAS08572+3915	09h 00m 25.4s	+39d 03m 54s	0.05835	ULIRG	8.62±0.02	-0.96±0.05	TW	8.5±0.2	-0.7±0.2
UGC5101	09h 35m 51.6s	+61d 21m 11s	0.01615	ULIRG	8.78±0.02	-0.7±0.1	TW	8.6±0.1	-0.6±0.4
M82	09h 55m 52.7s	+69d 40m 46s	0.00068	HII	8.70±0.01	-0.46±0.03	TW	8.6±0.1	-0.8±0.2
NGC3256	10h 27m 51.3s	-43d 54m 13s	0.00935	HII	8.39±0.07	-0.39±0.02	TW	8.70±0.09	-0.80±0.09
Haro3	10h 45m 22.4s	+55d 57m 38s	0.003149	Dwarf	8.37±0.02	-1.35	M13,C19	8.30±0.07	-1.4±0.1
IRAS10565+2448	10h 59m 18.2s	+24d 32m 34s	0.04310	ULIRG	8.77±0.02	-0.50±0.01	TW	8.6±0.1	-0.6±0.1
IRAS11095-0238	11h 12m 03.4s	-02d 54m 23s	0.106634	ULIRG	8.53±0.02	-0.77±0.09	TW	8.7±0.1	-0.9±0.3
Arp299 A=IC694	11h 28m 33.7s	58d 33m 49s	0.01041	LIRG	8.56±0.02	-0.74±0.02	TW	8.5±0.1	-1.0±0.1
Arp299 B+C=NGC3690	11h 28m 31.0s	58d 33m 43s	0.01022	LIRG	8.79±0.02	-0.50±0.01	TW	8.6±0.1	-1.0±0.1
NGC4151	12h 10m 32.6s	+39d 24m 21s	0.003319	S1	8.5±0.1	-0.71±0.07	TW	...	-0.59±0.06
IRAS12112+0305	12h 13m 46.0s	+02d 48m 38s	0.073317	ULIRG	8.66±0.02	-0.75±0.01	TW	8.4±0.2	-0.5±0.2
NGC4194	12h 14m 09.5s	+54d 31m 37s	0.008342	LIRG	8.52±0.01	-0.63±0.03	TW	8.5±0.2	-0.9±0.1
NGC4214-reg.1	12h 15m 39.3s	+36d 19m 37s	0.00097	Dwarf	8.20±0.03	...	M13	8.6±0.1	-1.4±0.1
NGC4631	12h 42m 07.8s	+32d 32m 35s	0.002021	HII	8.52±0.01	-1.11±0.03	TW	8.69±0.07	...
NGC4945	13h 05m 27.5s	-49d 28m 06s	0.00188	S2	8.5±0.4	-0.6±0.2
NGC5033	13h 13m 27.5s	+36d 35m 38s	0.00292	S2	8.85±0.07	-0.25±0.01	TW	...	-0.73±0.07
IRAS13120-5453	13h 15m 06.4s	-55d 09m 23s	0.03076	ULIRG	8.7±0.1	-0.7±0.2
CenA=NGC5128	13h 25m 27.6s	-43d 01m 09s	0.00183	S2	8.85±0.02	-0.91±0.04	TW	...	-0.92±0.08
M83	13h 37m 00.9s	-29d 51m 56s	0.001711	HII	8.6±0.2	-0.34±0.02	TW	8.7±0.1	-0.7±0.2
NGC5253	13h 39m 56.0s	-31d 38m 24s	0.001358	Dwarf	8.16±0.03	-1.45	M13,C19	8.2±0.1	-1.2±0.1
Mrk273	13h 44m 42.1s	+55d 53m 13s	0.03778	S2	8.85±0.06	-1.06±0.07	TW	...	-0.8±0.2
IC4329A	13h 49m 19.3s	-30d 18m 34s	0.016054	S1	8.4±0.2	-1.0±0.4	TW	...	-0.77±0.07
Mrk463E	13h 56m 02.9s	+18d 22m 18s	0.05035	S1h	8.5±0.2	-1.0±0.4	TW	...	-0.9±0.1
Circinus	14h 13m 09.9s	-65d 20m 21s	0.00145	S1h	8.8±0.1	-0.4±0.1	TW	...	-0.74±0.02
NGC5506	14h 13m 14.9s	-03d 12m 28s	0.006181	S1h	8.76±0.07	-1.1±0.3	TW	...	-0.81±0.05
NGC6240	16h 52m 58.9s	+02d 24m 04s	0.02448	LIN	8.85±0.01	-1.1±0.1	TW	...	-0.9±0.2
IRAS17208-0014	17h 23m 21.9s	-00d 17m 01s	0.042810	ULIRG	8.69±0.01	-0.61±0.03	TW	8.7±0.1	-0.8±0.2
3C405=Cyg A	19h 59m 28.3s	+40d 44m 02s	0.056075	S2	8.78±0.04	-0.50±0.06	TW	...	-1.0±0.2
IRAS20551-4250	20h 58m 26.8s	-42d 39m 00s	0.042996	ULIRG	8.50±0.01	-0.83±0.05	TW	8.70±0.09	-0.9±0.2
NGC7130=IC5135	21h 48m 19.5s	-34d 57m 05s	0.01615	S2	8.60±0.09	-0.6±0.3	TW	...	-0.4±0.1
NGC7172	22h 02m 01.9s	-31d 52m 11s	0.00868	S2	8.8±0.2	...	TW	...	-0.7±0.1
NGC7314	22h 35m 46.2s	-26d 03m 02s	0.004763	S1h	8.88±0.02	-0.2±0.2	TW	...	-1.03±0.05
NGC7469	23h 03m 15.6s	+08d 52m 26s	0.01632	S1	8.4±0.1	-0.38±0.03	TW	...	-0.4±0.1
IRAS23128-5919	23h 15m 46.8s	-59d 03m 16s	0.04460	ULIRG	8.40±0.07	-0.75±0.01	TW	8.48±0.07	-0.8±0.1
NGC7582	23h 18m 23.7s	-42d 22m 14s	0.005254	S1h	8.5±0.1	-0.47±0.02	TW	...	-0.71±0.06

Notes: From left to right, the table columns show: (1) object name; (2,3) 2MASS coordinates; (4) NED redshift (z); (5) Galaxy type: dwarf, Seyfert, starburst (HII), Luminous IR Galaxy (LIRG) or Ultra Luminous IR Galaxy (ULIRG); (6,7) Oxygen abundance and nitrogen-to-oxygen relative abundance determined from optical nebular lines; (8) References for the optical abundances: AH10: [Alonso-Herrero et al. 2010](#), C19: [Cormier et al. 2019](#), M13: [Madden et al. 2013](#), TW: this work; (9) Oxygen abundance and nitrogen-to-oxygen relative abundance determined from IR nebular lines using HCM-IR ([Fernández-Ontiveros et al. 2021](#)).

APPENDIX

A. APPENDIX INFORMATION

We present below our reductions for various galaxies included in Table 2.

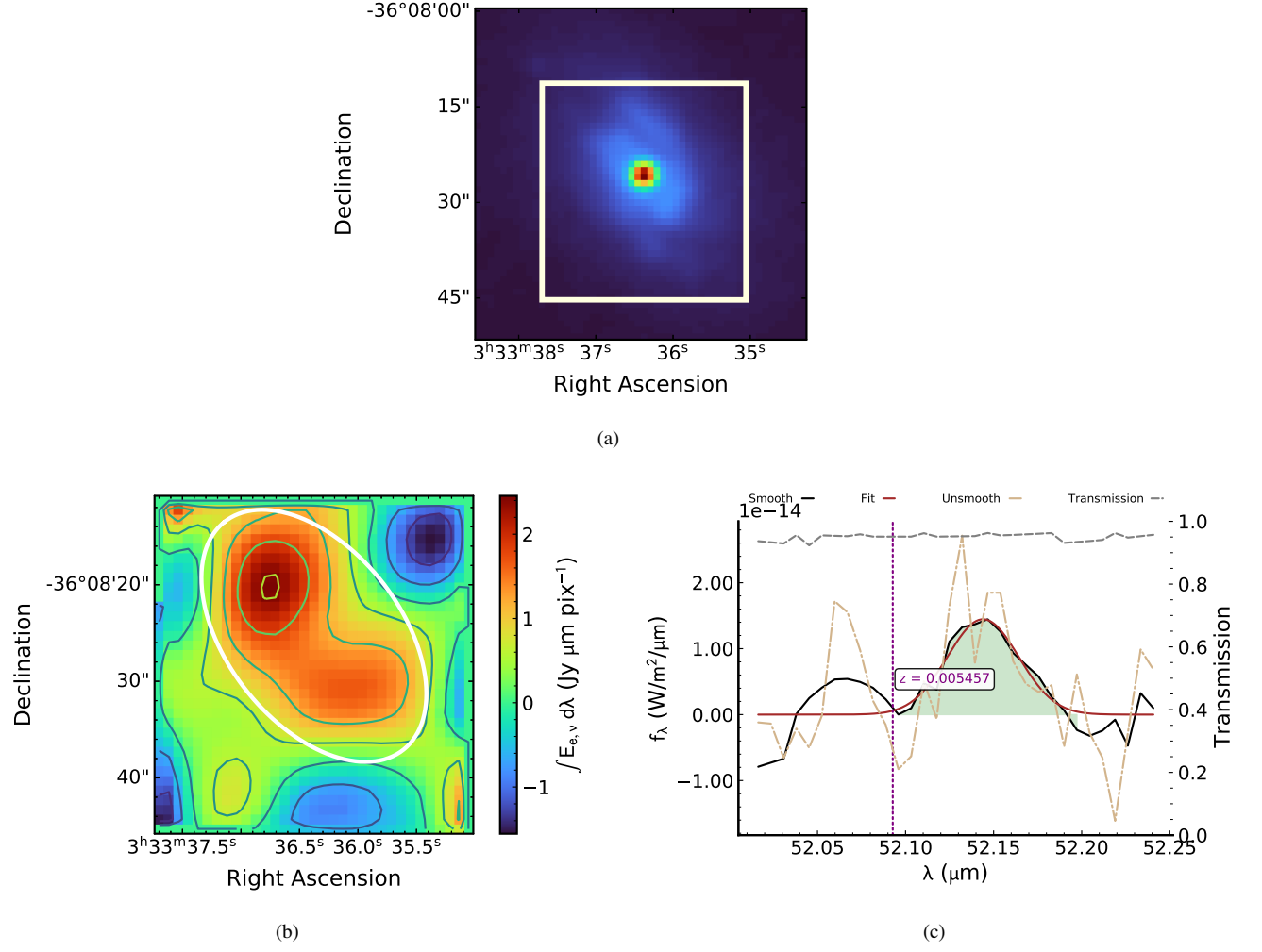


Figure 23. The 2MASS image (Figure 23(a)) as well as 2-D linemap, and 1-D spectrum for [OIII]52 μm (Figures 23(b) and 23(c), respectively) in NGC1365. In this case the optical center, located at the active galactic nucleus lies in between the two peaks of the far-IR emission which are on either side of the galactic disk.

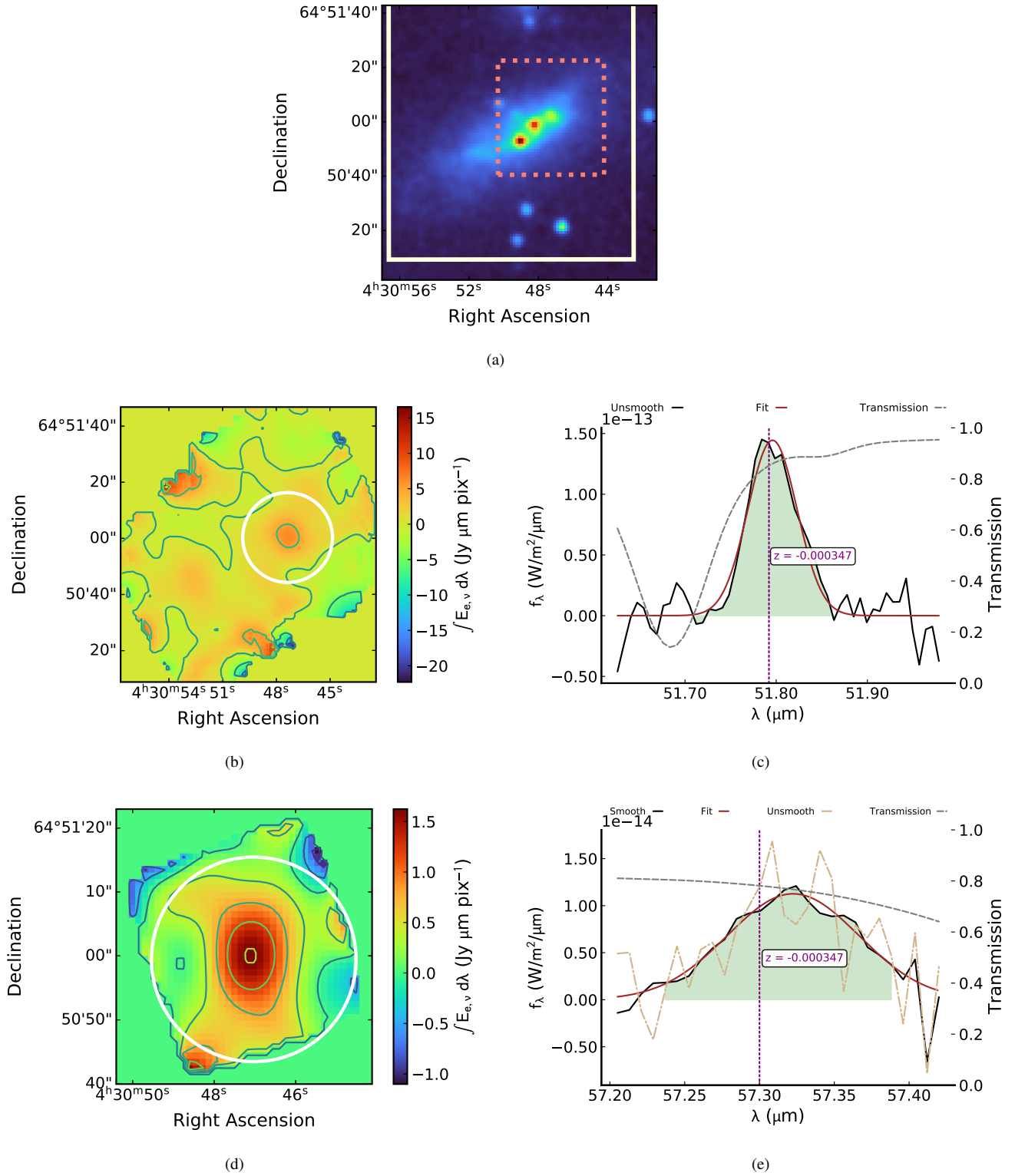


Figure 24. The 2MASS image (Figure 24(a)), 2-D linemaps and 1-D spectra for [OIII]52 μm (Figures 24(b) and 24(c), respectively) and [NIII]57 μm (Figures 24(d) and 24(e), respectively) in NGC1569. The profiles for both lines have not been corrected for atmospheric transmission, and the large apertures are meant to be comparable to the Herschel apertures used for calculating [OIII]88 μm . The [OIII]52 μm linemap is a scan of a larger area, but apertures for both [OIII]52 μm and [NIII]57 μm have the same size, and are centered around the same coordinate.

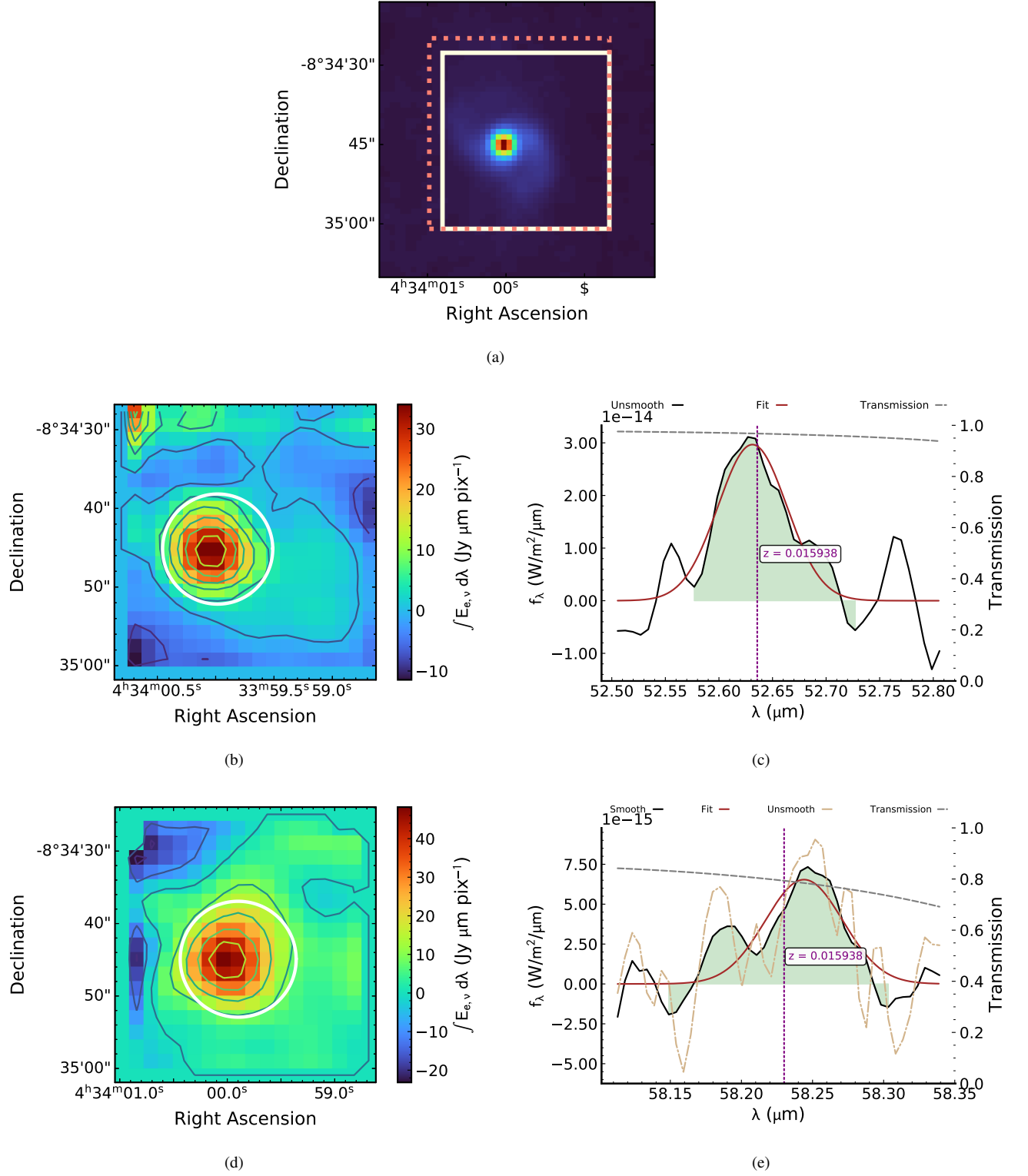


Figure 25. The 2MASS image (Figure 25(a)), 2-D linemaps and 1-D spectra for [OIII]52 μm (Figures 25(b) and 25(c), respectively) and [NIII]57 μm (Figures 25(d) and 25(e), respectively) in NGC1614.

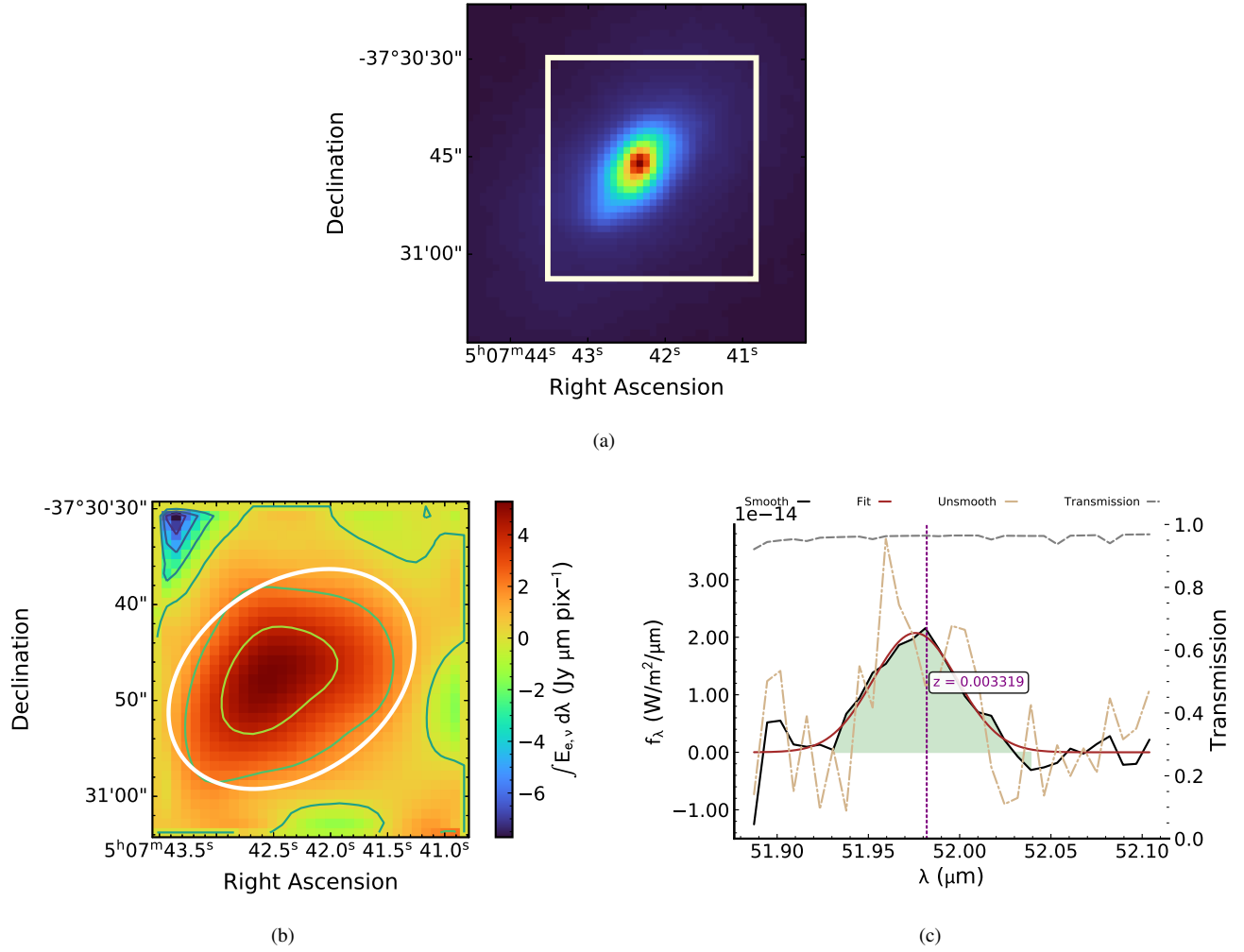


Figure 26. The 2MASS image (Figure 26(a)) as well as 2-D linemap and 1-D spectrum for [OIII]52μm (Figures 26(b) and 26(c), respectively) in NGC1808.

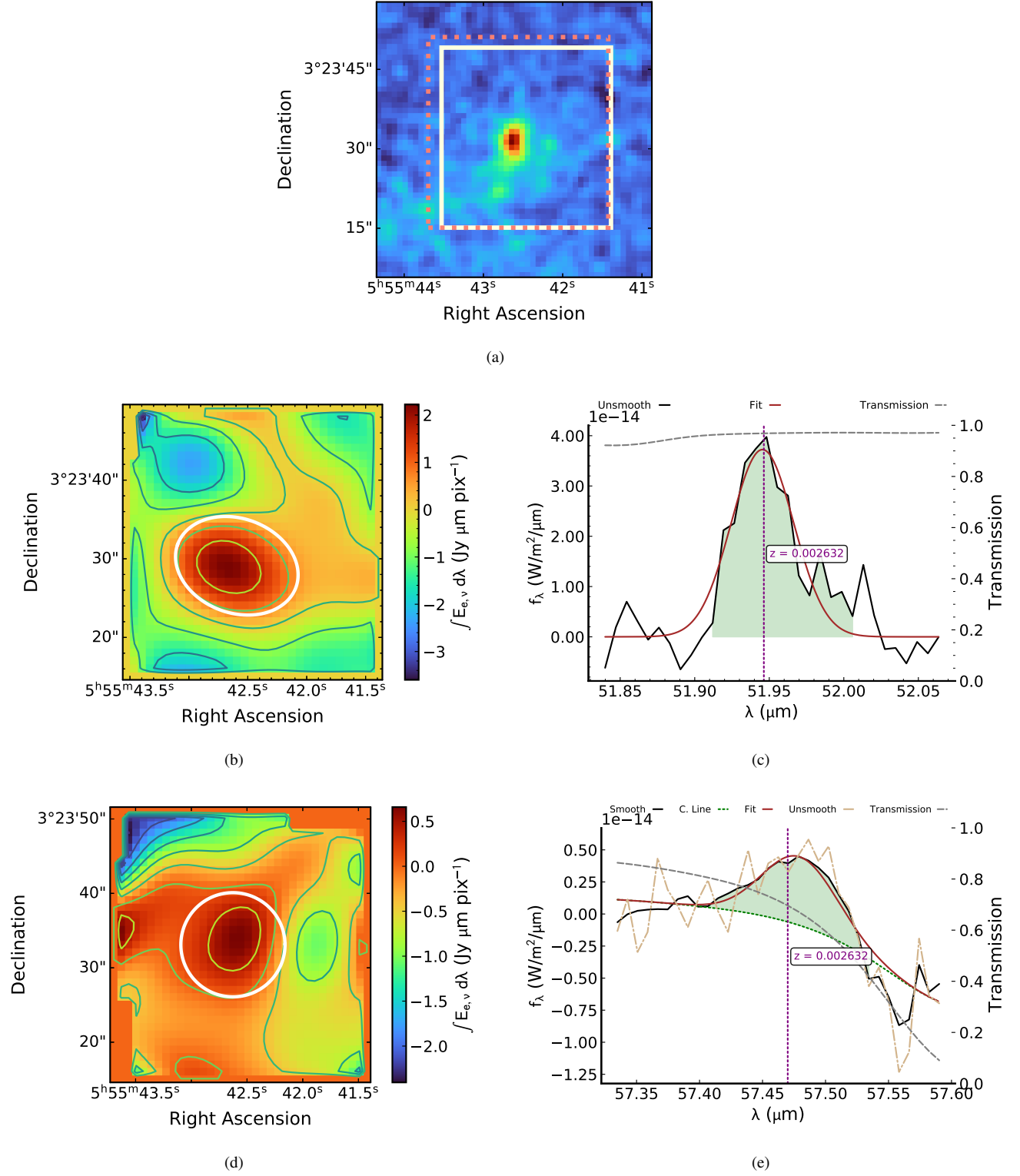


Figure 27. The 2MASS image (Figure 27(a)) 2-D linemaps and 1-D spectra for [OIII]52μm (Figures 27(b) and 27(c), respectively) and [NIII]57μm (Figures 27(d) and 27(e), respectively) in II Zw 40. The [NIII]57μm profile has not been corrected for atmospheric transmission. Further, to account for the poor transmission towards the red wavelengths, the continuum has been chosen as the best fit of a straight line times the transmission line shape (green dotted line in Figure 27(d)).

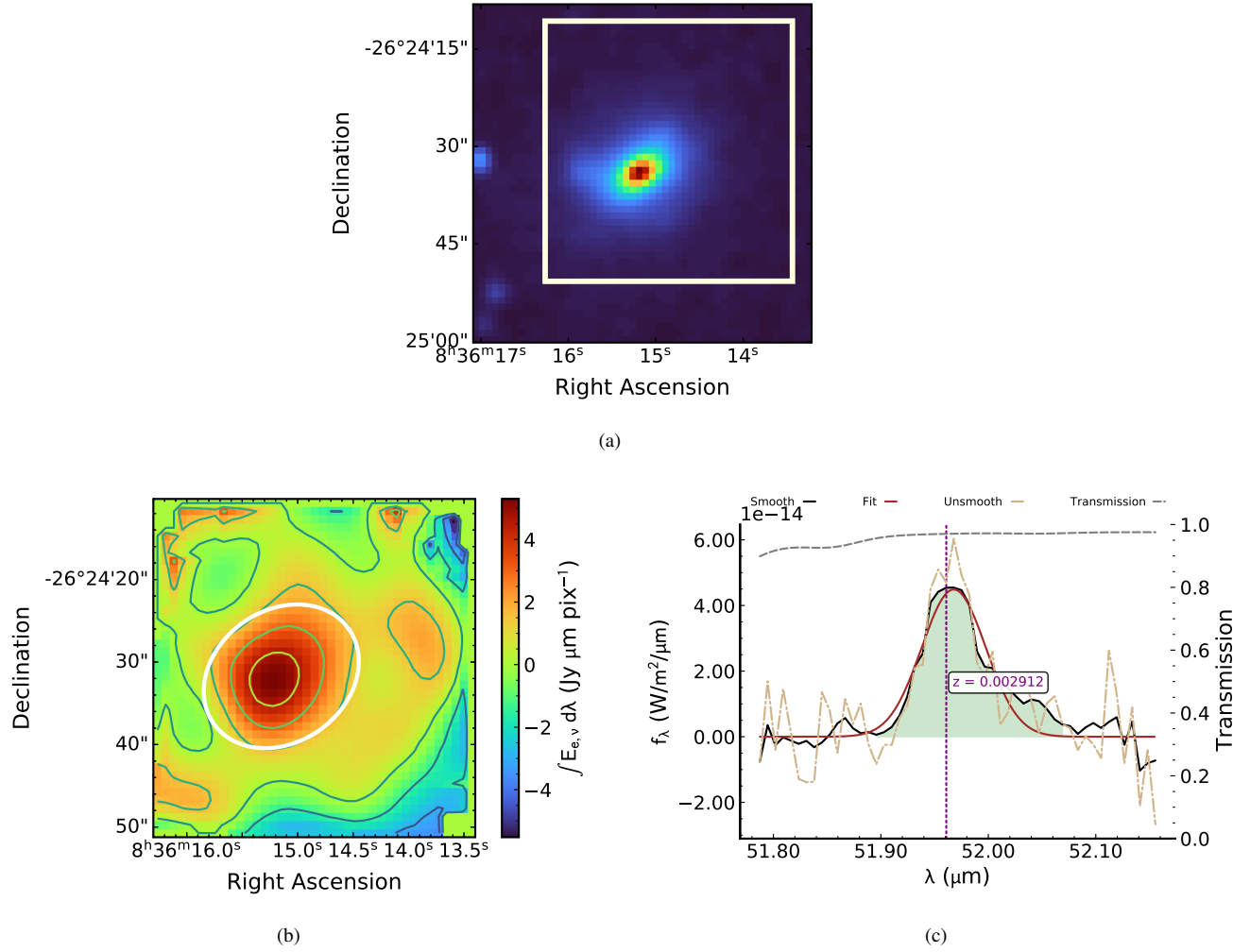


Figure 28. The 2MASS image (Figure 28(a)) as well as 2-D linemap and 1-D spectrum for $[OIII]52\mu m$ (Figures 28(b) and 28(c), respectively) in He2-10.

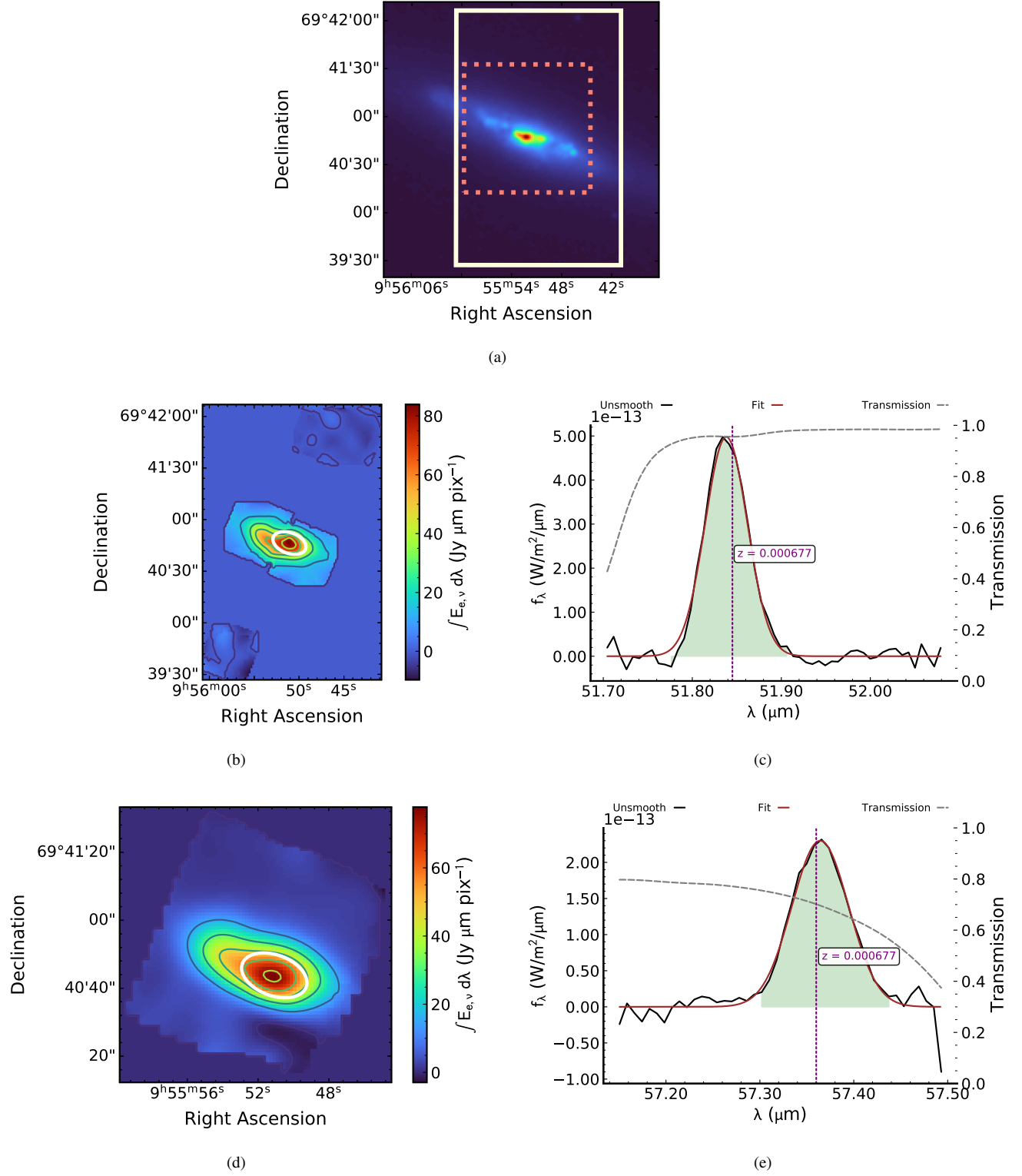


Figure 29. The 2MASS image (Figure 29(a)), 2-D linemaps and 1-D spectra for [OIII]52 μm (Figures 29(b) and 29(c), respectively) and [NIII]57 μm (Figures 29(d) and 29(e), respectively) in M82.

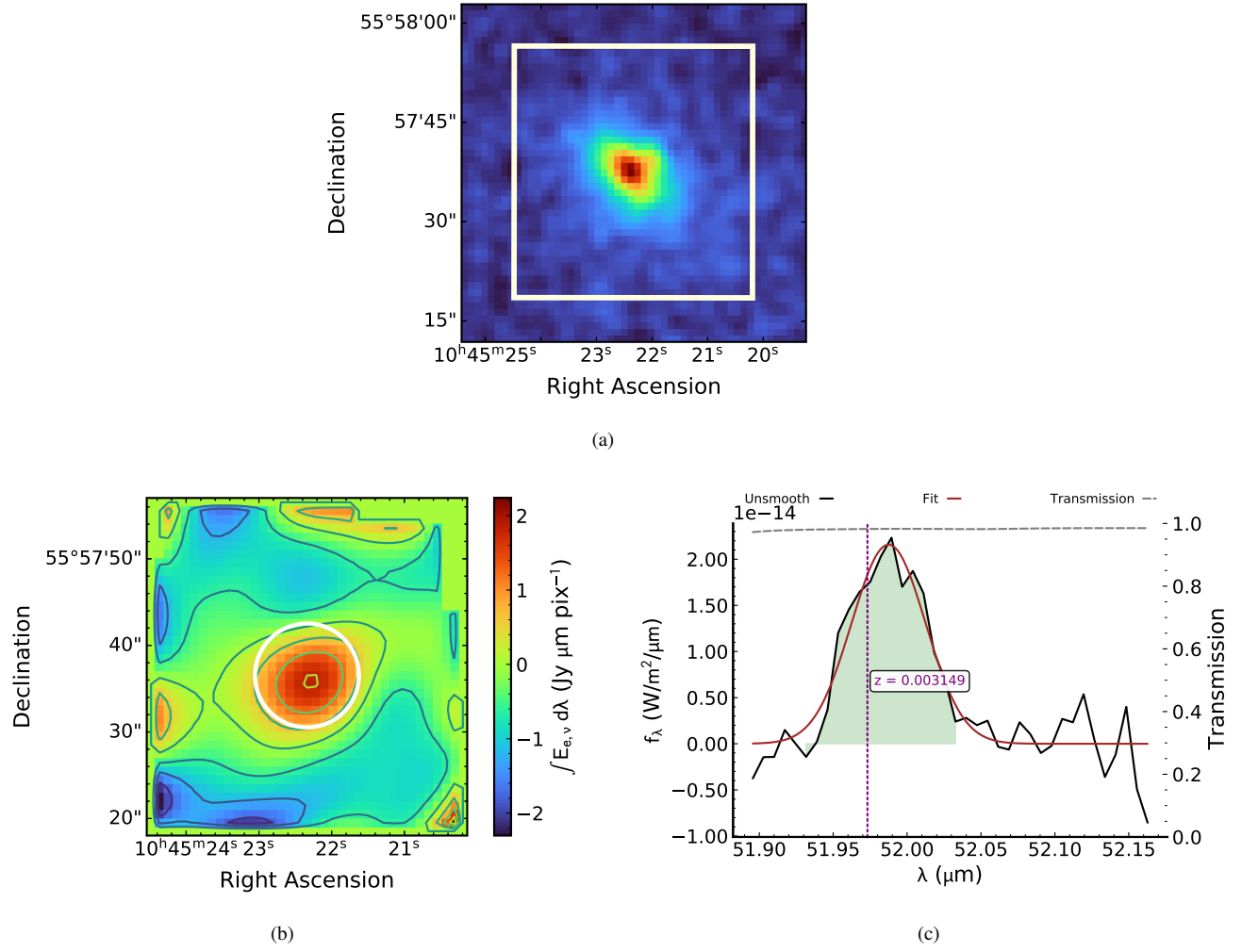


Figure 30. The 2MASS image (Figure 30(a)) 2-D linemap and 1-D spectrum for $[OIII]52\mu\text{m}$ (Figures 30(b) and 30(c), respectively) in Haro3.

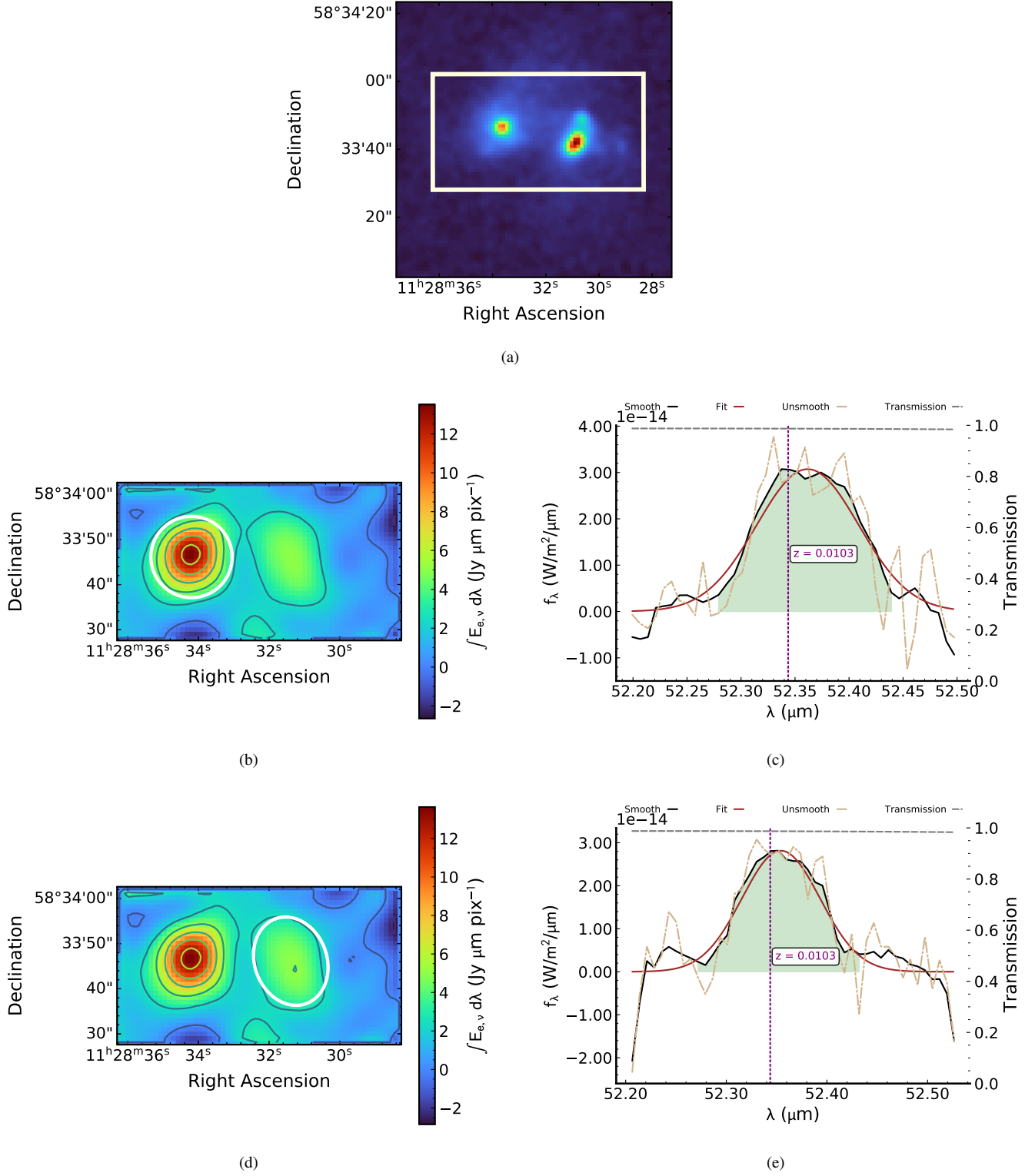


Figure 31. The 2MASS image of Arp299 (Figure 31(a)), the [OIII]52μm 2-D linemap and 1-D spectrum of Arp299A (Figures 31(b) and 31(c), respectively), [OIII]52μm 2-D linemap and 1-D spectrum of Arp299B&C (Figures 31(d) and 31(e)), respectively

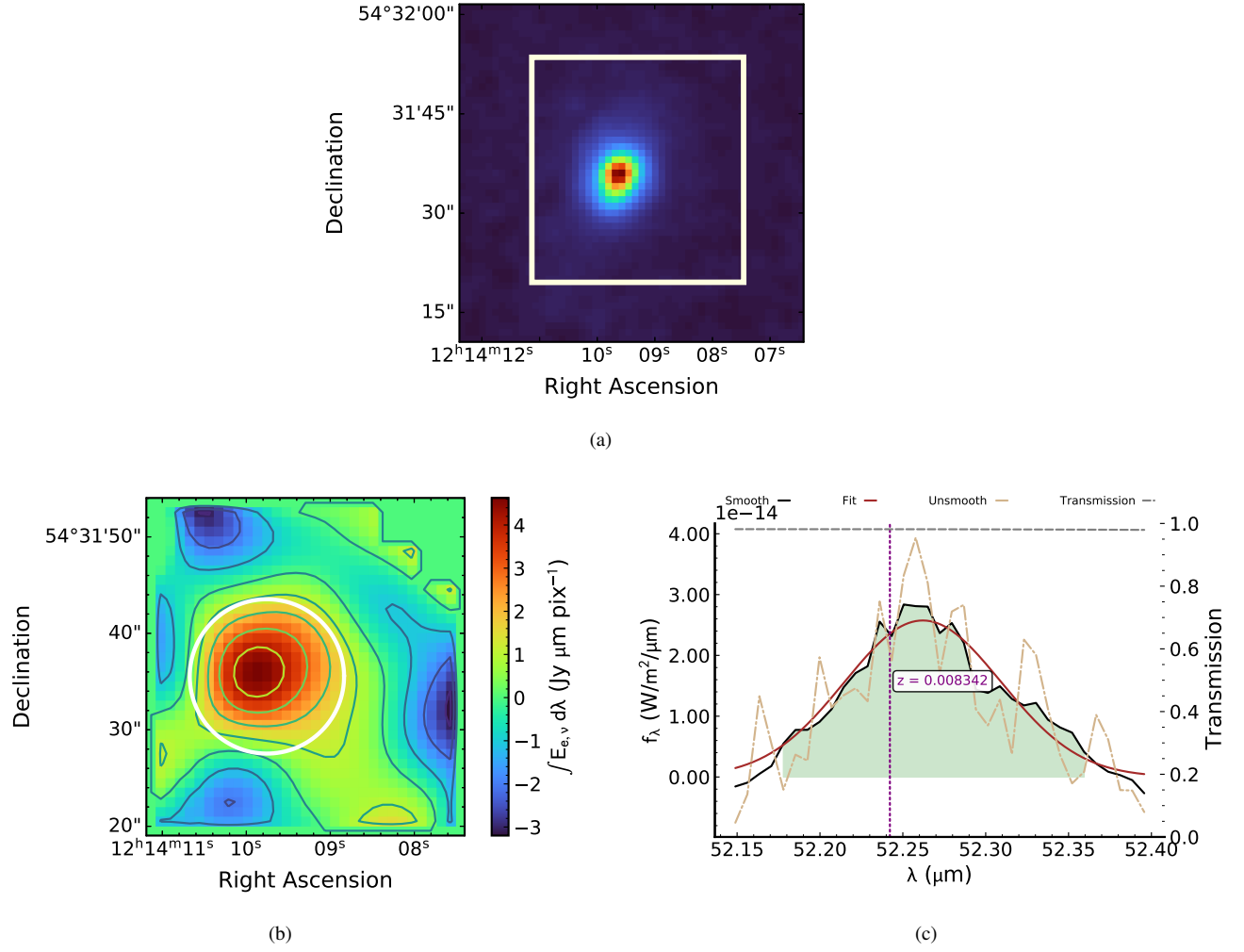


Figure 32. The 2MASS image (Figure 32(a)), 2-D linemap and 1-D spectrum for $[OIII]52\mu m$ (Figures 32(b) and 32(c), respectively) in NGC4194.

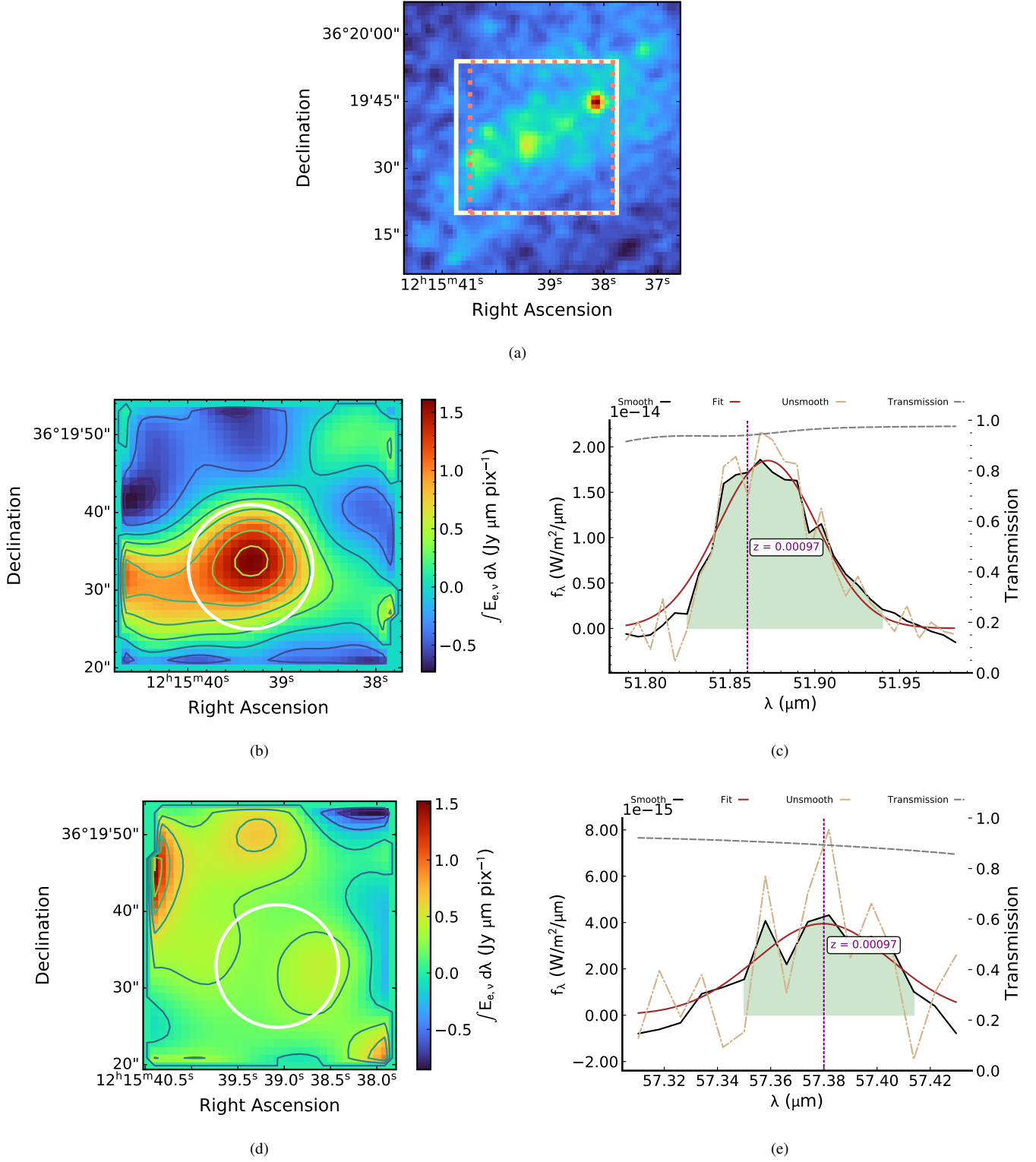


Figure 33. The 2MASS image (Figure 33(a)), 2-D linemaps and 1-D spectra for [OIII]52 μ m (Figures 33(b) and 33(c), respectively) and [NIII]57 μ m (Figures 33(d) and 33(e), respectively) in NGC4214. While the [NIII]57 μ m map does not show a clear peak, we centered the circular extraction aperture around the same location as for the [OIII]52 μ m map.

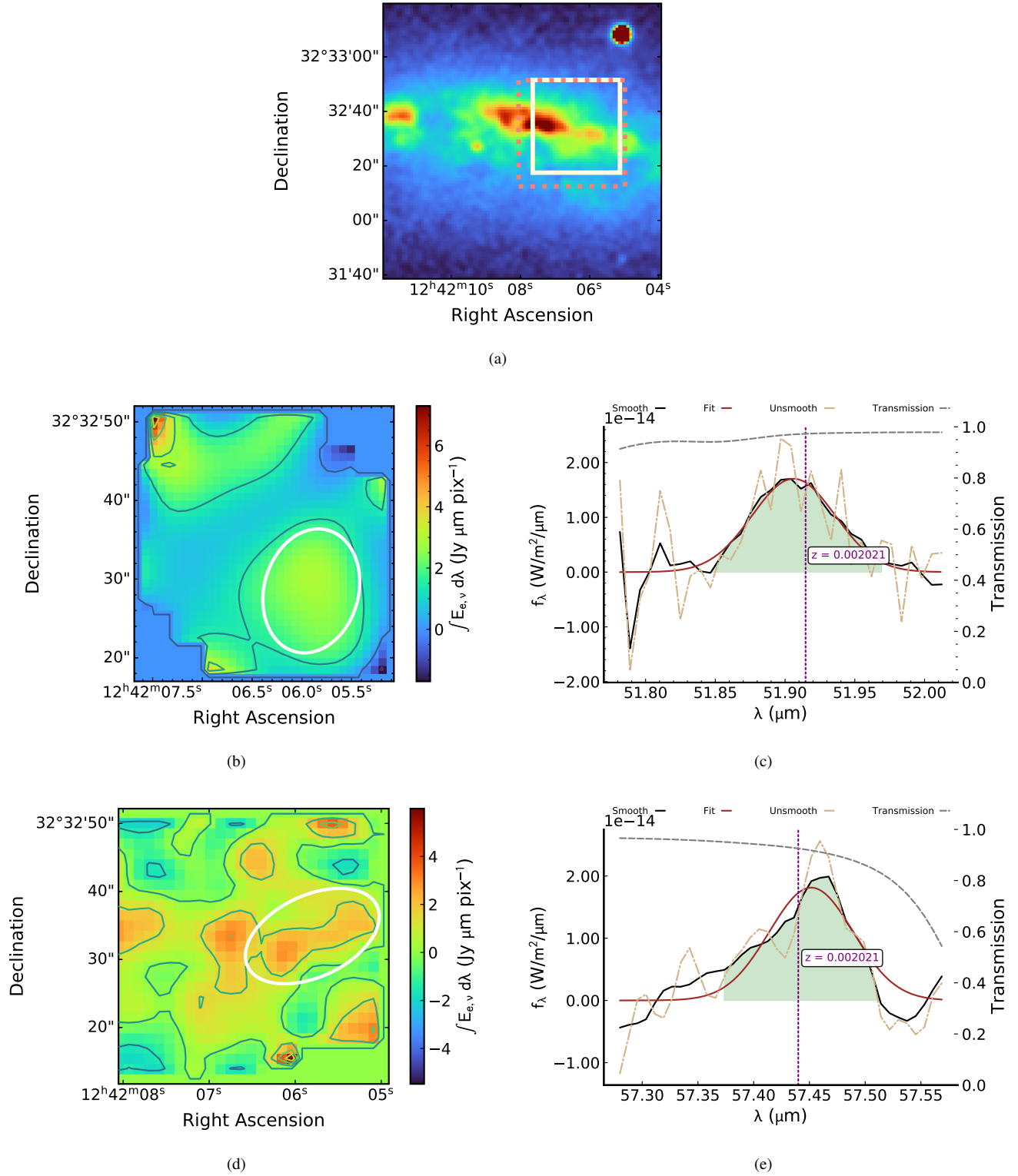


Figure 34. The 2MASS image (Figure 34(a)), 2-D linemaps and 1-D spectra for [OIII]52 μm (Figures 34(b) and 34(c), respectively) and [NIII]57 μm (Figures 34(d) and 34(e), respectively) in NGC4631. The datacube for [NIII]57 was processed independently by us to deal with the low transmission at the edge of the spectral range.

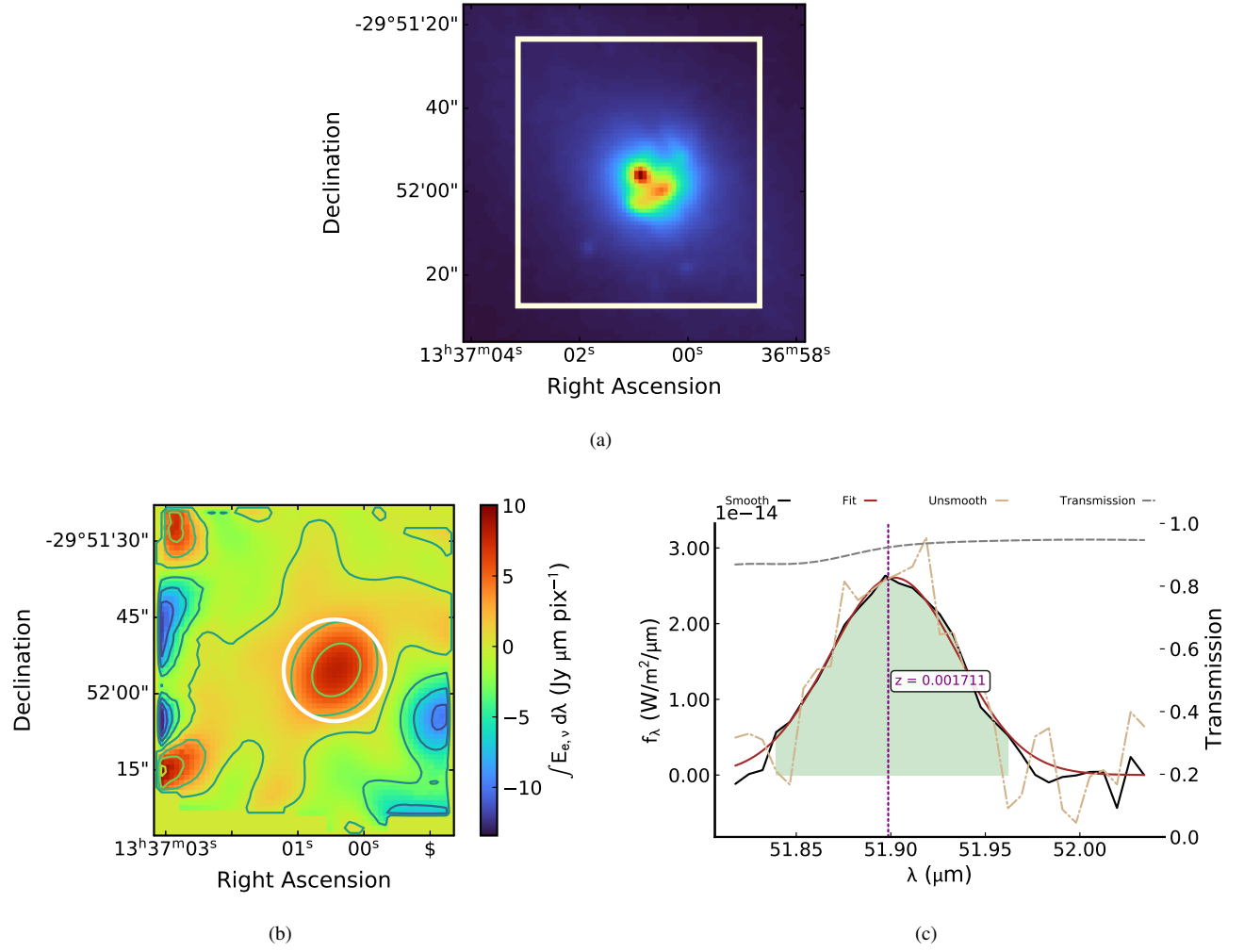


Figure 35. The 2MASS image (Figure 35(a)), 2-D linemap and 1-D spectrum for $[OIII]52\mu m$ (Figures 35(b) and 35(c), respectively) in M83.

We now show the linemaps and spectra for the galaxies mentioned in Table 4, for which only the [OIII] $52\mu\text{m}$ line was measured.

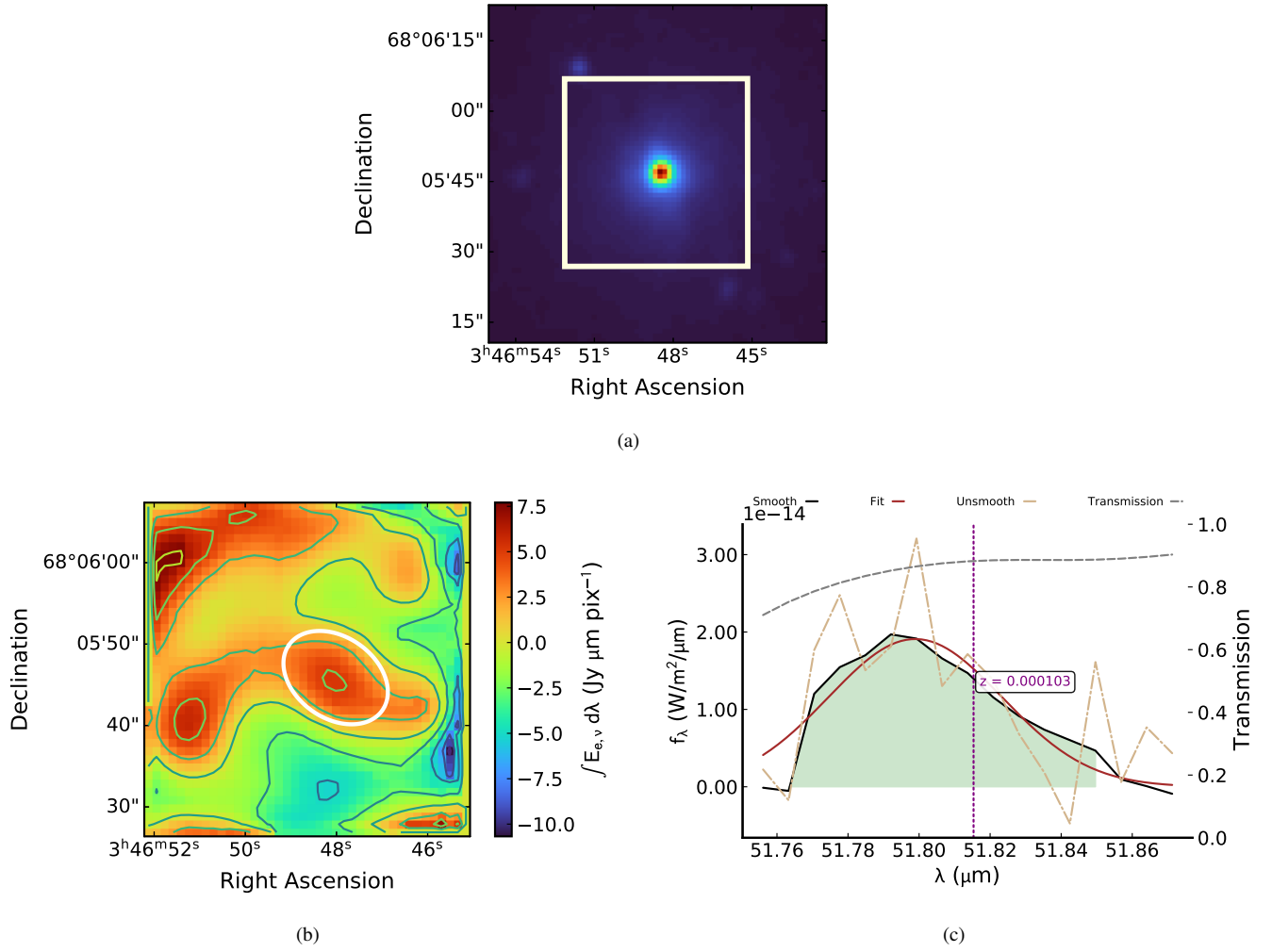


Figure 36. The 2MASS image (Figure 36(a)), 2-D linemap and 1-D spectrum for [OIII] $52\mu\text{m}$ (Figures 36(b) and 36(c)) in IC342.

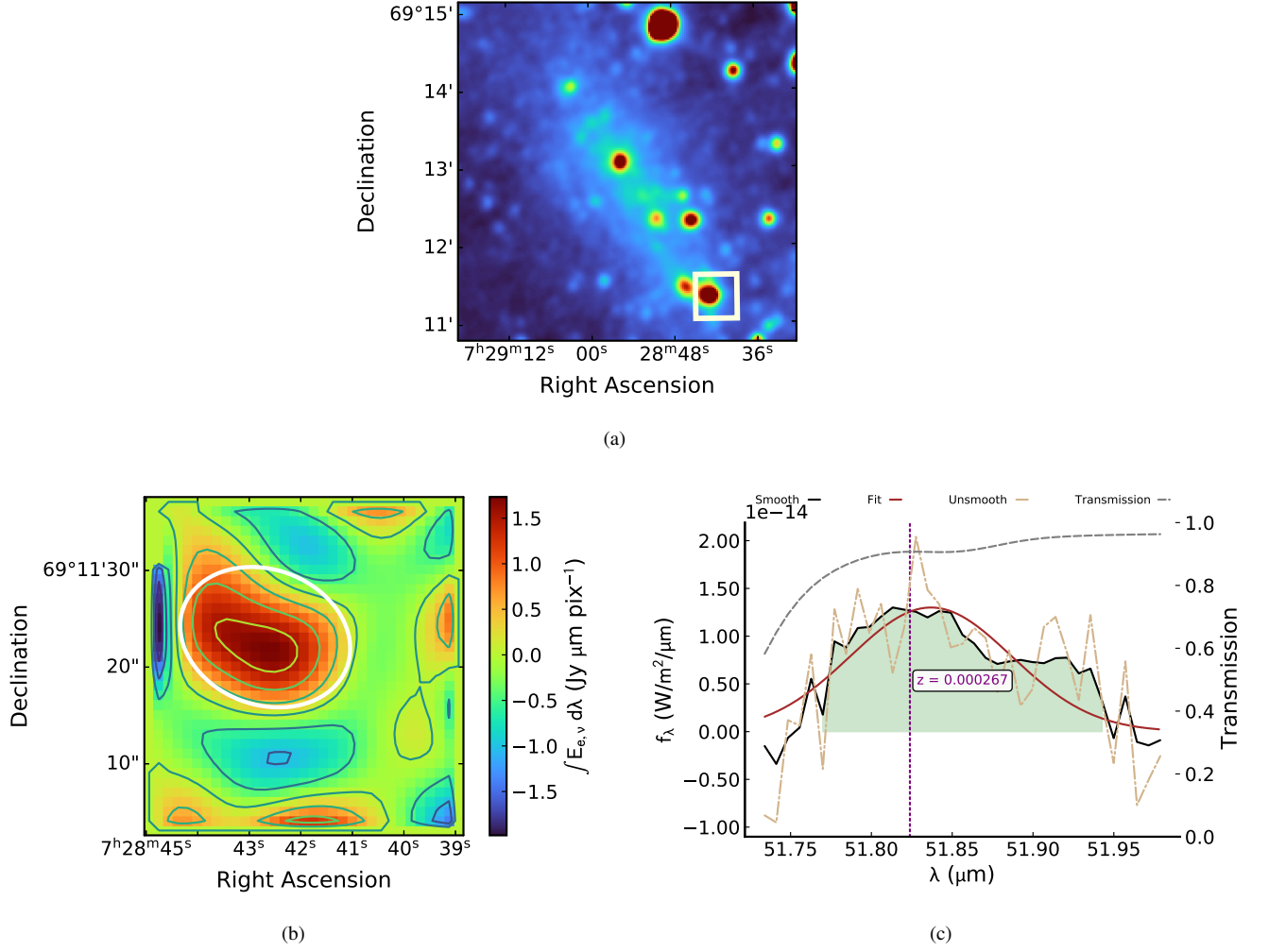


Figure 37. The WISE W1 band image (Figure 37(a); the 2MASS map in this case did not show appreciable detection), 2-D linemap and 1-D spectrum for [OIII]52μm (Figures 37(b) and 37(c)) in NGC2366. The profiles have not been corrected for atmospheric transmission. Once again, the SOFIA survey region shows significant departure from the optical center, just like NGC2366. This is because the SOFIA in this case was not pointed to the optical center, as displayed in the WISE map.

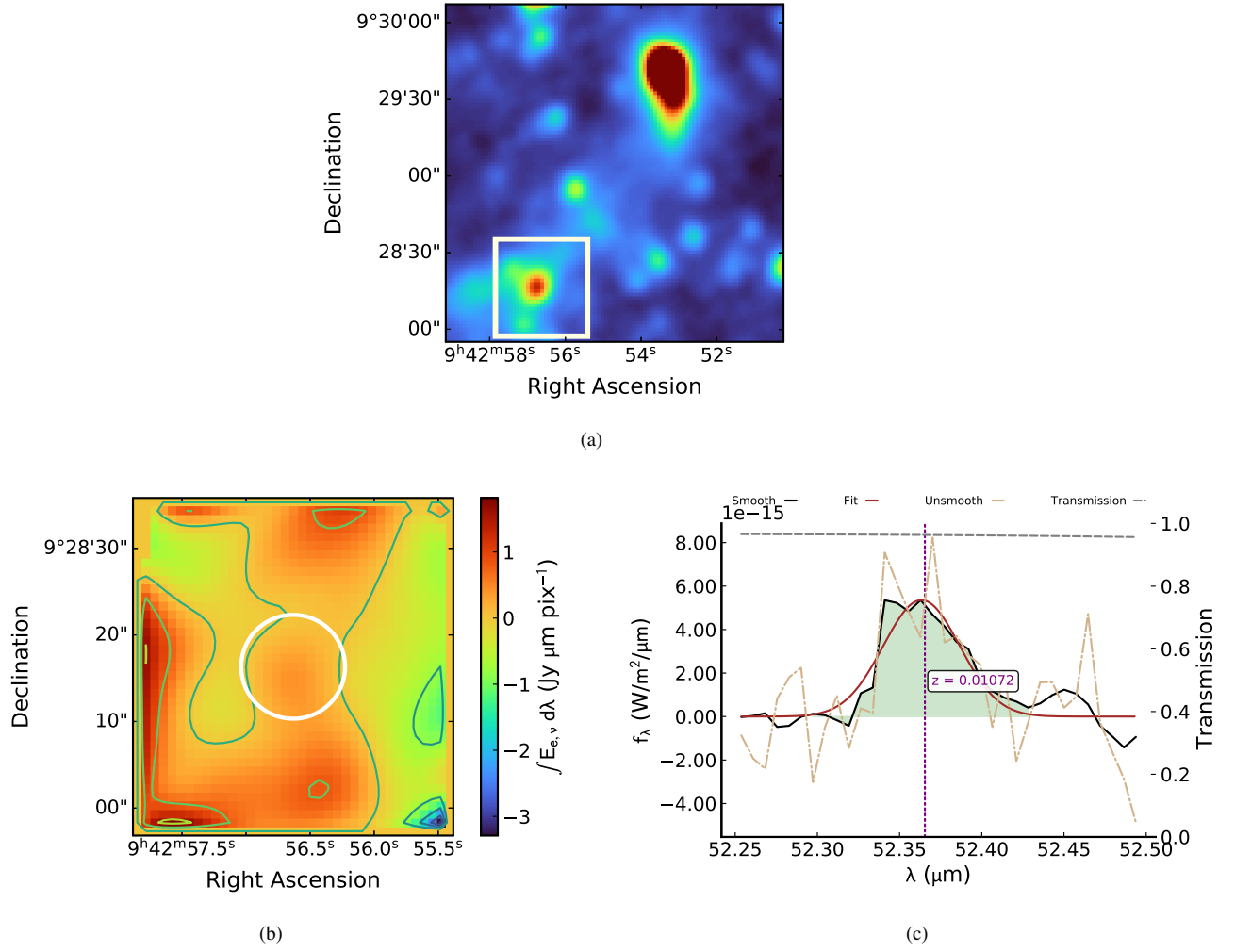


Figure 38. The WISE W1 band image (Figure 38(a); the 2MASS map did not show appreciable detection), 2-D linemap and 1-D spectrum for [OIII]52μm (Figures 38(a) and 38(b), respectively) in UGC5189. Once again, like NGC2366, one may notice the significant deviation of the SOFIA survey region from the optical center, just like NGC2366.

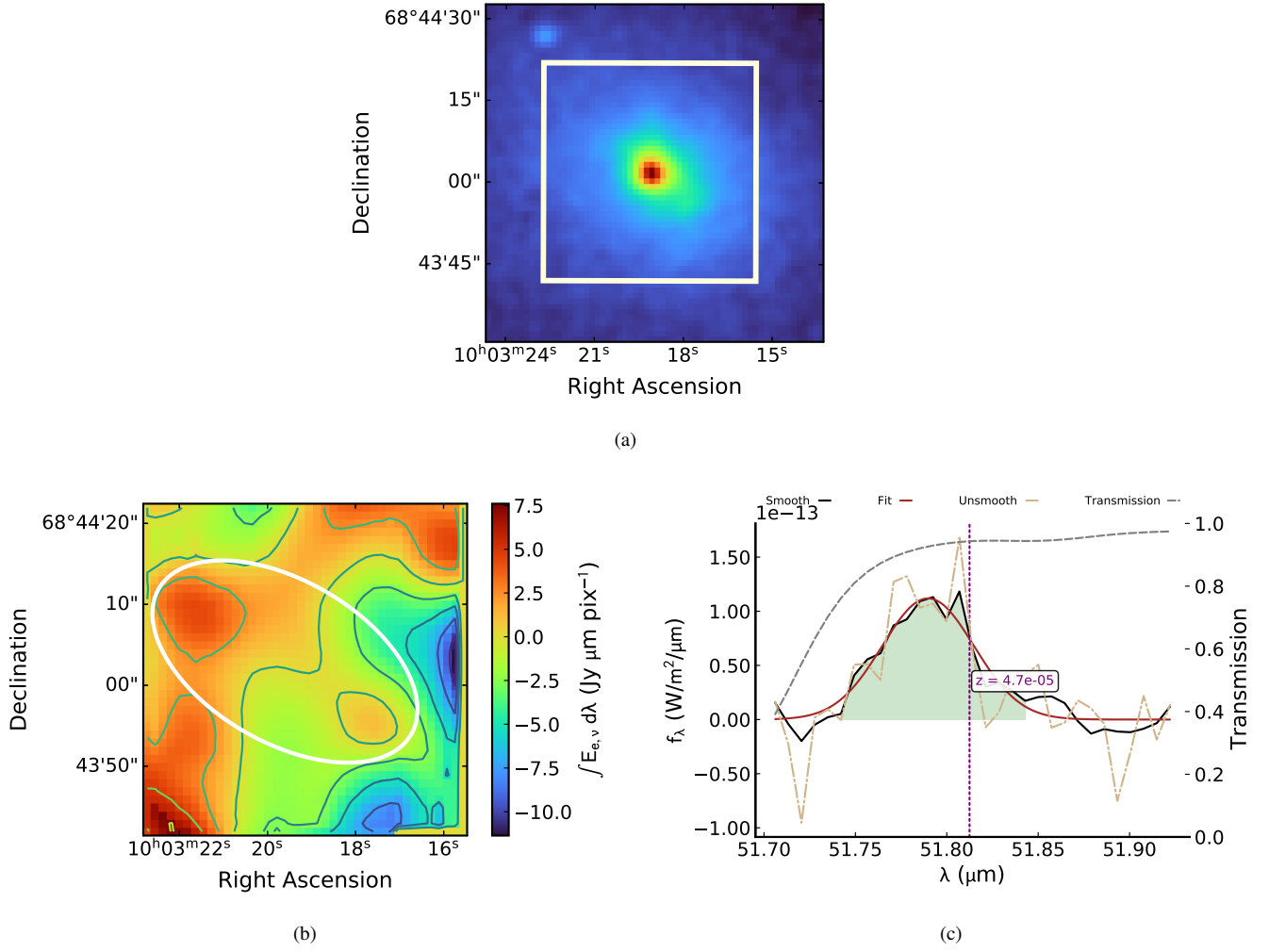


Figure 39. The 2MASS image (Figure 39(a)), 2-D linemap and 1-D spectrum for $[OIII]52\mu m$ (Figures 39(b) and 39(c)) in NGC3077. The profiles have not been corrected for atmospheric transmission.

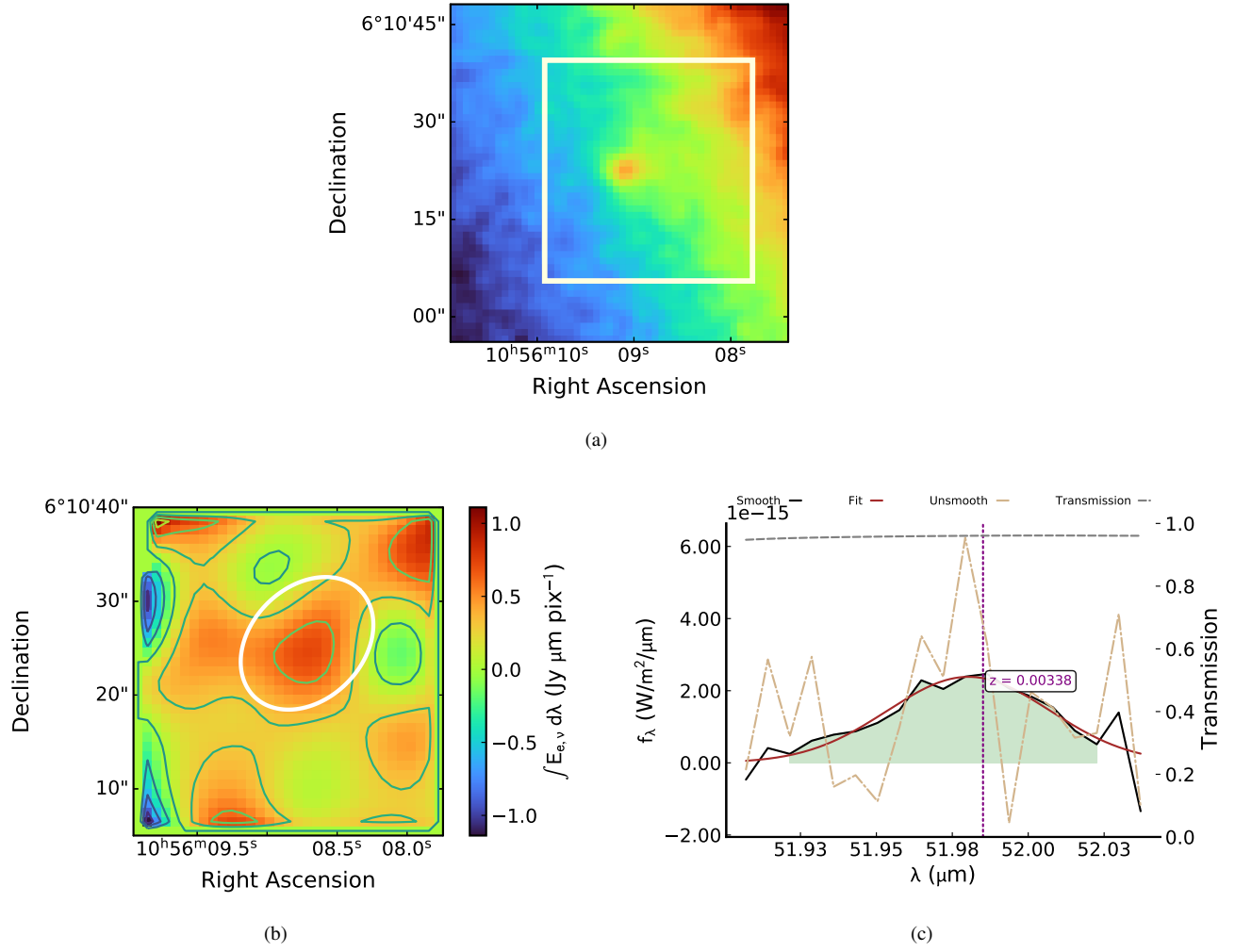


Figure 40. The 2MASS image (Figure 40(a)), 2-D linemap and 1-D spectrum for $[OIII]52\mu m$ (Figures 40(b) and 40(c)) in Mrk1271. The profiles have not been corrected for atmospheric transmission.

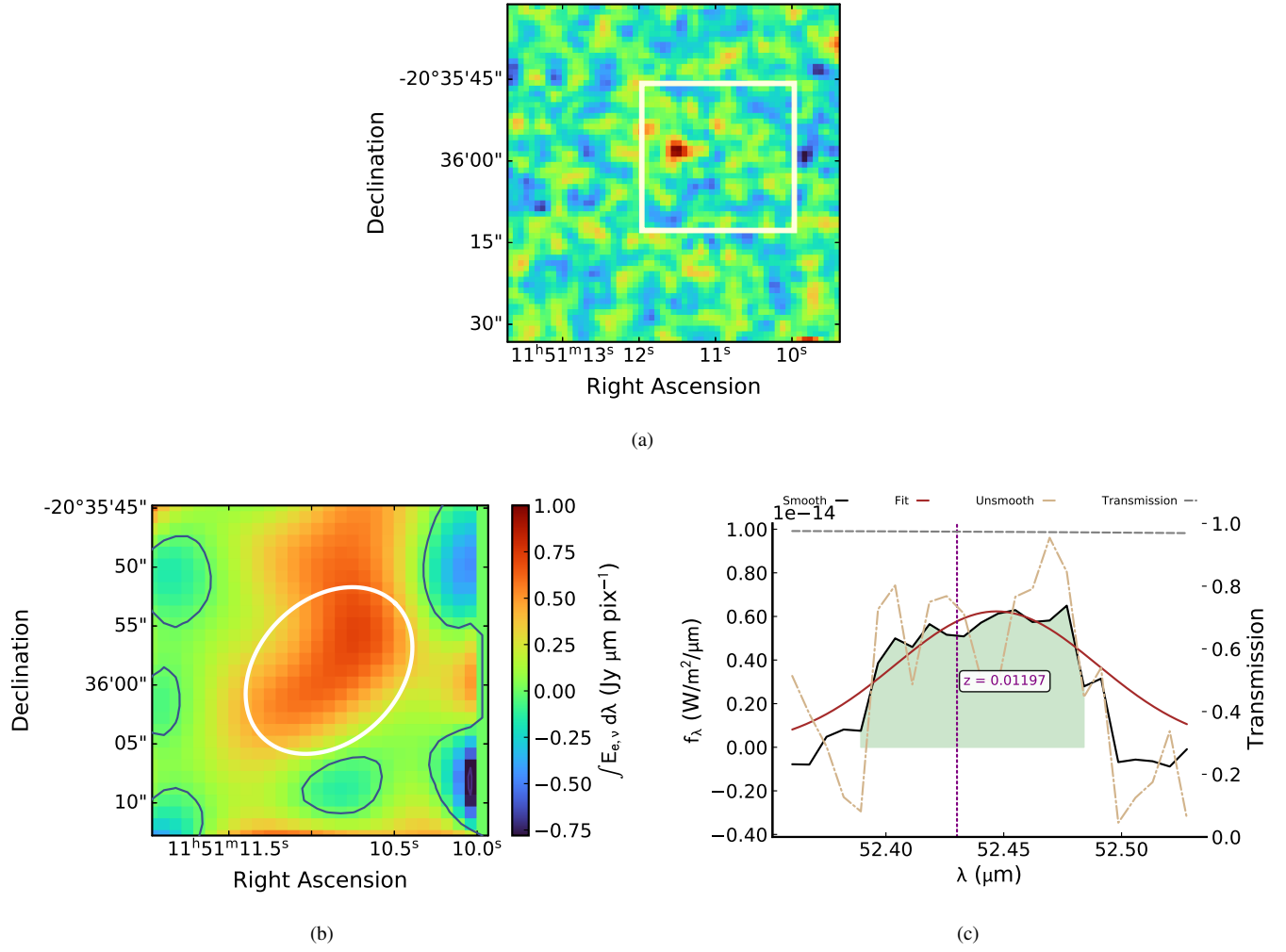


Figure 41. The 2MASS image (Figure 41(a)), 2-D line map and 1-D spectrum for $[OIII]52\mu m$ (Figures 41(b) and 41(c), respectively) in Pox4.

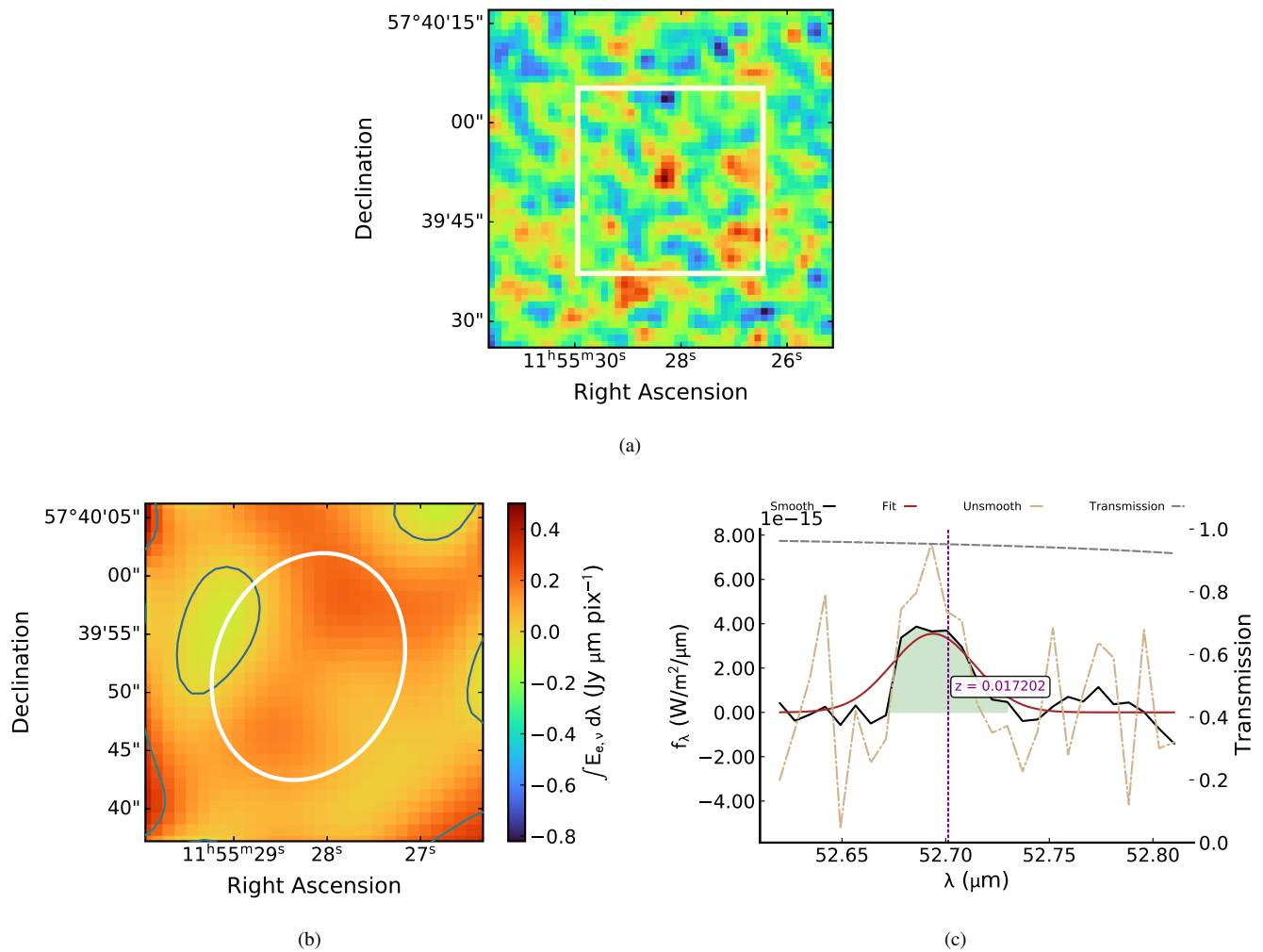


Figure 42. The 2MASS image (Figure 42(a)), 2-D linemap and 1-D spectrum for [OIII]52μm (Figures 42(b) and 42(c)) in Mrk193.

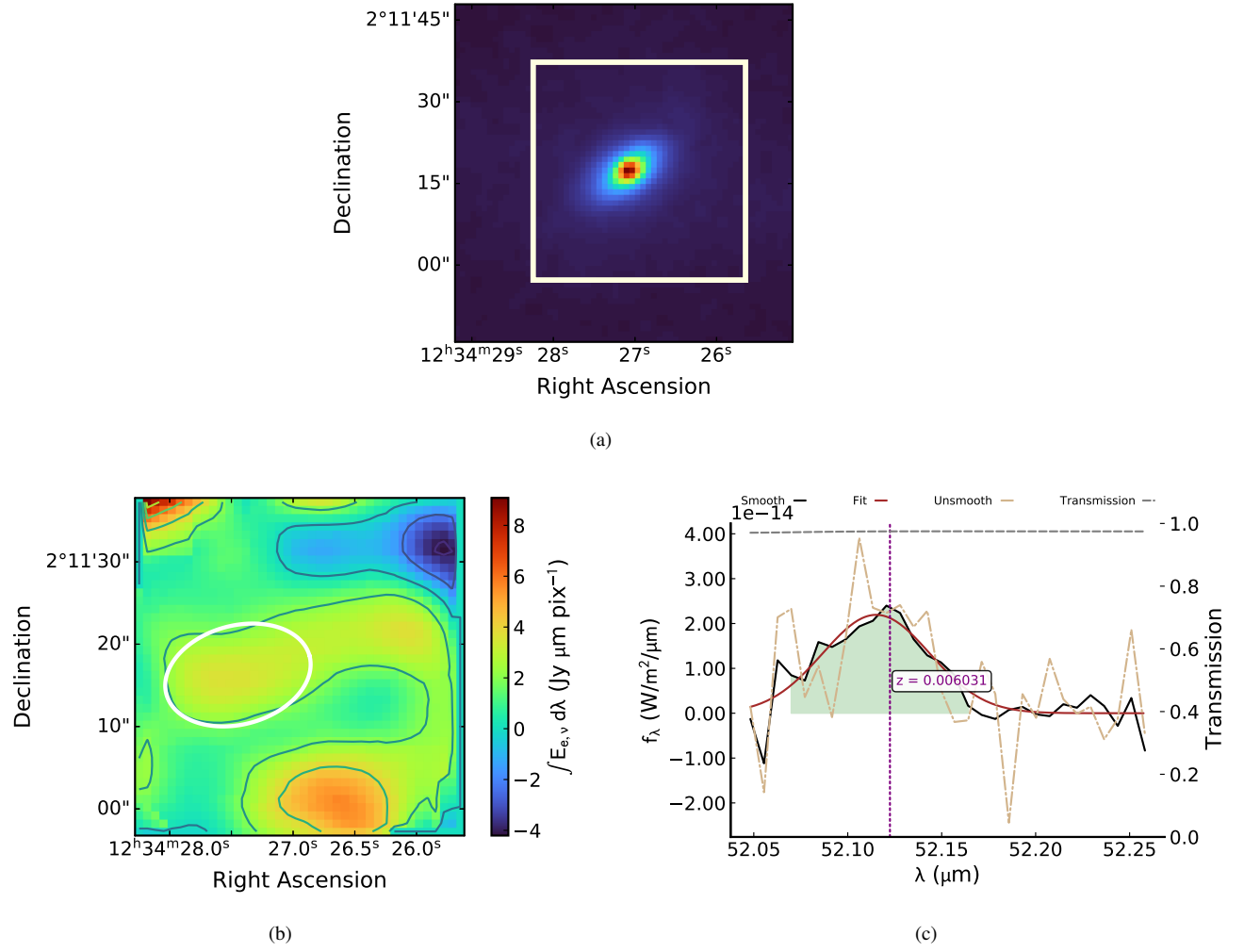


Figure 43. The 2MASS image (Figure 43(a)), 2-D linemap and 1-D spectrum for $[OIII]52\mu m$ (Figures 43(b) and 43(c)) in NGC4536.

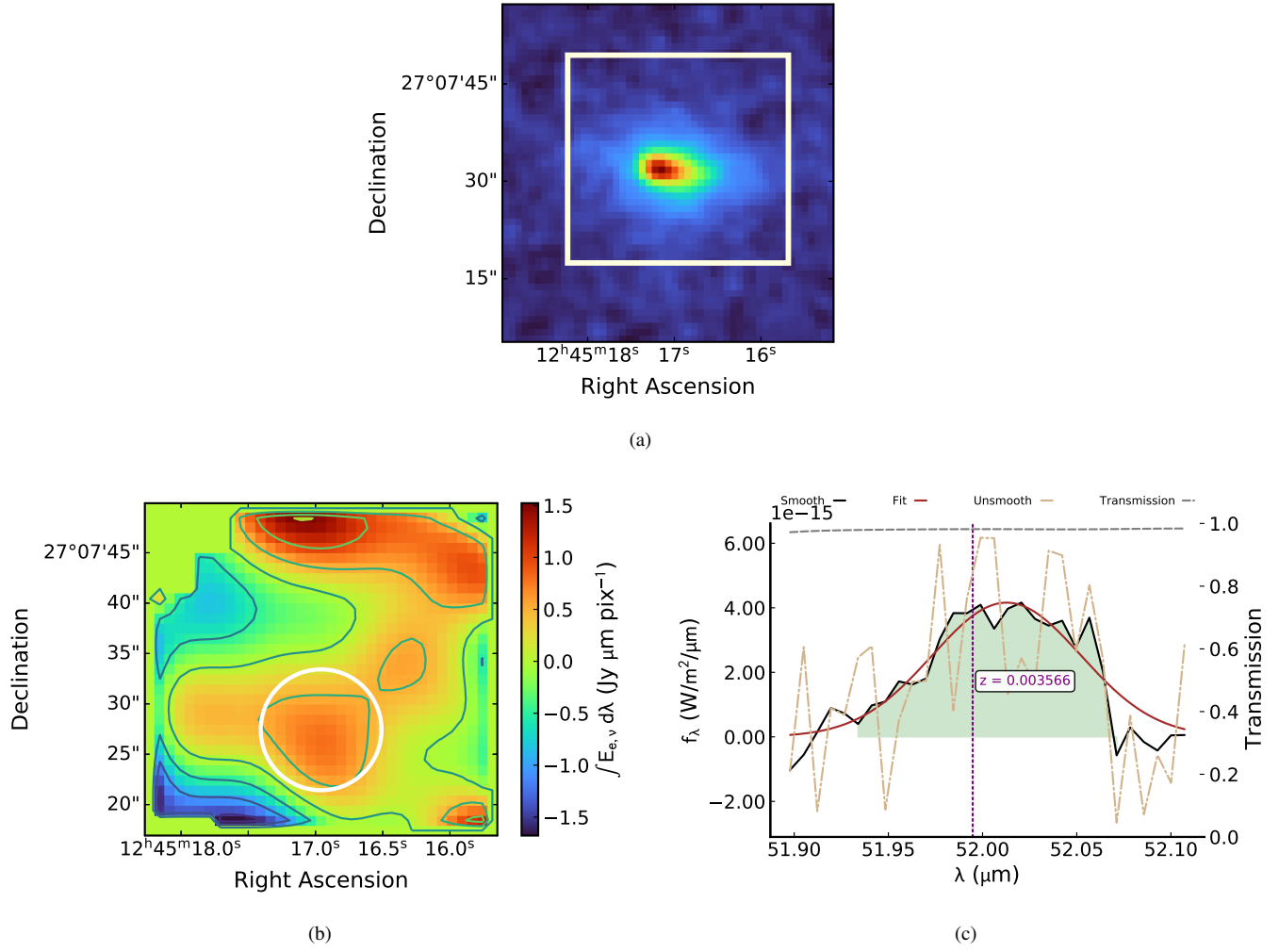


Figure 44. The 2MASS image (Figure 44(a)), 2-D linemap and 1-D spectrum for $[\text{OIII}]\lambda 52\mu\text{m}$ (Figures 44(b) and 44(c)) in NGC4670.

B. N/O ABUNDANCES FOR AGN FROM IR PHOTOIONIZATION MODELS

Fig. 45 shows the tight dependence of the N3O3 parameter, based on the ratio of [NIII]57 μ m and [OIII]52, 88 μ m lines, with the global N/O abundance ratio for the grid of AGN photoionization models using a power law continuum index of $\alpha_{\text{OX}} = -0.8$ ($F_\nu \propto \nu^{\alpha_{\text{OX}}}$). Due to the similar ionization structure of nitrogen and oxygen elements, variations in $\log U$ have a small effect in the N3O3 parameter, allowing us use a linear regression fit (black solid line; see Eq. 5) to determine the relative N/O abundances.

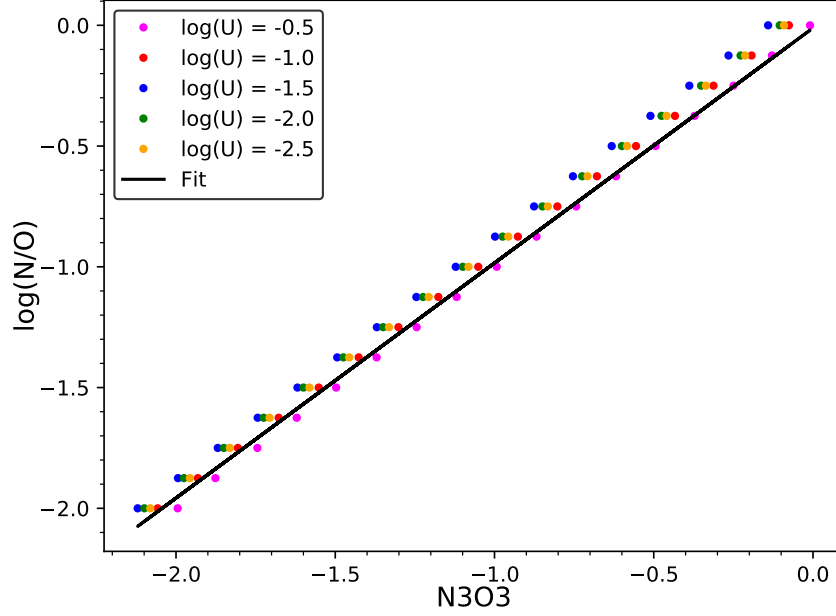


Figure 45. Predicted dependency of the inferred N/O abundances on the N3O3 parameter for AGN models with $n_e = 500 \text{ cm}^{-3}$ and $\log U$ in the -2.5 to -0.5 range. The solid black line shows a linear regression derived for the whole grid of models (see Section 4).

C. $\Delta(N/O)$ VERSUS DENSITY: IR LINES DIAGNOSTICS

In Fig. 18 we have explored the dependence of the $\Delta(N/O)$ with the electron density of the gas as measured from the optical [SII] $\lambda\lambda 6716, 6731$ doublet. We have also explored if the $\Delta(N/O)$ has some dependence on the electron density as derived from the IR fine structure lines of [SIII] and [OIII]. We presents the results here.

A similar trend to what is seen in Fig. 18 is also present in Fig. 46(a), where the $\Delta(N/O)$ value is plotted as a function of the electron density as derived from the IR fine structure lines of [SIII] $18.7\mu\text{m}$ and $33.5\mu\text{m}$. Also in this plot we see a higher $\Delta(N/O)$ value for higher gas densities, however no correlation is present either for HII region/ULIRG galaxies and dwarf galaxies or for the total sample that includes Seyfert galaxies.

Fig. 46(b) shows the $\Delta(N/O)$ value plotted as a function of the electron density as derived from the IR fine structure lines of [OIII] $52\mu\text{m}$ and $88\mu\text{m}$. In this figure, if one considers only the HII region/ULIRG and dwarf galaxies and excludes the Seyfert galaxies, a decreasing trend of the $\Delta(N/O)$ is found as a function of density. However, because of the large spread of the data and the poor statistics, no statistically significant correlation is found. We notice, however, that a decreasing trend of the $\Delta(N/O)$ value with the electron density, related to a higher value of $(N/O)_{OPT}$ at low densities, would indeed be expected by the presence of diffuse ionized gas (DIG). This is hot and low density gas in the disk of galaxies and can be excited by relatively old stars, which have enough time to increase the N abundance through secondary production, and thus would be also associated to higher $(N/O)_{OPT}$ values, while the IR lines would be less contaminated due to the higher excitation. This scenario would be in agreement with the conclusion by Peng et al. (2021).

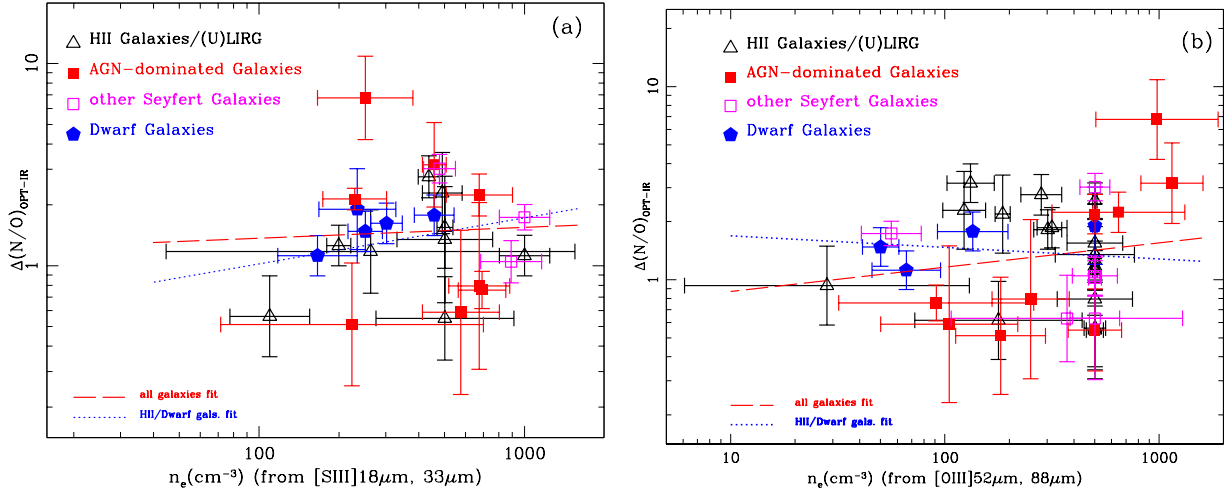


Figure 46. (a: left) Logarithmic difference between the N/O ratio computed from IR emission lines and the N/O from optical lines versus the electron density of the gas, as measured from the IR [SIII] $18.7\mu\text{m}$ and $33.5\mu\text{m}$ lines. The dotted line gives the fit for HII/ULIRG and dwarf galaxies: $y = (0.23 \pm 0.22) \cdot x - (0.45 \pm 0.56)$ ($\chi^2 = 0.47$, $R = 0.29$). A fit to all the data gives (shown as a dashed line): $y = (0.05 \pm 0.23) \cdot x + (0.03 \pm 0.60)$ ($\chi^2 = 1.97$, $R = 0.05$). (b: right) Logarithmic difference between the N/O ratio computed from IR emission lines and the N/O from optical lines versus the electron density of the gas, as measured from the IR [OIII] $52\mu\text{m}$ and $88\mu\text{m}$ lines. The dotted line gives the fit for HII/ULIRG and dwarf galaxies: $y = -(0.06 \pm 0.13) \cdot x + (0.29 \pm 0.32)$ ($\chi^2 = 0.98$, $R = -0.10$). A fit to all the data gives (shown as a dashed line): $y = (0.12 \pm 0.12) \cdot x - (0.19 \pm 0.30)$ ($\chi^2 = 2.58$, $R = 0.17$).